Mesoscale Modeling and Computer Simulation of Tethered Nanoparticle “Shape-Amphiphile” Assemblies

by

Christopher R. Iacovella

A dissertation submitted in partial fulfillment
of the requirements for the degree of
Doctor of Philosophy
(Chemical Engineering)
in The University of Michigan
2009

Doctoral Committee:
- Professor Sharon C. Glotzer, Chair
- Professor John Kieffer
- Professor Nicholas A. Kotov
- Professor Ronald G. Larson
- Associate Professor Michael J. Solomon

To my family and friends.

Acknowledgments

I would like to thank my advisor, committee and all those professors, friends, and family members that have encouraged me throughout the course of school. To Professor Sharon Glotzer, my advisor, I thank you for all the encouragement and guidance during my time at Michigan. Your confidence and belief in me has helped me to grow as a researcher and I am very grateful for all the many opportunities and resources you provided.

I would like to extend a special thanks to Professor David A. Kofke for giving me the opportunity to start my research career, teaching me about simulation, and encouraging me to attend graduate school. I thank Assistant Professor Suljo Linic for his help, advice and support during my time as a GSI. I would also like extend appreciation to my committee members, Associate Professor Michael J. Solomon, Professor John Kieffer, Professor Ronald G. Larson, and Professor Nick Kotov, for their support, ideas, and time during my graduate career. I am very grateful to have a committee with such dedicated faculty members that were always willing to provide assistance.

I am very grateful to Dr. Mark A. Horsch and Dr. Zhenli Zhang who were instrumental during the early stages of my time in the Glotzer group. Their knowledge, guidance, and outlook will forever be appreciated.

I would like to thank Aaron Keys for the many thought provoking and helpful discussions related to research and code development. I would also like to thank Stephanie Teich-McGoldrick and Eric Jankowski for their research discussions, support and friendship during graduate school. I was very lucky to have had such good friends like Aaron, Stephanie, and Eric in the lab.

I thank Dr. Benjamin Gould for the many interesting research discussions, advice, encouragement, experiments in cooking, and friendship.

I would also like to extend thanks to the rest of the many Glotzer group members I've worked with over the years, especially Magnus Bergroth, Tom Babinec , Carolyn Phillips, Trung Dac Nguyen, and Aaron Santos.

I thank the the U.S. Department of Energy, U.S. Department of Education GAANN Fellowship, and the University of Michigan Rackham Predoctoral Fellowship for funding my research. I have extreme gratitude for staff at the Center for Advanced Computing, especially Andy Caird, Brock Palen, and Matt Britt.

To my parents Pamela and Charles Iacovella, and siblings Kerri and Shawn, I can never say thank you enough for your support, encouragement, and understanding during this long and somewhat arduous experience. To my nieces Kiera and Brianna, thank you for always being to bring a smile to my face no matter how stressed. To my Ann Arbor family, Brett, Rebecca, Parker, Christine, Chris and Dr. Sallie Churchill, sincere thanks for welcoming me into your family and helping make Ann Arbor feel like home. To my fiancée Dr. Nicole Behnke, your love, support, patience, and encouragement in these last few years has meant the world to me.

Table of Contents

List of Tables

Table

List of Figures

Figure

List of Appendices

Appendix

Abstract

In this dissertation, we explore the use of polymer-tethered nanoparticles as a means to self-assemble highly ordered arrays of nanoparticles and nanometer-sized domains. We perform Brownian dynamics simulations to study the self-assembly of polymer functionalized spherical and rod-like nanoparticles. Immiscibility between tethers and nanoparticles facilitates assembly into highly ordered structures reminiscent of phases formed by surfactants and block copolymers, but with greater complexity. We explore the influence of key factors such as the nanoparticle size and shape, tether architecture, solvent selectivity, and bulk volume fraction on the resulting structures.

In this thesis we perform several studies. First, we explore the phase behavior of mono-tethered nanospheres. Under solvent conditions that are poor for the tethers, we find phase behavior that is similar to surfactants with structures including lamellae, perforated lamellae, hexagonally packed cylinders, and spherical micelles. We report quasicrystalline-like ordering between the spherical micelles and propose an entropic model to explain this behavior. We also explore the phase behavior of a mono-tethered nanosphere system where nanospheres are in poor solvent. We find phases similar to surfactants including lamellae, perforated lamellae, double gyroid, and hexagonally packed cylinders. We see a predominance of icosahedral arrangements of nanospheres in phases with 2D confinement and crystalline packing of nanospheres in structures with 1D confinement. We also compare and contrast the formation of the double gyroid structure for tethered nanospheres and tethered nanorods. We show that the ability of the nanoparticles to locally order into icosahedra (nanospheres) and hexagonally splayed bundles (nanorods) reduces packing frustration making these structures more stable than their block copolymer counterparts.

We also explore the phase behavior of di-tethered nanospheres. We find a complex phase behavior for di-tethered nanospheres similar to triblock copolymers with phases including lamellae, tetragonally packed cylinders, alternating gyroid, and alternating diamond. We also report two novel phases not seen in triblock copolymers: NaCl ordered spherical micelles with a complementary simple cubic network of nanospheres and ZnS ordered micelles with a complementary diamond network of nanospheres.

Throughout this thesis we focus on understanding why these complex structures form and what trends exist.

Chapter 1

Introduction

1.1 Motivation

Assembly of materials from the "bottom up" provides an unprecedented number of opportunities for creating novel materials with specific physical properties. Applications are vast, impacting everything from electronics to drug delivery. To date, a large variety of nanometer scale building blocks with specific geometries, such as spheres (1), rods (2), cubes (3), plates (4; 5), and tetrapods (6), have been synthesized from various materials. The development of recent techniques, such as imprint lithography (7), have given experimentalists even more control over shape, making for an almost limitless catalog of nanoparticle geometries. Nanoparticles are of particular interest as bottom up materials, since they often have tunable electrical, optical and mechanical properties that are different from their bulk counterparts. By properly choosing the building block or combinations of building blocks, we can create materials with specific, desirable properties.

The assembly of these nanoparticle building blocks into specific structures and devices is a fundamental challenge if large numbers of building blocks are required. Proof of concept devices such as single electron transistors have been created using direct mechanical manipulation (8). Such an approach might be unfeasible for large scale production of common devices made of many transistors, e.g. current computer chips contains $\sim$1 billion transistors (9). Manipulation of large numbers of these building blocks into specific arrangements seems an insurmountable task for mechanical methods. Instead, self-assembly is generally regarded as a promising means to facilitate the assembly of large numbers of nano building blocks into desired structures (10; 11). For self-assembly to be a predictable method for the design of novel materials, one must understand the roles thermodynamic parameters, geometry, and functionalization play in the assembly process, and how this information can be classified and used to guide the design of new materials and devices.

The literature contains many methods and demonstrations of approaches to the self-assembly process, yet only a few demonstrate a comprehensive, predictable scheme. Current methods for the self-assembly of nanoparticles include polymer templates whereby nanoparticles are fillers in an organic medium (12), the application of external fields where shear or magnetic fields are applied to suspended nanoparticles(13; 14), or the use of surface stamping techniques to direct the assembly(15; 16). A method proposed by Zhang, et al. (17) is to utilize soft matter to assemble nanoparticles by functionalizing the nanoparticles with a small number of polymeric tethers, creating "tethered nanoparticles." This scheme relies on the thermodynamic immiscibility between nanoparticle and tether to facilitate the assembly of the nanoparticles; the resulting structure is heavily influenced by the geometry of the nanoparticle, location of the tether attachment, and various properties of the tether, e.g. molecular weight. Due to the immiscibility and geometric constraints, tethered nanoparticles constitute a new class of macromolecules referred to as "shape amphiphiles" (18). Roughly speaking, tethered nano building blocks share many features with block copolymers and surfactants–each are composed of two or more immiscible blocks bonded together. It may therefore be expected that the microphases created by these tethered nanoparticle systems are governed by similar physics where systems seek to minimize their free energy by aggregating with like species (17) (see section 2.1). Unlike traditional amphiphiles, the "head" group of a shape amphiphile has a large excluded volume and distinct geometry, which may heavily influence and even provide control over the self-assembly process.

1.2 Overview

In this thesis the role of immiscibility, nanoparticle geometry, and tether placement for tethered nanoparticles is investigated with an emphasis on making comparisons with other amphiphiles such as surfactants, diblock copolymers, and linear and star triblock copolymers. The objectives of this work are to elucidate the key parameters that control the self-assembly of polymer tethered shape amphiphiles and explore the vast parameter space of possible structures.

Chapter 1 provides motivation for carrying out the research within this thesis. Chapter 2 provides background on amphiphiles, nanoparticles, and the use of polymers to guide the self-assembly of nanoparticles.

Chapter 3 describes the simulation models, Brownian dynamics simulation method and general simulation procedure utilized.

Chapter 4 discusses the key analysis routines developed and applied throughout the course of this dissertation. These methods include (1) the $\mathrm{R}_{y}lm$ method for determining local structure, (2) a method for calculating the center-of-mass based on image processing techniques, and (3) the bond order diagram method used to characterize crystalline structures.

Chapter 5 discusses the self-asembly of mono-tethered nanospheres. The temperature verses volume fraction phase behavior is investigated as a function of nanosphere diameter and solvent selectivity. We find a variety of bulk ordered structures including lamella, perforated lamella, the double gyroid, hexagonally packed cylinders, and ordered spherical micelles. We also compare our results with surfactants and present a rough mapping between model tethered nanospheres and surfactants. Additionally, we explore the local structure of the nanospheres finding a distinct icosahedral ordering under certain conditions. We investigate how local structure is related to the microphase ordering of the system.

Chapter 6 explores the double gyroid structure formed by both mono-tethered nanospheres and mono-tethered nanorods. We develop a relationship for the Flory-Huggins χ parameter to allow for the direct comparison between mono-tethered nanospheres, mono-tethered nanorods, and surfactants/diblock copolymers. We discuss the stability of the double gyroid structure as it relates to void fraction and packing frustration. We additionally calculate the local structure of the nanospheres and nanorods, in both cases finding a trend towards the formation of dense, minimal energy configurations.

Chapter 7 examines the ordering present in a system of spherical micelles formed by mono-tethered nanospheres in selective solvent. We present results that demonstrate ordering reminiscent of a dodecagonal quasicrystal and compare with a known quasicrystal forming system. We also present a simplified model of the system to explain this ordering.

Chapter 8 explores the phase behavior of di-tethered nanospheres. We present the phase behavior under melt-like conditions as a function of temperature, nanosphere diameter, and the planar angle separating the two tethers. We find a variety of phases reminiscent of triblock copolymers, including lamella, the alternating gyroid, alternating diamond, and alternating tetragonally ordered cylinders. We also find two novel phases, namely NaCl ordered spherical micelles with a complementary simple cubic network of nanospheres and zincblende (binary diamond) ordered spherical micelles with a complementary diamond network of nanospheres. We also explore the temperature verses block fraction phase behavior under melt like conditions to understand how asymmetry impacts the phase behavior.

Chapter 9 summarizes the important results and contributions of this work. Additionally, a short discussion of the future direction of this research is presented.

Chapter 2

Background

2.1 Amphiphiles

It is well known that certain molecules are water soluble and effectively repel each other in water, preferring to maximize their contact with water rather than each other. In contrast, hydrophobic molecules exhibit an effective attraction when in water and tend to minimize their contact with water by aggregating. If we consider a simple case where equal amounts of A and B particles are mixed in water (A being hydrophobic and B hydrophilic), the result will be a macrophase separated system. In the macrophase separated system, most of the A particles will reside on one side of the box and most B particles will reside on the other. If the A and B particles were instead linked together they can no longer macrophase separate, but instead must microphase separate. The resulting microphase separated structure will be a compromise between the desire of A to minimize contact with water and B to maximize contact with water. Bonding two immiscible blocks together results in what is termed an amphiphile. The degree of miscibility or immiscibility of the two ends of an amphiphile causes the building block to form a variety of structures, referred to by Tanford (19) as micelles. The general class of micelles includes many structures such as spherical micelles, bilayers, vesicles (20), oblate and prolate ellipsoids, and long cylinders (19).

Surfactants and block copolymers are common examples of amphiphilic molecules. Surfactants are generally made of a lyophilic (hydrophobic) species and a hydrophilic species that are chemically bonded together. Typically the lyophilic group (referred to as the tail) is a slender hydrocarbon chain with length of 8-20 units, and the hydrophobic group (referred to as the head) is usually a short and bulky chain (21). Block copolymers – materials with two more distinct monomer species – can be thought of as a more general classification of a surfactant. A typical phase diagram for surfactants or diblock copolymers (i.e. molecules made of two immiscible blocks) has several distinct regions; depending on concentration and/or relative size of the blocks one observes spherical micelles, wormy micelles, hexagonally packed cylinders, the double gyroid, and lamellar sheets (21; 22; 23; 24; 25).

However, there can be much richness added to the typical phase diagram, such as BCC ordered micelles (21; 23; 25) or other bicontinuous structures (e.g. double diamond and plumber's nightmare)(26), depending on the relative size and interactions between the blocks or interaction with excess monomer in the system.

Triblock copolymers are another specific instance of a block copolymer where three distinct, immiscible blocks are joined together. Triblock copolymers can be joined together in a linear fashion, referred to as a linear triblock copolymer, or joined to a central location, referred to as a star triblock copolymer. Linear triblock copolymers have a richer phase behavior than diblock copolymers and are known to self-assemble into phases such as lamella (27), alternating diamond (28; 29; 30), alternating gyroid (27), alternating tetragonal cylinders (27; 30), and alternating spherical micelles that arrange in a CsCl structure (27; 30). Star triblock copolymers organize into a variety of complex phases including lamella perforated with spherical micelles (31) and alternating cylinders in a [6,6,6] Archimedean tiling (31). Mixtures of ABC star triblock copolymers and homopolymers have been shown to form cylinders that display quasicrystalline ordering (32) and ZnS (binary diamond) ordered spherical micelles (33).

Surfactants and diblock copolymers are in many ways similar to some of the simpler cases of tethered nanoparticles, such as mono-tethered nanospheres and mono-tethered nanorods. Both surfactants and the tethered nanoparticle systems have a distinct head and tail group that are immiscible. Similarly, triblock copolymers share many features with di-tethered nanoparticles (i.e. they are composed of three immiscible blocks).

2.2 Nanoparticles

In the last fifteen years, the catalog of nanoparticles of various shape, size, and composition (34; 2; 35; 36; 37; 6; 1; 38; 5; 39; 40; 3; 41) has grown dramatically. These include, but are not limited to, metallic and semiconductor nanospheres (1), nanorods (2), nanocubes (3), multipods (6; 42), and nanoplates (4; 5). Molecular nanoparticles of interest include carbon fullerenes (38; 43), porphyrin squares (44), and polyhedral oligomeric silsesquioxane (POSS) cages (45; 46).

Generally, the synthesis of metallic nanoparticles in solution is accomplished by means of a reduction reaction. A salt solution containing a given metal is mixed with a reducing agent and a stabilizer (capping agent). A typical reaction for the synthesis of gold nanoparticles is as follows (47):

$$\mathrm{H_2AuCl_4 + C_3OH(COOH)_3} \xrightarrow{H_2O,100^\circ C} \text{Citrate capped gold nanoparticle}$$

It has been shown by Sun and Xia that a decrease in salt concentration may result in a change in the shape of the aggregate. They observed that by decreasing the salt concentration for a gold system wires formed rather than cubes (40). Carotenuto and Nicolais showed that decreasing the concentration of the reducing agent resulted in a decrease in particle size (48). Solvent interactions, specifically solvent-philicity and phobicity, are inherited from the terminating groups on the stabilizing polymer/capping agent, and can therefore be modified. The composition of the nanoparticle (species and crystallinity), may influence the range/shape of particle-particle interaction (49) or result in a dipole moment (50). There are other variables that affect the formation of nanoparticles, but by changing only a few parameters, much about a nanoparticles geometry and interaction can be modified and even tuned. Based on how nanoparticles are synthesized and stabilized, they lend themselves readily to functionalization by polymeric materials.

2.3 Polymer-mediated self-assembly of nanoparticles

Polymers have been shown to act as a means to guide the self-assembly of nanoparticles into ordered aggregates (51; 15; 52; 53; 54). Typically in these systems, nanoparticles are coated with a large number of polymers with desirable interactions. For example, one of the first proof-of-concept studies showed that coatings of synthetic polymers could be used to control interparticle spacing between gold nanospheres and also facilitate the aggregation of gold nanospheres into larger spherical aggregates (51). Other early work showed that biopolymers, specifically DNA, can be used to create networks of nanoparticles with lock-and-key interaction specificity in a reversible manner (15); the reversibility and lock-and-key functionality is currently being utilized in biosensing applications (15). More recent work has explored using the specific interactions of DNA to allow for dynamic crystallization, e.g. controlling lattice parameters and degree crystallinity by changing the type of linker molecules added to the system (55).

2.4 Polymer-tethered self-assembly of nanoparticles

Functionalization of nanoparticles with a small number of oligomeric or polymeric tethers is a novel strategy to induce the self-assembly of nano particles in a predictable and controllable manner. This method is similar to polymer-mediated self assembly, discussed in section 2.3, however it typically involves only attaching a countable number of polymers to a nanoparticle (e.g. one to ten), creating a building block with many levels of anisotropy.

Recent advances in synthesis techniques are providing ever-increasing control over the ability to attach a small number of tethers to specific locations on the surfaces of nanoparticles creating shape amphiphiles with both controllable nanoparticle geometry and tether placement. Prototypical examples of experimentally synthesized tethered nanoparticles includes mono-tethered spheres(56; 57; 58; 59; 60; 61; 62), ditethered spheres (34; 63), tethered rods (64), and tethered cubes (45; 46; 65).

2.4.1 Experimental studies of tethered nanoparticles

There have been many studies in the literature looking at the assembly of tethered nanoparticles. For example Song and coworkers created single and double Buckyball-capped poly(ethylene oxide) (PEO) tethers, finding that the single-capped PEO tethers formed larger aggregates than the double-capped tethers. Buckyball-capped tethers also formed larger aggregates than paraffin-capped tethers which was postulated to be a result of the Buckyballs being more hydrophobic than the paraffins (56). This study demonstrates that tether and solvent conditions can be used to moderate and potentially control the self-assembly and aggregation of nanoparticles. However, it also shows the lack of a priori predictability; Song et al. lacked a definitive theory or framework to understand tethered assembly or to elucidate the impact of geometry, tethering, or other thermodynamic parameters.

Similar work by Kim, et al. looked at mono-tethered nanospheres, where the sphere portion was composed of one end of a collapsed diblock copolymer. Changing from a linear chain to a tethered sphere was shown to change the morphology from spherical micelles to wormy cylindrical micelles (61). Again, this study shows the control that geometry can have on structure, but also the lack of predictability when geometric changes are made to shape amphiphiles.

Westenhoff and Kotov created a network of quantum dots on “ropes,” where cadium telluride (CdTe) nanoparticles were tethered to a polyelectrolyte film by anionic polyethylene glycol (PEG) tethers. The relative distance between the quantum dot and the film was controlled by changing the solvent quality, which was used to change the luminescence (58).

There are many other proof of concept studies related to the synthesis and assembly of tethered nanoparticles. Di-tethered gold nanospheres have been shown to form ring-like structures (34). Recent work by DeVries, et al. showed that two polymeric tethers attached to the poles of gold nanospheres can be used to promote the formation of chain like aggregates (63). End-tethered nanorods have also been shown to form chain aggregates (64). These examples of tethered nanoparticles serve as a proof of concept and represent substantial progress toward realizing shape amphiphiles with specific geometry and structure.

2.4.2 Simulation studies of tethered nanoparticles

Zhang, *et al.* (17) were first to perform a simulation study of tethered nanoparticles broadly exploring the role of nanoparticle shape, number of tethers, tether location, and solvent selectivity. Specifically, they studied several statepoints of disks with tethers attached either equatorially or on the faces, mono- and di-tethered spheres, triangular plates with tethers attached at the vertices, and end-tethered rods (17). In the study of tethered disks, it was observed that for certain temperature ranges the disks form hexagonally packed columnar structures when the tethers are bonded equatorially to the disks and sheets when the tethers are attached to opposite faces. In the study of di-tethered spheres, the nanospheres self-assembled into cylindrical shells, spherical shells, or mono-layers depending on the tether length and system temperature. In the study of mono-tethered spheres, it was found that switching the solvent selectivity from being poor for the tether to good for the tether resulted in a change from self-assembled micelles to bilayer sheets. Further it was predicted that unlike in surfactants and flexible diblock copolymers, the rigidity of a nanorod in a tethered nanorod system induces liquid crystalline ordering, forming a lamellar smectic C structure. A host of other studies have been undertaken looking at mono-tethered nanospheres(66; 67; 68; 69), di-tethered nanospheres (70; 71), tethered rods (72; 73; 74; 68), tethered POSS cubes(75; 76; 77), and tethered Vs (78); many of these studies will be discussed in detail in the following chapters.

2.5 Axes of anisotropy

A first step to understanding the self-assembly of tethered nanoparticles is to understand the various levels of anisotropy inherent to the building blocks. Anisotropy can manifest itself in many ways; the most obvious place it appears is within the shape of the nanoparticle. For example, we would expect that a tethered nanorod would adopt different local packing than a tethered nanosphere as a result of the different shape of the nanoparticle. More subtle anisotropy arises as a result of the number of tethers, length of the tether, location of tether, and specificity of interactions. For example, we expect the structure formed by a di-tethered nanosphere would be heavily dependent on the relative location of the two tethers, e.g. diametrically opposed verses attached to the same location. In reference (18) we classified several key axes of anisotropy for tethered nanoparticles, as shown in figure 2.1. In figure 2.1, axis *A* classifies the number of tethers attached to the nanoparticle and axis *B* classifies the relative length of the tether, which both can be varied independently. Axis *C* refers to the nanoparticle shape, arising form the number of vertices, and as previously mentioned, may

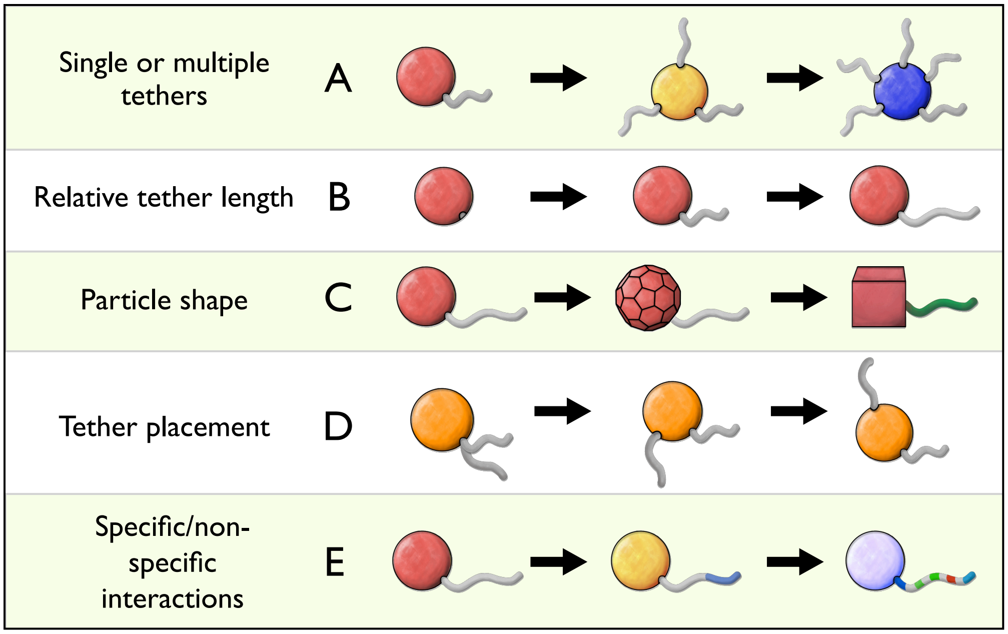

Figure 2.1 Classification of tethered nanoparticle "shape amphiphiles" anistropy. Various building blocks are classified according to a particular measuresof anisotropy: (a) Number of tethers, (b) relative length of tether/relative size of nanoparticle, (c) Number of nano particle vertices, (d) Relative location of tethers, (e) Tether interaction specificity. This is only a subset of possible axes and subset of possible combination of axes. Complex anistropies can be described by a combination of more simple dimensions. Reproduced from reference (18)

have a large impact on the local crystalline and liquid crystalline packing of the nanoparticles. Axis *D* classifies the placement of the tethers on the nanoparticle; the location of the tethers may strongly impact the directionality of the tether-tether interactions. Axis *E* refers to the specificity of the tether-tether interaction, ranging from a homopolymer to lock-and-key specificity of DNA. Experiments within this thesis were conducted to conform with the axes of anisotropy in figure 2.1 to elucidate the role of relative nanoparticle size, nanoparticle geometry, tether location, and tether interaction.

Chapter 3

Simulation models and methodology

3.1 Simulation models

To study tethered nanoparticles, we consider a general class of tethered nanoparticles rather than any one specific system and use empirical pair potentials that have been successful in the study of block copolymers and surfactants (79). We utilize minimal models that capture the essential physics of the problem. Specifically our model is designed to capture:

- geometry of the nanoparticle
- immiscibility between tethers and nanoparticles
- flexibility of the polymer tethers
- attachment location of the tether(s) on the nanoparticle

In this thesis, we examine the phase behavior of mono- and di- tethered nanospheres and compare with tethered nanorods, diblock copolymers and surfactants. We utilize short-ranged Lennard-Jones-like potentials to model the interactions between the individual components in our system. In our studies, we incorporate amphiphilicity through solvent selectivity. Solvent selectivity is modeled by treating "solvent-phobic" and "solvent-philic" beads with different potentials. To model attractive, solvent-phobic interactions, we utilize a shifted form of the Lennard-Jones (LJ) potential, given by:

$$U_{LJ}(r) = \begin{cases} 4\varepsilon \left(\frac{\sigma^{12}}{(r-\alpha)^{12}} - \frac{\sigma^{6}}{(r-\alpha)^{6}} \right) - U_{shift} \,, & r - \alpha < r_{cut} \\ 0 \,, & r - \alpha \geq r_{cut} \end{cases} \tag{3.1}$$

where ε is the attractive well depth, U_{shift} is the energy at the cutoff, and $r_{cut} = 2.5\sigma$. The parameter α is used to shift the interaction to the surface of a bead with radius larger than σ to properly account for excluded volume, such as for our model nanospheres. α is determined by calculating $\alpha = (D_i - \sigma)/2 + (D_j - \sigma)/2$, where D_i and D_j are the diameters of our two interacting particles. This calculation effectively creates a system where there is a "ghost" particle with diameter σ at the surface of our larger particles. It is important to

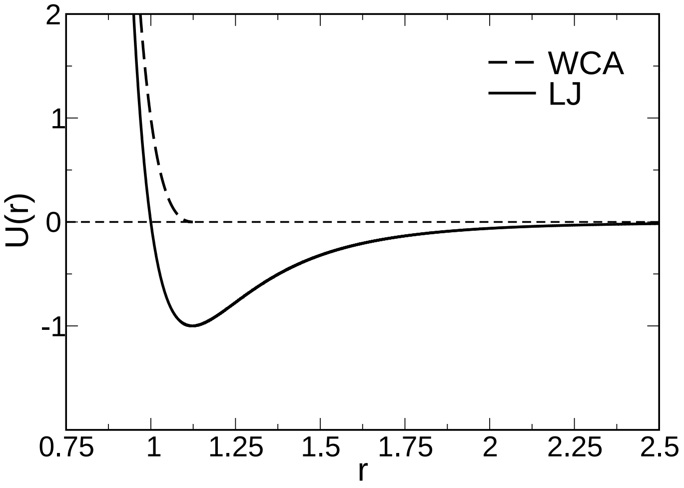

Figure 3.1 Plot of the Lennard-Jones (LJ) potential and Weeks-Chandler-Andersen (WCA) potential.

note that when the diameters of our two particles are σ, α reduce to 0.

To capture non-attractive, solvent-philic interactions, we utilize the purely-repulsive Weeks-Chandler-Andersen (WCA) potential which captures excluded volume and very short ranged-repulsion. The WCA potential can be described by the LJ equation (eqn. 3.1), with $U_{shift} = \varepsilon$ and $r_{cut} = 2^{1/6}\sigma$. Under neutral or melt-like solvent conditions, all like species are modeled using the LJ potential and all dislike species are modeled using the WCA potential.

The connectivity between beads is modeled using finitely extensible non-linear elastic (FENE) springs(80). The FENE spring is given by:

$$U_{FENE}(r) = -\frac{1}{2}kR_o^2 ln\left[1-\left(\frac{r-\alpha}{R_o}\right)^2\right] \tag{3.2}$$

where k is the spring constant, R_o is the maximum allowable separation, and α is the same shifting parameter described above. The FENE spring has a maximum separation preventing unphysical chain crossings. Within this thesis, all systems utilizing the FENE interaction have k=30 and R_o= 1.5. In select cases, such as setting the planar angle in di-tethered nanospheres (discussed in chapter 8 and below), harmonic springs are used. The harmonic spring is given by:

$$U_{harmonic}(r) = -\frac{1}{2}k(r-R_o)^2 \tag{3.3}$$

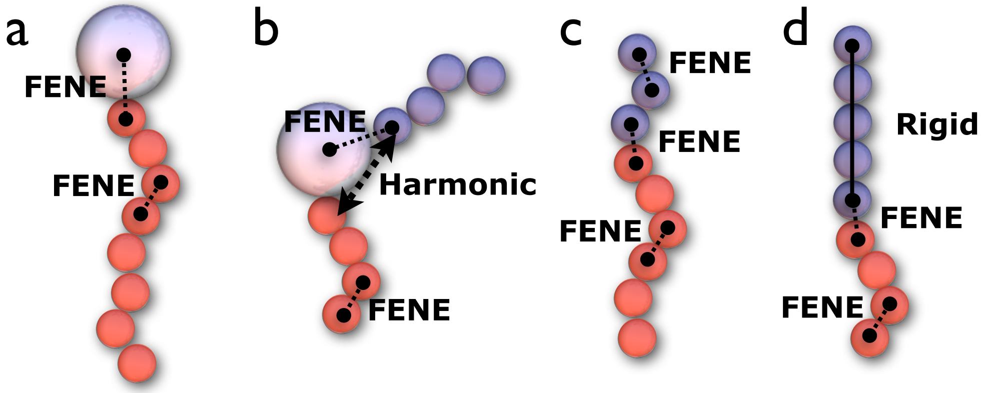

Figure 3.2 **(a)** Schematic of a mono-tethered nanosphere, **(b)** schematic of a di-tethered nanosphere **(c)** schematic of a flexible amphiphile, and **(d)** schematic of a tethered nanorod. Representative labels of the connectivity used are labeled in the figures.

where the spring constant, k=30 and R_o is the equilibrium separation.

Our basic model of a mono-tethered nanosphere consists of a sphere of diameter D connected via a FENE spring to an N-bead polymer chain, where FENE springs are also used to model the connectivity between beads in chain; a schematic of this building block is shown in figure 3.2a. The amphiphilic interactions between individual beads are governed by solvent-selectivity discussed above. Di-tethered nanospheres are modeled similarly, but instead two polymer tethers are attached with FENE springs to our nanosphere. The angle between the two polymer tethers is controlled by using a harmonic spring between the first beads of the tethers, as shown in figure 3.2b. Diblock copolymers and surfactants are modeled as two FENE polymer chains of length N_A and N_B connected together by a FENE spring, as shown in figure 3.2c. Tethered nanorods are modeled in a similar fashion to diblock copolymers, however one block is composed of a rigid collection of beads, as shown in 3.2d. The specific individual models used are discussed in their corresponding sections.

The natural units of these systems are: σ, the diameter of a tether bead; m, the mass of a tether bead; and ε, the Lennard-Jones well depth. Bulk system volume fraction, ϕ, is defined as the ratio of volume of the beads to the system volume, the dimensionless time is $t^*=\sigma\sqrt{m/\varepsilon}$, and the degree of immiscibility and solvent quality are determined by the inverse temperature, $1/T^* = \varepsilon/k_BT$.

3.2 Brownian dynamics method

There are several computational methods that can be employed to study the self-assembly and phase behavior of tethered nanoparticle and polymeric systems. These methods include Brownian dynamics (BD), molecular dynamics (MD), dissipative particle dynamics (DPD), and Monte Carlo (MC). BD was chosen over the other methods for several reasons. First, BD allows for longer timescales than MD by eliminating the need to explicitly model solvent particles; the dissipative and random forces inherent in BD implicitly include solvent effects and also allow for larger timesteps. DPD is a mesoscale method that allows for even longer timescales than BD, however, this gain comes at a price. In DPD, beads represent fluid elements and all interactions are treated with short-ranged, soft, repulsive interactions that allow particles to pass through each other–since particles can pass through each other, capturing the geometry and excluded volume of a nanoparticle is a challenge. Many of our studies are conducted at high density states, making an off-lattice MC method potentially slow to explore phase space. Lattice-based MC simulations perform better at high density states, however, the lattice may be incapable of properly capturing the geometry of our nanoparticles.

To properly include nanoparticle geometry and allow for the realization of longer time scales and larger number of tether nanoparticles, surfactants, and block copolymers, we utilize the BD method. As shown by reference (80; 81; 82), BD is capable of capturing the appropriate details of the simulations for surfactants and block copolymers, while making the simulations less computationally expensive. BD is a subset of Langevin dynamics wherein the trajectory of each "bead" is governed by the Langevin equation:

$$m_i \ddot{\mathbf{r}}_I(t) = \mathbf{F}_i^C(\mathbf{r}_i(t)) + \mathbf{F}_i^R(t) - \gamma \mathbf{v}_i(t) \tag{3.4}$$

where m_i, $\mathbf{r}_i$, $\mathbf{v}_i$, $\mathbf{F}_i^C$, $\mathbf{F}_i^R$ and γ_i correspond to the mass, position, velocity, conservative force, random force, and friction coefficient of bead i, respectively (80). We assume that there are no spatial or temporal fluctuations in the friction coefficient and fix $\gamma_i = 1.0$ which limits the range of ballistic motion of a bead to approximately 1.0σ. The random force is independent of the conservative force and satisfies the fluctuation-dissipation theorem:

$$\begin{aligned} &\langle \mathbf{F}_i^R(t) \rangle = 0 \\ &\langle \mathbf{F}_i^R(t) \mathbf{F}_j^R(t') \rangle = 6\gamma k_B T \delta_{ij} \delta(t - t') \end{aligned} \tag{3.5}$$

The friction coefficient and random force act as a non-momentum-conserving heat bath; the combination of these two terms helps to minimize numerical roundoff errors that can occur over long simulations runs. The stationary solution of the Langevin equation is the

Boltzmann distribution and therefore BD samples the canonical (NVT) ensemble. In our simulations, solvent particles are not explicitly included; however, the frictional and random forces in the Langevin equation help to implicitly account for some of the effects of solvent (e.g. random bombardment and viscosity). It is important to note that BD does not include hydrodynamic interactions, however, we showed that this is unimportant to the resulting equilibrium morphology or the time to order for block copolymer systems in reference (72).

Particle beads are advanced through time using the leapfrog algorithm (83). A timestep of Δ t=0.01 is utilized for almost all tethered systems; high temperature and high density often required a smaller timesteps, with Δ t=0.005. For studies of linear nanorod building blocks, the equations of rotational motion of linear are objects are implemented to properly account for rotational degrees of freedom (84).

3.2.1 General simulation procedure

We employ a similar simulation procedure for most of the systems simulated in this dissertation. First, individual building blocks are initialized on a simple cubic lattice within the simulation box. Individual bead-bead interactions are treated using the purely repulsive WCA potential. This allows the system to melt off the lattice and become well mixed without a strong desire to phase separate; alternatively this can be thought of as equivalent to running at high temperature, well above the order-disorder transition. After this initialization stage, bead-bead interactions are set to their prescribed potentials. The system is then incrementally cooled. For each temperature, the system is allowed to run for several million time steps, allowing it to reach equilibrium at that statepoint. The potential energy is monitored and allowed to fully reach a minimum to help ensure that equilibrium is reached.

Simulation caveats

This simulation procedure does not completely ensure that a global minimum in the free energy landscape is achieved, but rather only that a low-energy, local minimum is achieved. To help ensure that we have reached a global equilibrium and not just a metastable state, we perform multiple, independent cooling sequences to establish path independence and reproducibility of our results. By performing several independent runs we decrease the likelihood of exploring the same regions of phase space. Since we often perform a series of simulations as a function of, for instance, volume fraction, we can gain additional confidence in our results by considering our closely related neighboring phases.

Additionally, we typically perform simulations at multiple system sizes to ensure that our structures are not a result of finite size effects. Phases that are triply periodic (e.g. BCC ordered micelles and the double gyroid network) are particularly sensitive to box size, requiring a system size that is commensurate with the periodic spacing of the structure. Performing simulations that include multiple unit cells in each direction often avoids many of the box size issues associated with small systems, however such systems may be computationally intractable.

Systems with 2D periodicity (e.g. hexagonally packed cylinders) or 1D periodicity (e.g. lamellar sheets) can orient themselves within the box to find the appropriate spacing under most conditions. In these cases, the structures do not form parallel to any of the principle axes in the system. Care should be taken if the structure is oriented in the box such that its periodic direction(s) are oriented along the largest direction(s) (i.e. the diagonal(s) of the box). This condition suggests that the structure requires a larger periodic spacing than the box can accommodate and as such, larger systems should be explored; this does not necessarily mean that the bulk classification of the structure is wrong, but rather that the potential energy, order-disorder transtion, and periodic spacing may not be correct. Two commonly encountered situations occur when the normal of a lamellar sheet is parallel to the diagonal of the cubic simulation box and when the long axis of a cylinder is parallel to the diagonal of the cubic simulation box. Additionally, this behavior can be evaluated by calculating the stress tensor and comparing the values of the diagonal components; if the diagonal components of the stress tensor are not approximately equal, the system is likely to be experiencing finite size effects.

The box length search algorithm developed by Schultz, *et al.* (85) has been successfully used to orient 1D and 2D structures along the principle axes of the simulation box by distorting the simulation box shape so as to equalize the pressure in each direction. However, it is often easier to manually calculate the approximate periodic spacing of a non-aligned system and adjust the system size appropriately in a separate simulation to achieve alignment with the principle axes.

Chapter 4

Analysis methods

To analyze the results of the simulations presented in this thesis, we utilize a variety of analysis techniques. In this chapter we discuss novel analysis methods developed and applied in this dissertation. In section 4.1 we discuss the R$_{ylm}$ method based on spherical harmonics that we developed in references (67; 68). The R$_{ylm}$ method is used to determine the local structure of particle aggregates. In section 4.2 we outline a method for calculating the center of mass of spherical aggregates utilized in references (71; 86) that is an extension of an image processing technique typically used in the colloidal community. In section 4.3 we discuss the bond order diagram used to determine the structure of bulk crystalline materials utilized in references (71; 86). Other common analysis methods utilized are discussed in Appendix B.

4.1 R$_{ylm}$ method

The structures formed by tethered nanoparticles often contain multiple levels of ordering. Within these structures, nanoparticles and micellar aggregates typically adopt ordered local configurations that we would like to identify and quantify. In references (67; 68) we introduced the R$_{ylm}$ method based on spherical harmonics (87) to determine the structure of nanoparticles/micelles. The general R$_{ylm}$ method relies on creating a rotationally invariant spherical harmonic "fingerprint" of a structure and using a matching metric to determine the best match from a library of known structures.

The first step in this procedure is to determine our nearest neighbors. We use a simple cutoff based procedure (e.g. any particles that are closer than the cutoff are neighbors). The cutoff is set such that it encompassed the first peak of the pair correlation function, g(r). Note that since our systems utilize periodic boundary conditions we use the minimum image convention to construct our clusters. Next we calculate the spherical harmonics fingerprint. To calculate the fingerprint, we first calculate q_ℓ^m by summing over all nearest neighbor directions between particles:

$$q_\ell^m = \frac{1}{N_b}\sum_{N_b}^{j=1} Y_{\ell m}\left[\theta(\hat{r}_{i,j}), \phi(\hat{r}_{i,j})\right],$$

where $\hat{r}_{i,j}$ is the vector drawn from particle i to its nearest neighbor j, N_b is the total number of neighbors, ℓ is the specific harmonic, and $Y_{\ell m}$ is the spherical harmonic expansion (87). From this we can construct two rotationally invariant measures of cluster shape, Q_ℓ, the vector magnitude of q_ℓ^m, and w_ℓ, the rotationally invariant combination of the average values of q_ℓ^m (87). As defined by Steinhardt, *et al.* :

$$Q_\ell = \left((4\pi/(2\ell+1))\sum_{m=-\ell}^{\ell}|q_\ell^m(i)|^2\right)^{1/2},$$

$$w_\ell = \frac{\sum\limits_{\substack{m_1,m_2,m_3 \\ m_1+m_2+m_3=0}} \begin{pmatrix} \ell & \ell & \ell \\ m_1 & m_2 & m_3 \end{pmatrix} q_\ell^{m_1}(i) q_\ell^{m_3}(i) q_\ell^{m_3}(i)}{\left(\sum\limits_{m=-\ell}^{\ell} |q_\ell^m(i)|^2\right)^{3/2}},$$

where $\begin{pmatrix} \ell & \ell & \ell \\ m_1 & m_2 & m_3 \end{pmatrix}$ is the Wigner 3j symbol(87).

Our fingerprint is composed of the Q_ℓ and w_ℓ values for l = 4, 6,...12. Table 4.1 shows fingerprints of some commonly found structures, including BCC, FCC, HCP, and an icosahedron. To determine our local configuration, the residual value with respect to a library of known structures with matching coordination is calculated (67):

$$R_i = \sqrt{\sum_{l=4}^{12}\left(Q_l - Q_{ref_i}\right)^2 + \sum_{l=4}^{12}\left(w_l - w_{ref_i}\right)^2}.$$

A particle is considered to be in the local configuration i that minimizes the residual R_i. Since there is no way to construct a disordered configuration, a particle is considered to be disordered if the residual value exceeds a certain cutoff. The value of the residual cutoff is a subjective measure of how much disorder we are willing to accept in our configuration; a small value of the residual cutoff will make the structure classification more sensitive to thermal disorder.

The R$_{ylm}$ method is well suited to accurately identify particle configurations as it provides a rotationally invariant description of a local structure and does not rely on multiple cutoff values to determine the configuration, minimizing potential error. Additionally, this metric relies on a variety of harmonics, not just one or two, allowing for better differentiation between structures. This method also has the advantage that we can evaluate a match with any arbitrary structure, not just mathematically perfect ones. This allows us to compare with non-ideal structures, such as an icosahedron missing particles, as we do in chapters 5 and 6.

Table 4.1 Common spherical harmonics fingerprints. Note that BCC, FCC and HCP are mathematically perfect structures, while the icosahedra (Z12) is a thermally cluster from simulation.

	Q4	Q6	Q8	Q10	Q12	w4	w6	w8	w10	w12
BCC	0.036	0.511	0.429	0.195	0.405	0.159	0.013	0.058	-0.090	-0.050
FCC	0.191	0.575	0.404	0.013	0.600	-0.159	-0.013	0.058	-0.090	0.087
HCP	0.097	0.485	0.317	0.010	0.565	0.134	-0.012	0.051	-0.080	0.095
Z12	0.028	0.653	0.052	0.355	0.555	-0.036	-0.169	0.007	-0.090	0.096

It should be noted that this method is only as good as the library of known structures. It is impossible to determine a match that is absent from the library. Thus it is important to have a robust library of possible structures to avoid making erroneous structure assignments.

4.1.1 Average descriptors

Rather than matching the ylm fingerprint of individual clusters, we can average together the individual fingerprints to create a single fingerprint that describes the system (i.e. an average descriptor). This average descriptor can then be compared with a reference library to determine the average order of a system.

Alternatively, we can compare the average descriptor to a single descriptor of another system or another point in time, providing us an easy to construct order parameter. This is particularly useful for comparing the evolution of periodic structures. An average descriptor order parameter is used in chapter 7.

4.2 Center of mass calculation

To analyze and classify spherical micelle structures it is often necessary to locate the center of mass of each micelle. The center of mass is often calculated using a recursive neighboring routine. A recursive technique can be computationally expensive and has the additional drawback that it requires the micelles be well spaced. If micelles are not well spaced, two neighboring micelles may be incorrectly considered a single micelle. Another common technique is to calculate the Fourier transform of the system in 3-d followed by the inverse transform of the main peaks. This technique works well, but requires that micelles are arranged in a periodic crystal; this method would not work for a system of disordered spherical micelles or in quasicrystalline materials that lack translational symmetry.

To approximate the center of mass we modified an image processing technique that is typically used to identify the center of colloidal particles from microscopy data, developed by Crocker and Grier (88) and later extended to 3D systems by Varadan and Solomon (89) . This technique only requires that the micelles are roughly monodisperse in diameter. In this method, we start by constructing a density profile of the system by creating a 3-d grid of cubic cells and calculating the number of particles in each cell (i.e. we convert our position data to voxels). We then apply a 3-d Gaussian filter to the density data where the diameter of the filter corresponds to the approximate diameter of the spherical micelles. This weights the center of a spherical object greater than the edges. It is important to note that any filter that associates a high weight to the center should work for this application. We then calculate the cell with the highest weighted value in each region, where a region is defined by the approximate diameter of the micelles. This calculation produces a set of cells that correspond to the centers of mass of the micelles in the system. A schematic of this method applied to a 1-d density profile is shown in figure 4.1.

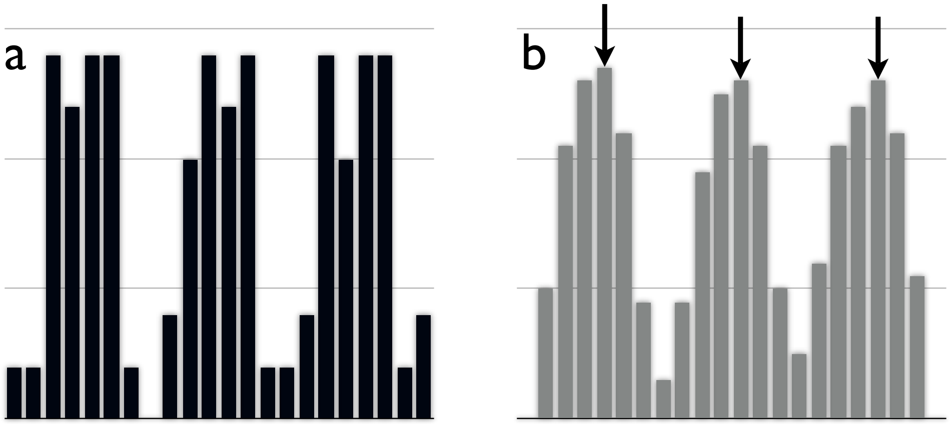

Figure 4.1 **(a)** 1-d example of a density profile. **(b)** The density profile shown in **a** processed with a Gaussian filter. The arrows indicate the local maximum that are identified as micelle centers of mass.

Accuracy of this calculation can be increased by using many closely spaced snapshots to construct the density profile, e.g. using 50 snapshots spaced 50 timesteps apart to average over the time-dependent shape of the micelles. It is important to make sure that the snapshots occur in a small enough time window that the bulk structure is still correlated.

To avoid artifacts of the size of the grid (i.e. locations that are integer multiples of grid size), several different methods can be used. The simplest method is to use a small grid size to better approximate a continuous density profile. However, as the grid size becomes smaller than the characteristic dimension (i.e. size of the smallest particle), it is necessary to create the density profile using multiple snapshots, to avoid having “holes” (i.e. empty cells) within the micelles. In general, the more snapshots averaged over, the smaller the grid size that can be used. Another method to avoid artifacts requires calculating the centroid around each center-of-mass cell, as is typically done in colloidal applications (88). Additionally, performing the calculation at different grid sizes and averaging together the results should also avoid artifacts; note that either cell positions or centroid data can be averaged together to improve accuracy.

4.3 Bond order diagram

To identify orientational order, we utilize the bond order diagram (BOD). The BOD shows the directions of all vectors drawn from a particle or micelle to neighboring particles/micelles projected on the surface of a sphere, creating an “average” picture of the orientational order in the system. Systems that have highly correlated neighbor directions (e.g. bulk crystalline materials) will show distinct groupings of points on the surface of the sphere, as shown in figure 4.2a. In contrast, a disordered system will appear as points randomly distributed on the surface, as shown in figure 4.2b.

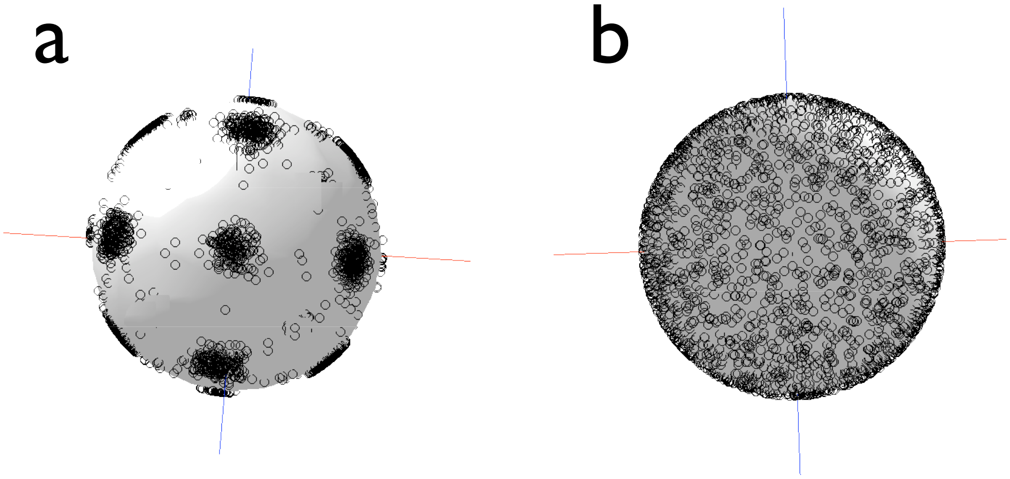

Figure 4.2 **(a)** BOD of a BCC crystal showing distinct groupings of points on the surface of the sphere. **(b)** BOD of a disordered liquid.

To calculate the BOD, we first must create clusters of particles containing neighbors. In principle, the BOD can be constructed with any number of neighboring shells (i.e. first, second, third, etc.) on a single diagram or separate diagrams. In the application of the BOD in this thesis, we utilize only the first neighbor shell (i.e. nearest neighbors). Particles are clustered using the same scheme employed in the R$_y lm$ method (see section 4.1) where two particles within a certain cutoff are considered to be neighbors; the cutoff is chosen such that it includes the first peak of the pair correlation function, g(r). Note that since our systems utilize periodic boundary conditions we use the minimum image convention to construct our clusters. Once the nearest neighbors are determined, each cluster is translated to the origin, and the distances between the center particle and neighboring particles are normalized to unity.

It is important to note that the bond order diagram is rotationally dependent; if direct comparisons are going to be made between a two systems, care should be taken to properly orient the two BODs. Alternatively, this information can be presented in the form of a histogram on the surface of a sphere (commonly known as the shape histogram (90)). A histogram will properly weight each region of the sphere, making areas with highly correlated bond angles more apparent and suppressing thermal noise. However, in most cases, the calculation of the shape histogram is not necessary.

Chapter 5

Mono-tethered nanospheres

One of the simplest examples of a tethered nanoparticle is the mono-tethered nanosphere. Mono-tethered nanospheres are composed of a single polymer tether attached to the surface of a uniform spherical nanoparticle. This building block can be thought of as replacing the headgroup of a surfactant, or alternatively replacing one of the blocks of a diblock copolymer, with a large sphere. Due to the architectural similarities with surfactants and diblock copolymers, we expect mono-tethered nanospheres to exhibit similar morphologies and phase behavior trends. In this chapter we investigate the behavior of a model system of mono-tethered nanoparticles to 1) predict the possible morphologies, 2) understand the similarities and differences with flexible amphiphiles, and 3) create a datum for future studies of tethered nanoparticle shape amphiphiles. In particular, we are interested in the extent to which a tethered nanosphere qualitatively behaves like a traditional surfactant molecule. We first investigate a system where the solvent is good for the nanoparticle (i.e. the tethers wish to aggregate). Within this context, we explore the role of volume fraction, immiscibility, and nanoparticle diameter on the phase behavior and compare this with surfactant systems. We predict that in contrast to flexible amphiphiles the nanospheres are locally ordered and there is an increase in the local order with an increase in volume fraction or relative nanoparticle diameter. We present the temperature vs volume fraction phase diagram for a system of mono-tethered nanospheres and propose a dimensionless scaling factor F_v (headgroup volume/tether volume) that allows a comparison between the morphologies formed from mono-tethered nanospheres and traditional surfactants. This work is published in reference (66). We next investigate a system where the solvent is poor for the nanosphere (i.e. the nanospheres wish to aggregate) and explore the role of volume fraction, immiscibility, and confinement on the overall phase behavior. We show that microphase separation of the immiscible tethers and nanospheres causes confinement of the nanoparticles. We find a predominance towards icosahedral ordering between the nanospheres for systems with 2D confinement, and crystalline ordering for systems with 1D confinement. This work is published in reference (67).

5.1 Phase behavior of tethered aggregating nanospheres

An impressive variety of nanoparticles of different materials and geometries has been synthesized (1), including but not limited to Au nanospheres (34; 53; 91; 3; 35; 39), Ag nanocubes and polyhedra (41; 36; 40), $Al(OH)_3$ platelets (92; 4), Ag (3; 37) and Au (93) triangles, etc (1; 38; 6). This vast library of nanoparticles will provide the building blocks for tomorrows materials (94) if they can be assembled from the "bottom up" into ordered arrays. Bottom-up assembly provides an unprecedented number of opportunities for engineering novel materials with specific physical properties. However, the size scale and potentially large number of nanoparticles required to assemble macroscopic materials precludes mechanical methods as a viable means for bottom-up assembly. Self-assembly is generally regarded as a promising means to reliably facilitate the assembly of large numbers of nano building blocks (NBBs) into desirable structures (11), but a predictive theory of assembled phases for nanoparticle systems is not yet in hand.

Functionalization of nanoparticles with a small number of oligomeric or polymeric tethers (17) is a novel strategy to induce the self-assembly of NBBs in a predictable and controllable manner. In this scheme, thermodynamic immiscibility between nanoparticle and tether, induced by temperature, concentration, or solvent selectivity, facilitates assembly and the building block topology and nanoparticle shape influence the structure formed by the self-assembly process (17). To this extent, recent advances in synthesis techniques are providing ever-increasing control over the size and shape of nanoparticles and it is now possible to attach a small number of polymer tethers to specific locations on the surface of the nanoparticles (53; 54; 52; 56; 57; 58; 59; 60; 62), creating "shape amphiphiles" (95) with controlled topology. For example, Westenhoff and Kotov attached a single tether to the surface of a CdTe quantum dot (58); Alivisatos and coworkers demonstrated their ability to attach one, two, three, or more tethers to the surface of spherical, Au nanoparticles (96); Stellacci and coworkers developed a technique that allows them to pattern the surface of spherical, Au nanoparticles with rings of tethers (34) or to attach diametrically opposing carboxylic acid tethers to Au spheres (63). These and other tethered nanoparticles (97) serve as a proof of concept and represent substantial progress toward realizing NBBs with specific geometry and topology. It may be expected that shape amphiphiles will self-assemble into microphases similar to those observed in block copolymers (BCP) and surfactants and that the underlying self-assembly process is governed by similar physics, whereby systems seek to minimize their free energy through aggregation of like species. One distinct difference between tethered NBBs and BCPs and surfactants is that the "head" groups of the NBBs are rigid, resulting in a large excluded volume for which the effects on the self-assembly process are unclear. The overall concentration-dependent phase behavior of surfactant solutions has been studied computationally via lattice and off-lattice Monte Carlo (MC) (98; 99), most notably by Larson (22; 23). Computational studies of surfactants using molecular and Brownian dynamics methods have thus far been limited to small regions of the phase diagram (81; 82; 100; 101; 102; 103; 79; 104; 105). Recently, Bourov and Bhattacharya studied a two- and three-dimensional system of surfactants with large head groups (100; 101). In their study, they used a model and method similar to that proposed by Zhang, *et al.* (17) where the surfactant was modeled as a large spherical particle permanently bonded to a flexible chain. They showed the impact of head group size on the critical micelle concentration was commensurate with experimental predictions. Since their work was limited to the study of micelles (100; 101) the effects of a large rigid head group on other phases was not reported. We report such effects here.

5.1.1 The role of volume fraction, immiscibility, and nanoparticle diameter

To explore the impact of nanoparticle diameter on the overall phase behavior of TNS, we have conducted a series of studies where the length of the bead-spring tether is fixed and the nanoparticle diameter is varied. Simulations are performed for a tether length of 8 beads of diameter σ and nanoparticle diameters of $D = 1.5\sigma$, 2.0σ, and 2.5σ. The nanospheres are modeled as being in a good solvent and the tethers in a bad solvent. Thus, tethers aggregate and are treated using the Lennard-Jones (LJ) potential and nanospheres are modeled using the Weeks-Chandler-Andersen (WCA) potential, as discussed earlier in section 3.1. For direct comparison to surfactant systems, we also study flexible chains of two head beads (h2t8) and eight head beads (h8t8) all with tether length of 8 beads. Surfactant tails are modeled as being in poor solvent, thus treated with the LJ potential, and head groups are modeled as in good solvent, and thus treated with the WCA potential, as outlined in section 3.1. The method of Brownian dynamics (BD) is utilized, as discussed in section 3.2. We present a temperature vs. volume fraction phase diagram for a three-dimensional system of TNS and compare the TNS phase diagram to that of surfactants. We further present a "phase diagram" given by a scaling factor, (F_v) = (head-group volume/tether volume), plotted versus volume fraction (i.e. concentration), ϕ. We predict the existence of three distinct regimes in the phase behavior of TNS. The first regime is where the head group volume is small compared to the tether volume and lamellar phases are predominant, the second regime is where head-group and tether volumes are similar, resulting in a rich combination of phases, and the third is where the head group volume is larger than the tether volume and

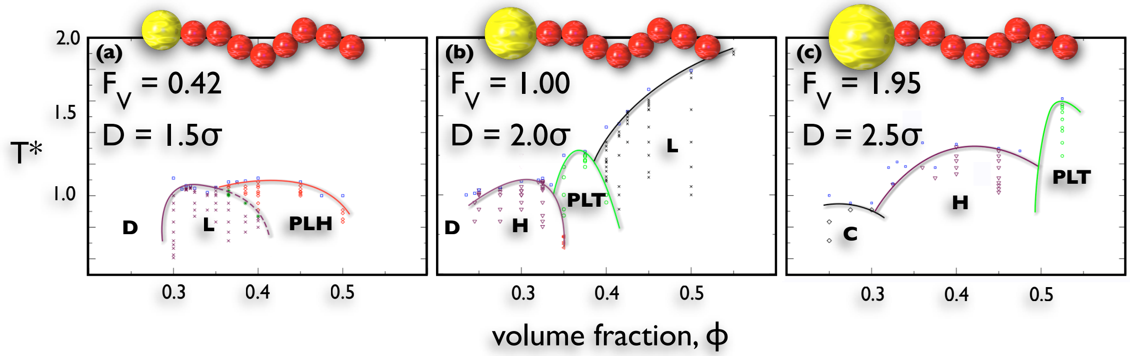

Figure 5.1 Temperature vs. ϕ phase diagrams for h1t8 TNS systems, with schematic representations of simulated TNS displayed above diagrams. Data points indicate performed runs. Phases are defined as lamellae (L), perforated lamellae through the head group (PLH), hexagonally packed cylinders (H), perforated lamellae through tethers (PLT), cubic ordered spherical micelles (C). **(a)** Phase diagram for TNS with particle diameter $D = 1.5\sigma$, **(b)** particle diameter $D = 2.0\sigma$, **(c)** particle diameter $D = 2.5\sigma$. In **(a-c)**, the phase boundaries are approximate and drawn as guides for the eye. Reproduced from reference (66).

phases with high a high degree of curvature are dominant.

Nanoparticle volume smaller than tether volume

We predict for TNS with a nanoparticle diameter of $D = 1.5\sigma$ and a fully extended tether length of 8σ that the equilibrium structures are limited to sheet-like (lamellar) structures over a wide range of concentrations, ϕ ∼0.3-0.5, as shown in the phase diagram presented in Figure 5.1a. For ϕ ∼0.3-0.35 we observe the formation of lamellar (L) sheets for temperatures below the order-disorder temperature, T_{ODT}. For ϕ ∼0.35-0.4, we observe the formation of a perforated lamellar phase (PLH) for higher temperatures and the formation of a lamellar phase for lower temperatures provided $T<T_{ODT}$. For ϕ ∼0.4-0.5, we predict only the PLH phase, shown in Figures 5.2a-b. The PLH phase observed for the higher volume fractions is limited to perforations through the layer formed by the head group; in contrast, the inverse of this–the perforated lamella through the tether region (PLT)–is typically reported for surfactant systems (shown in Figures 5.2c-d). For concentrations outside those discussed above the system is either disordered or comprised of disordered micelles.

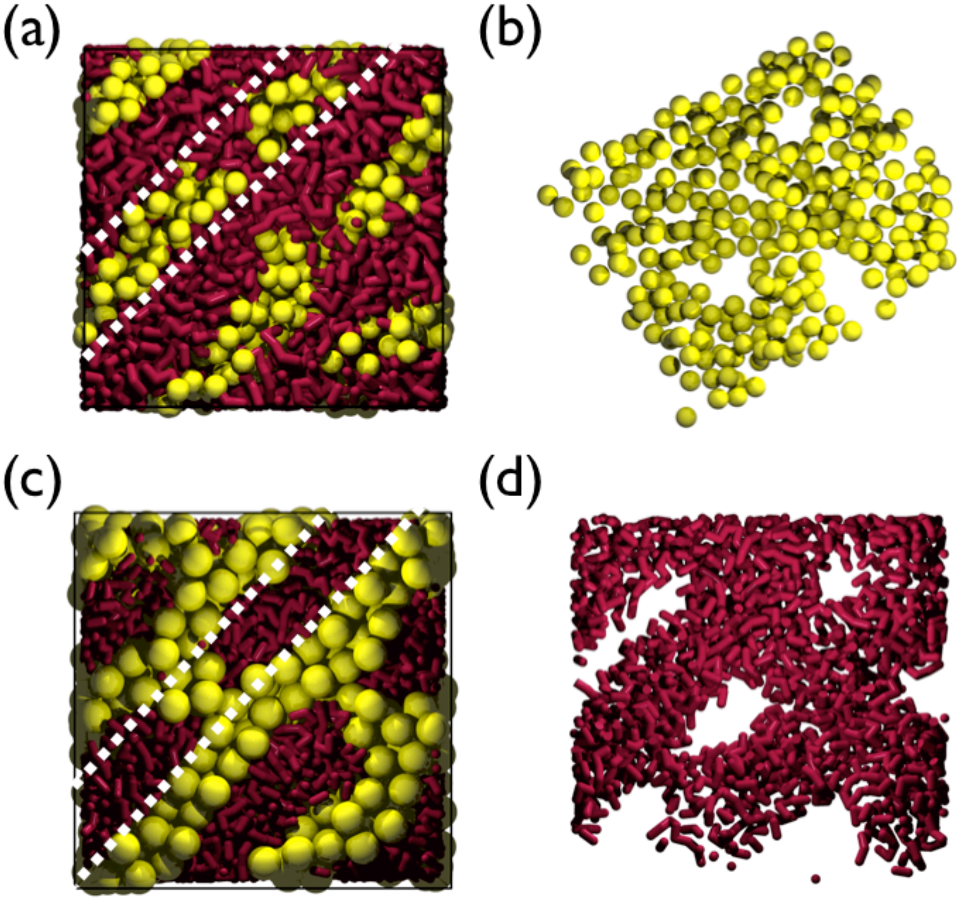

Figure 5.2 **(a)** Perforated lamella through the heads (PLH) for $D = 1.5\sigma$, $\phi = 0.45$, T* = 1.0. **(b)** A single sheet showing perforations as dotted in **(a)**. **(c)** Perforated lamella through the tethers (PLT) for $D = 2.5\sigma$, $\phi = 0.525$, T* = 1.5. **(d)** A single sheet showing perforations as dotted in **(d)**. Reproduced from reference (66).

Nanoparticle volume as large as tether volume

For a nanoparticle diameter of $D = 2.0\sigma$ connected to a tether with a fully extended length of 8σ, we observe the formation of hexagonally packed cylinders (H), lamellae (L), and perforated lamellae (PLT), where the perforations are through the tether layers, as shown in the phase diagram presented in Figure 5.1b. For ϕ ~0.25-0.35 we observe the formation of the H phase (a simulation snapshot is shown in Figure 5.3a), for intermediate ϕ ~0.35-0.4 we observe the PLT phase, and for ϕ ~0.4-0.55, we observe the L phase (a simulation snapshot is shown in Figure 5.3b). Here the volume of the head group is equivalent to the volume of the tether and for most of the phase diagram sheet-like structures are favored. However, in contrast to the case with the small head group we observe the formation of a curved structure, the H phase, at lower concentrations.

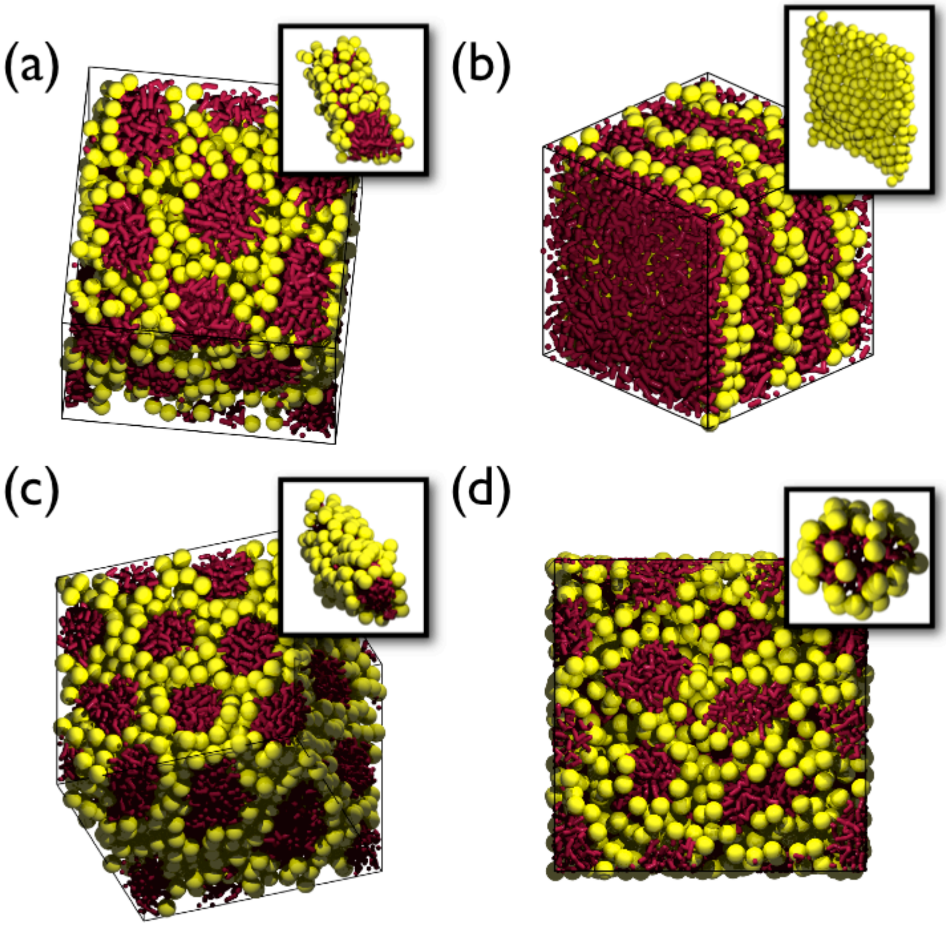

Figure 5.3 **(a)** Hexagonally packed cylinders (H) for $D = 2.0\sigma$, $\phi = 0.3$, T* = 1.0. **(b)** Lamellar bilayers (L) for $D = 2.0\sigma$, $\phi = 0.55$, T* = 1.8. **(c)** Hexagonally packed cylinders (H) for $D = 2.5\sigma$, $\phi = 0.45$, T* = 1.25. **(d)** Cubic ordered micelles for $D = 2.5\sigma$, $\phi = 0.275$, T* = 1.2. Reproduced from reference (66).

Nanoparticle volume larger than tether volume

For a nanoparticle diameter $D = 2.5\sigma$ connected to a tether with a fully extended length of 8σ, we observe the formation of cubic micelles (C), hexagonally packed cylinders (H), lamellar (L), and perforated lamellar (PLT), where the perforations are through the tether layers, as shown in the phase diagram presented in Figure 5.1c. For this case, the head-group volume is larger than the tether volume and we observe the formation of an additional curved structure, cubically ordered micelles (C). A simulation snapshot of the cubically ordered spherical micelle phase is shown in Figure 5.3d. We further observe that the curved structures now dominate the majority of the phase diagram and that the only sheet-like phase is limited to the PLT phase; simulation snapshots of the PLT phase are shown in

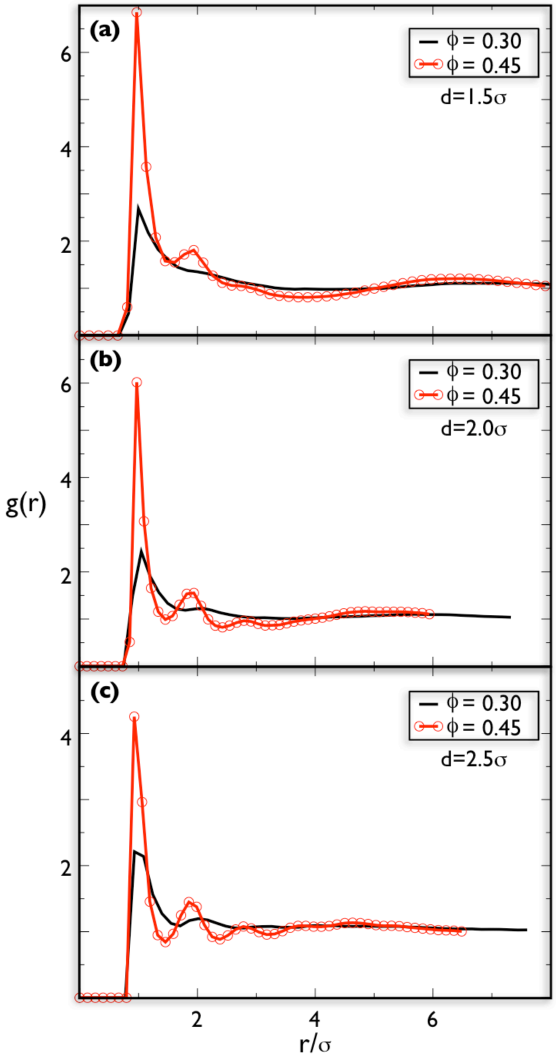

Figure 5.4 **(a)** Radial distribution function, g(r), calculated for nanoparticles (headgroups) center-to-center, for $D = 1.5\sigma$, $\phi = 0.3$ and $\phi = 0.45$, T* = 1.0. **(b)** g(r) for $D = 2.0\sigma$, $\phi = 0.3$ and $\phi = 0.45$, T* = 1.0. **(c)** g(r) for $D = 2.5\sigma$, $\phi = 0.3$ and $\phi = 0.45$, T* = 1.0. Reproduced from reference (66).

Figure 5.2c-d. Here the H phase, shown in Figure 5.3c, is stabilized over a broad range of concentrations, as compared to smaller head groups. As head group diameter is further increased to 3.0σ, this trend towards increased curvature of the assembled mesophases continues and the phase behavior is primarily limited to spherical micelles.

Discussion

We observe that as the nanoparticle increases in size relative to the size of the tether, sheet-like structures are destabilized while structures with curved interfaces are stabilized. The

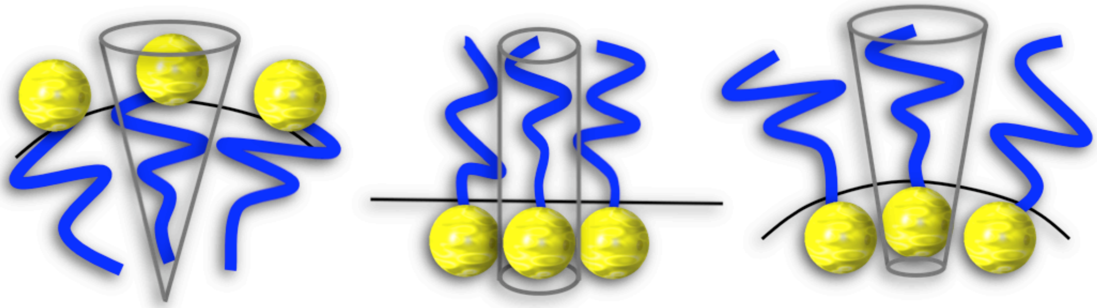

Figure 5.5 A depiction of the impact of interface curvature on the effective volume for tethered nanoparticles in three example mesophases observed. Reproduced from reference (66).

limiting case of TNS with a relatively small nanoparticle is restricted to sheet-like structures, while the limiting case of a TNS with a relatively large head group is restricted to structures with curved interfaces. For intermediate cases the phase diagram exhibits a combination of curved and sheet-like structures. In all cases of nanoparticle size, we predict an increase in the ordering of the nanoparticles (headgroups) with an increase in concentration of the system; this trend is shown by the number and intensity of peaks of the radial distribution function as concentrations of $\phi = 0.3$ and 0.45 are compared in Figure 5.4. As the system concentration is increased, the structures tend toward sheet-like structures where the nanoparticles arrange themselves within the sheets into hexagonal patterns, the most efficient packing of spheres in two-dimensions. Additionally, we predict that as particle diameter is increased, the temperature at which ordered phases form increases, as can be seen by comparing the phase diagrams represented in Figure 5.1.

The perforated lamella has been observed for surfactants both computationally(106; 72) and experimentally (107; 108) at concentrations very close to where the gyroid phase is observed (23; 107; 109). This phase can be understood as arising from a competition between the formation of curved interfaces and planar interfaces. For large nanoparticles, as concentration is increased from low to high, there is a tendency for the interface curvature to decrease; however, this behavior is to some extent mitigated by the desire of the tails to maintain maximum contact, resulting in the PLT phase (a simulation snapshot is shown in Figures 5.2c-d). Conversely, for small nanoparticles increasing concentration tends to induce inverted interface curvature because now the tails stretch, decreasing the effective grafting density of the tethers, and resulting in the PLH phase (a simulation snapshot is shown in Figure 5.2a-b). This interface behavior is illustrated in Figure 5.

This phase behavior can, in part, be rationalized by examining the packing factor, *S*, developed for surfactant systems (20). The packing factor is a purely geometric argument as to why certain structures form in surfactants. The geometry of associated structures depends upon "packing" properties of the amphiphile: the optimal area of the head group, a_o, volume of the chain, V, and the critical length of the tether, l_o :

$$S = \frac{V}{a_o l_o}.$$

It is reasonable to assume and we observe that with a fixed tether length, the effective tether volume and length remain roughly constant regardless of head size, for the range of sizes studied. The effective area depends on the square of the diameter of the head group; therefore, large diameters result in a large ao and S decreases with the square of the diameter of the head group. Based on the arguments given by Israelachvili, represented in Table 5.1, curved structures are favored for large head groups. Conversely, if the diameter is small, ao is small, and therefore S is large, favoring sheet-like and inverted structures.

Table 5.1 Values of the Israelachvili packing factor, S, and the expected structure. Adapted from ref (20).

S	Structure
$S < 1/3$	Spherical Micelles
$1/3 < S < 1/2$	Cylindrical Micelles
$1/2 < S < 1$	Flexible Bilayers
$S \sim 1$	Planar Bilayers
$S > 1$	Inverted Micelles

The Israelachvili packing factor can also help to explain the specific transitions we see regarding the perforated lamella phases. Starting from the H phase, increasing the concentration requires the head-groups to pack more densely, resulting in a decrease in ao and consequently an increase in S, favoring sheet-like structures over curved ones. If instead, we start with the L phase at low concentration and subsequently increase the concentration, a_o will again decrease, favoring structures with inverted curvature.

5.1.2 Comparison to surfactants

Since measurements of the various quantities in S are often difficult to determine, especially when trying to compare a rigid sphere to a chain, a relationship that includes easily determinable quantities should be developed to allow for direct comparison between a variety of different systems. We first discuss the comparison of the flexible head-group surfactant to the TNS. We obtain the phase behavior of a symmetric h8t8 surfactant system using our modified Larson model, where both head and tail beads are modeled as flexible chains, connected by FENE springs within a BD simulation. In the standard Larson model, a surfactant is modeled by i "head" units connected to j "tail" units, where each unit occupies a site on a simple cubic lattice (23). We find remarkable agreement with the phase diagrams plotted by Larson for h4t4 symmetric surfactant systems (23) as well as with the phase behavior mapped by Prinsen, et al. using dissipative particle dynamics (DPD) (110). Figure 5.6a shows the h2t8 surfactant phase diagram, Figure 5.6b shows the phase diagram for a system of TNS with nanoparticle diameter of $D = 2.0\sigma$, and Figure 5.6c shows the phase diagram for h8t8 surfactant (modeled systems are inset in Figure 5.6). By examining the overall behavior, it is clear that comparing amphiphiles with similar linear length, namely comparing $D = 2.0\sigma$ TNS to the h2t8 surfactant, does not provide similar results. The h2t8 system more closely resembles Figure 1a, most notably exhibiting a PLH phase as well as an inverted hexagonally-packed cylinder phase (IH), which is a natural progression as the head group gets increasingly forced into a curved structure due to the geometric constraints of the tail at high concentration. However, there are distinct similarities between the $D= 2.0\sigma$ TNS and h8t8 surfactant, and we therefore propose the following relationship be utilized:

F_v = (Excluded volume of the head)/(Excluded volume of the tail).

For both the $D = 2.0\sigma$ TNS and h8t8 systems $F_v = 1.0$, whereas the dissimilar h2t8 system has a value of $F_v = 0.25$. Examining the phase diagram presented in Figure 5.6 for the flexible surfactant, we again see the same trends with F_v as with S, since small head groups result in a small value of F_v, and F_v is large for large head groups. Applying F_v to systems studied by Larson (23) and surfactants studied in Figures 5.6a and c, we see good agreement in the trends and phase diagrams between both TNS systems and surfactants. Thus the quantity F_v allows a direct, albeit rough, comparison between computational studies of coarse-grained surfactants and TNS models.

The geometric packing of the nanoparticle head groups of the monotethered nanosphere model cannot be captured by standard surfactant models, which treat the head-group as a flexible chain. However, there are additional entropic differences that also arise as a result of the head-group treatment. This can be seen by comparing the $D = 2.0\sigma$ TNS and h8t8 phase diagrams. We observed that the TNS model does not exhibit a cubic ordered micelle phase at low concentration, as did the surfactant model. This can most closely be attributed to the increased configurational entropy associated with the bead-spring model of the head group in surfactants. That is, the head group of the flexible surfactant has greater entropy, and a larger effective volume, as compared to the head group of the TNS with equivalent excluded volume. This can be illustrated by looking at the theoretical radius of gyration for a freely jointed chain in comparison to the radius of the TNS particle. For a freely jointed chain (21),

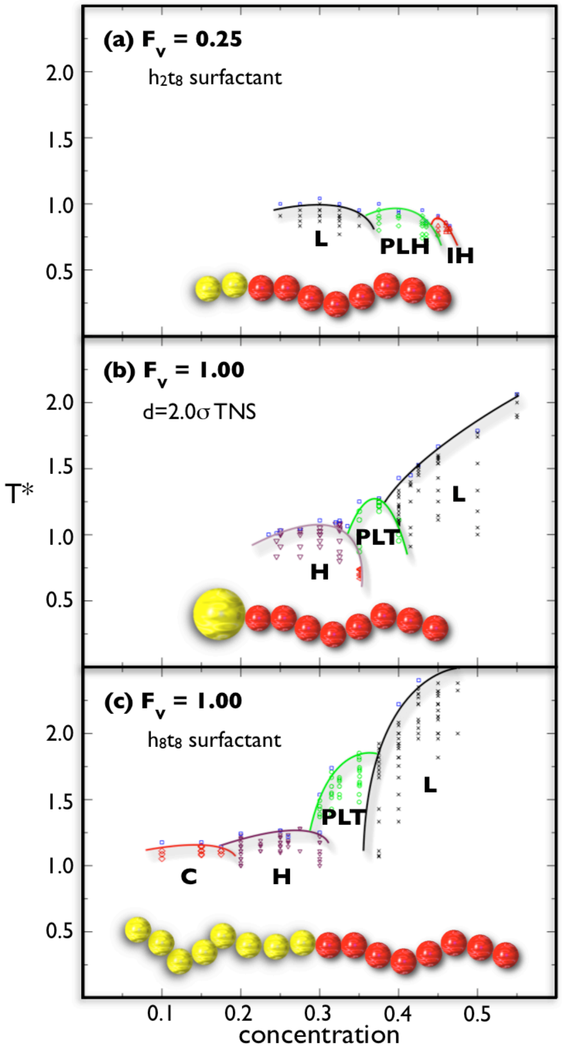

Figure 5.6 Temperature vs. volume fraction phase diagrams for surfactant and TNS systems, with the schematics of modeled systems in inset. Phases are defined as lamellae (L), perforated lamellae through the head group (PLH), hexagonally packed cylinders (H), perforated lamellae through tethers (PLT), cubic ordered spherical micelles (C), and inverted hexagonally packed cylinders (IH). **(a)** Phase diagram for h2t8 surfactant system. **(b)** Phase diagram for TNS with particle diameter of $D = 2.0\sigma$. **(c)** Phase diagram for h8t8 surfactant system. In **(a-c)**, the phase boundaries are approximate and drawn as guides for the eye. Reproduced from reference (66).

$R_g = \sqrt{N_{bonds}} L_{bond} / \sqrt{6} = 1.08$, as compared to R=1.0 for the TNS; when the values are cubed to give relative volumes the differences can become rather significant, specifically the volume ratio of (surfactant head group)/(TNS head group) is 1.26/1.00. F_v attains the value 1.26 for the surfactant when utilizing the radius of gyration in calculating the head group volume. At lower concentrations, this slightly increased volume manifests itself in the stabilization of additional phases, therefore, direct comparisons between phases of surfactants and TNS may not be applicable at low concentrations. At higher concentrations this increased volume does not manifest itself as additional phases, but rather as an increase in the order-disorder transition temperature.

5.1.3 F_v verses volume fraction phase diagram

We can additionally utilize F_v to more explicitly show the impact of nanoparticle size on the concentration dependent phase behavior. We can construct a diagram of F_v versus volume fraction, shown in Figure 5.7, that unifies the previously plotted temperature versus volume fraction phase diagrams for different nanoparticle diameters. This diagram does not include order-disorder transitions as a function of temperature, but for temperatures below the order-disorder transition temperature, it may be used as a guide to the types of structures that might form and their relationship to each other.

5.1.4 Summary

We predict that mono-tethered nanospheres form phases that strongly resemble the phases observed in surfactant systems. For certain nanoparticle diameters, concentration, and temperature, we observe the formation of cubic micelles, hexagonal cylinders, lamellar sheets, and perforated lamellar sheets. We demonstrate that for small nanoparticles relative to tether size the equilibrium structures favor sheet-like morphologies and for nanoparticles that are as large or larger than the tethers, curved morphologies are favored. We present a temperature vs. volume fraction phase diagram for a three-dimensional system of TNS and a dimensionless scaling factor Fv that relates the size of the head-group to that of the tether. F_v provides a mapping that may be useful when comparing between amphiphiles consisting of flexible chains to those containing a rigid and a flexible component. By mapping F_v vs. volume fraction it is possible to ascertain the stable morphology for either a flexible surfactant or a TNS. Finally, in contrast to the flexible surfactants, we observe an increase in the local geometric ordering of the nanoparticle as the size of the particle increases or

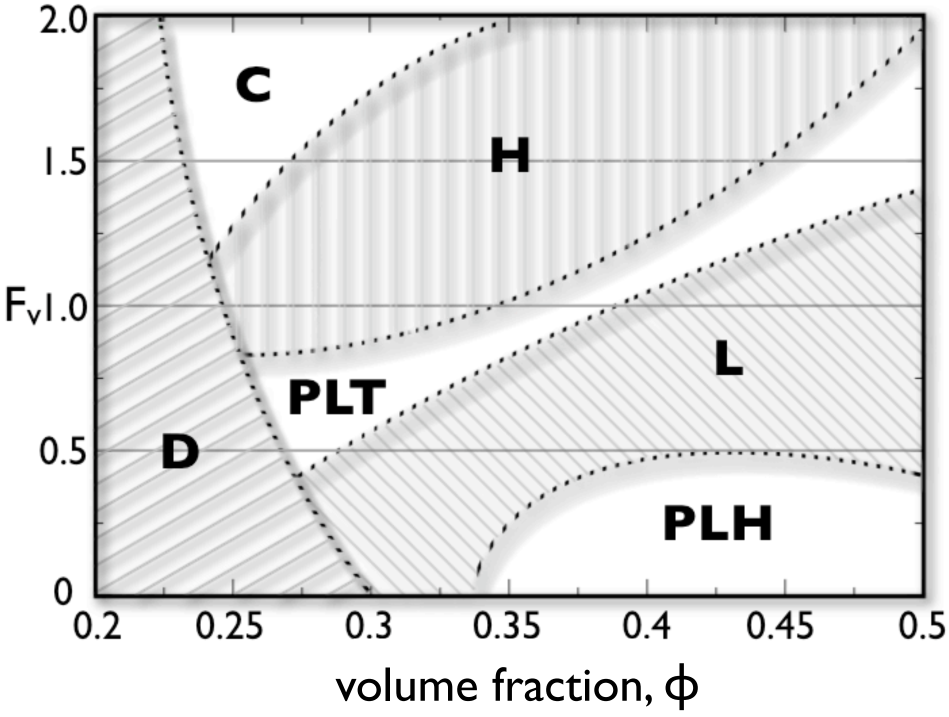

Figure 5.7 F_v vs. volume fraction "phase diagram" for T*=1.0 for TNS. Phases are defined as lamellae (L), perforated lamellae through the head group (PLH), hexagonally packed cylinders (H), perforated lamellae through tethers (PLT), cubic ordered spherical micelles (C), and disordered (D). Reproduced from reference (66).

as the concentration increases for a TNS tending toward local hexagonal packing at high concentrations.

5.2 Phase behavior of nanosphere aggregating mono-tethered nanospheres

The ability of block copolymers (BCPs) to order into periodic micro-domains makes them a choice building block for applications ranging from drug delivery (111) to photonic-bandgap materials (112). The BCP bi-continuous phases, when modified with nanoparticles (NPs), are ideal candidates for catalytic materials and high conductivity nanocomposites (113). Polymer-tethered NPs provide a novel route for the self-assembly of ordered arrays of NPs where the bulk phases formed resemble the complex morphologies found in BCPs and surfactants (73; 66). Polymer-tethered NPs constitute a class of "shape-amphiphiles" where microphase separation occurs due to the immiscibility between the NP and tether (17). In these systems, the geometry of the NP influences the bulk structure and local arrangement of NP by inducing liquid crystalline ordering (73; 17). Simulations of polymer-tethered nanorods highlight the interplay between microphase separation and particle geometry; e.g., the phase behavior for tethered rods includes a chiral cylinder phase and ordered smectic phases (73), not observed in flexible BCPs. Additional work suggests that morphologies may adopt unique structures as a result of confinement, including helical structures formed by colloids confined in v-shaped grooves (114) and helices and tori formed from BCPs confined in cylindrical pores (115).

Here, we examine the bulk-phase microstructures formed by polymer-tethered nanospheres (TNS) with attractive nanoparticles of diameter D=2.0σ (i.e. in poor solvent) connected to repulsive polymer tethers (i.e. good solvent) composed of eight beads of diameters σ; a schematic of the building block is shown in Figure 5.8. The nanospheres are modeled as being in a poor solvent and the tethers in good solvent. Thus, nanospheres aggregate and are treated using the Lennard-Jones (LJ) potential and tethers do not aggregate and are modeled using the Weeks-Chandler-Andersen (WCA) potential, as discussed earlier in section 3.1. The method of Brownian dynamics (BD) is utilized, as discussed in section 3.2. We demonstrate via simulation the first NP-based double gyroid phase. We present a new metric of local order based on spherical harmonics and use this to explore the impact of microphase-separation induced confinement on the local ordering of spherical particles. We show that this confinement promotes icosahedral packing of hard attractive particles, which helps to stabilize certain microphase-separated structures with limited stability in BCP systems, including the double gyroid.

5.2.1 The r ole of volume fraction and immiscibility

To examine the bulk phase ordering of the TNS system with attractive NP headgroups, we explore the T* vs. ϕ phase diagram. Simulations are conducted at ten fixed volume fractions between $0.15 \leq \phi \leq 0.45$. Disordered systems are incrementally cooled until bulk ordered phases are reached, as determined by visual inspection and discontinuities in potential energy as a function of T* (76). For each ϕ, multiple runs are conducted at various cooling rates and system sizes to avoid dynamically trapped structures and finite size effects. Our results presented are based on $\sim$40 independent runs of $\sim$250 state points for T* between 0.21 to 2.0, for systems of 500 to 4000 TNS, (4500 to 36000 individual beads). A phase diagram summarizing the observed phases is presented in Figure 5.8 ; each data point represents a state point arrived at using multiple cooling rates and system sizes. With increasing ϕ, we observe disordered wormy micelles (DWM), hexagonally packed

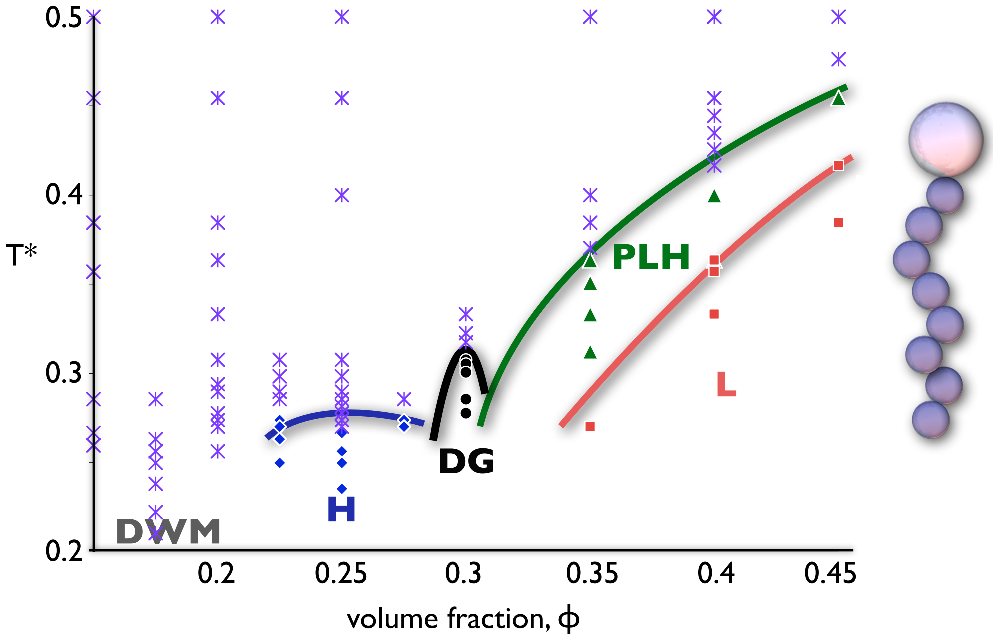

[h]

Figure 5.8 T* vs. ϕ phase behavior for D=2.0σ, where solid lines represent approximate phase boundaries determined by ∼250 state points. Stars indicate simulated disordered phases. With increasing ϕ we observe disordered wormy micelles (DWM), hexagonally packed cylinders (H), double gyroid (DG), perforated lamellae with perforations through the NPs (PLH), and lamellar bilayers (L). A schematic of the model tethered nanosphere is shown at right. Adapted from reference (67).

cylindrical micelles (H), the bi-continuous double gyroid (DG), perforated lamellae with perforations through the NP layer (PLH), and lamellar bilayers (L). At T* > T*$_{ODT}$, we find disordered aggregates and at sufficiently high T* we find no aggregates.

Interestingly, we observe both DG and PLH phases between ϕ ∼0.30 - 0.45. A snapshot of the DG phase is shown in Figure 5.9a and a snapshot of the PLH phase is shown in Figure 5.9b. In BCP systems, both the DG and PLH phases have been reported in similar regions of the phase diagram (107); however, the DG phase is considered to be an equilibrium morphology (116) and the PLH phase is considered to be metastable, stabilized by compositional fluctuations (117). Few examples of the DG phase exist for the simulation of BCPs and surfactants using non-lattice, dynamics based methods (118; 119) making this result unusual. For the TNS system, the dominance of the PLH phase outside of the DG region suggests that over this ϕ range it is stable and reproducible; we did not observe bi-continuous structures within the PLH region. As in the case of the polymer-tethered rods, the perforations result from competition between the NPs tending to locally order and the

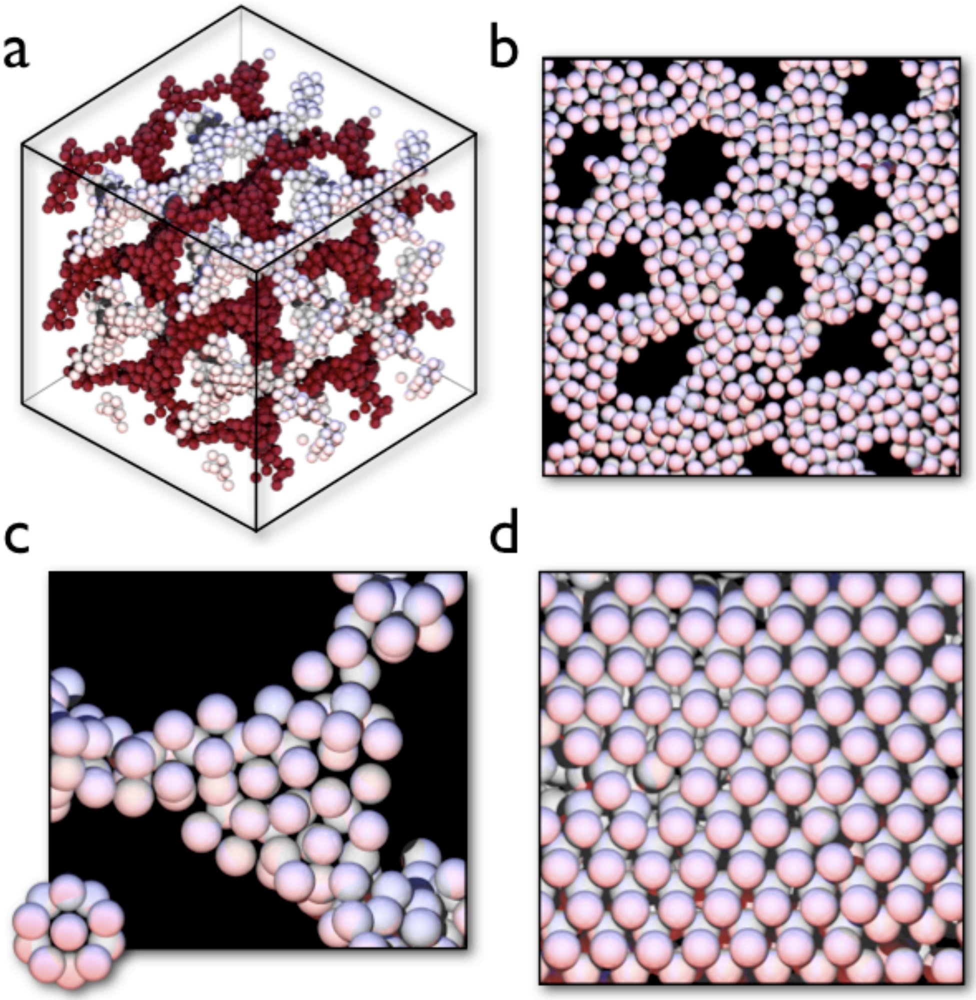

Figure 5.9 Images of self-assembled structures with tethers removed for clarity. **(a)** DG phase; the minimal unit cell was duplicated and found to be stable over $\sim$10 million time steps. **(b)** Individual sheet of PLH. **(c)** Node of the DG, showing icosahedral rings; perfect icosahedron inset. **(d)** Crystalline packing of L. Reproduced from reference (67).

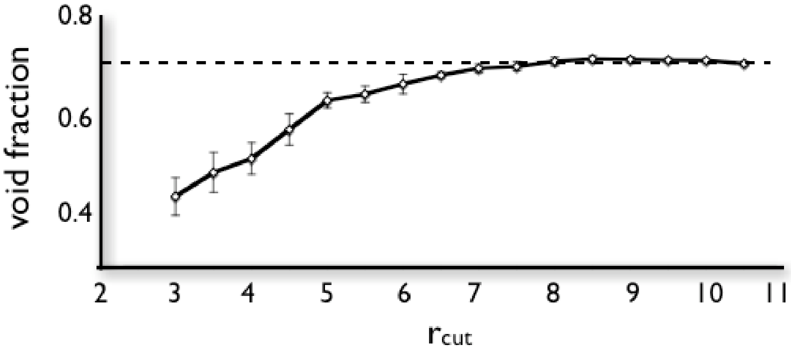

Figure 5.10 Void fraction of a node vs. r_{cut}. For small rcut values, void fraction is lower than the bulk, approaching the bulk value of 0.7 (dotted in the figure) as r_{cut} is increased. Reproduced from reference (67).

tether tending to maximize its configurational entropy (73).

The limited stability of the DG phase in BCP systems has been attributed to packing frustration within the connection points (nodes) (120; 121), which arises due to a high void fraction (low packing density) within the nodes. To examine this, we look at relative trends in void fraction. We approximate the center of a node and calculate the void fraction within a spherical volume drawn from the center, repeating for various sphere radii, r_{cut}. We find that for small values of r_{cut} the void fraction is lower than in the bulk, starting at $\sim$0.44, and as r_{cut} is increased we approach the bulk void fraction of 0.7 as shown in Figure 5.10. Thus particles within the nodes pack more densely than in the bulk. Ref. (122) used a similar analysis to compare a monodisperse BCP system to a blend of two different length BCPs. In the blend, the authors found that the longer of the two polymers occupied the nodes of the DG, resulting in a larger range of stability compared to the monodisperse system (122). For the monodisperse system, the authors found that the void fraction is higher than the bulk for small values of r_{cut}, and decays to the bulk value as r_{cut} becomes large (122). In the blend, the authors found that, like our system, the void fraction is *lower* than the bulk for small values of r_{cut} and approaches the bulk value from *below* as r_{cut} becomes large (122). This similarity in trends suggests that the ability of the TNS system to realize the DG phase is linked to the ability of NPs to locally order into dense structures, decreasing the packing frustration. In section 6 we discuss the stability of the double gyroid phase in more detail and compare with the double gyroid formed by tethered nanorods.

5.2.2 Local structure of nanospheres

We observe visually that the nanoparticles tend to form ring-like structures resembling icosahedral clusters in the H, DG, and PLH phases. Unlike icosahedral ordering observed in dense liquids, the tether sterically restricts particle packing, resulting in clusters with only partial coordination. To verify our visual findings, we utilize the R_{ylm} method detailed in section 4.1. We incorporated into the R_{ylm} reference database icosahedral clusters that maintain the same bond angles, but possess only partial coordination numbers (e.g. we remove 1 to 4 particle(s) from a perfect 13-particle icosahedral cluster). These clusters are indistinguishable from the minimum potential energy clusters found by Doye and Wales (123). Our reference library additionally contains other polyhedra and crystalline arrangements with full and partial coordination.

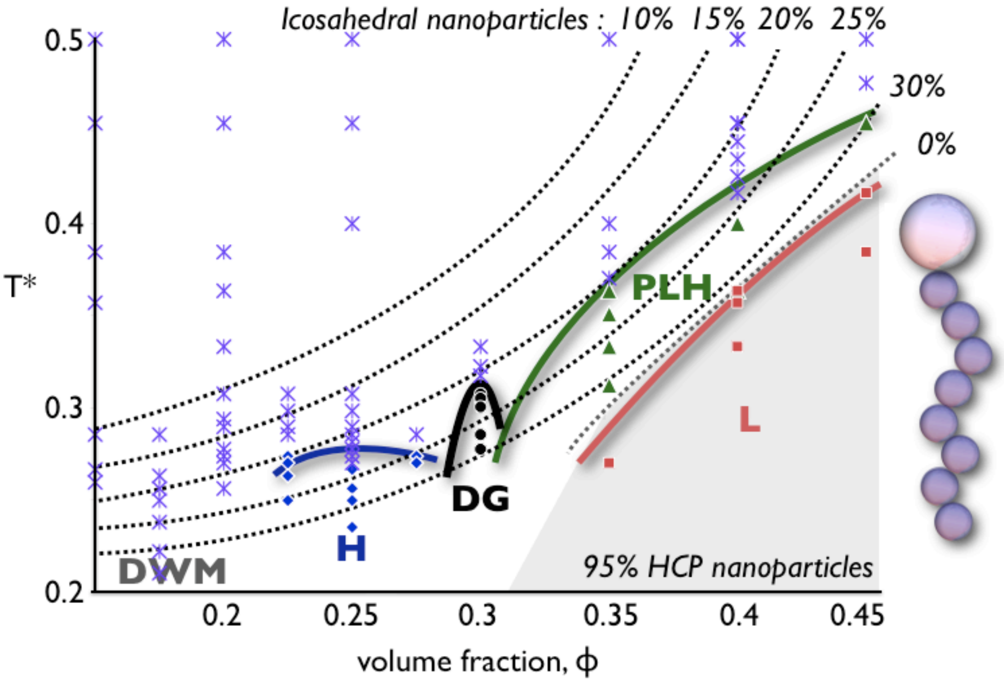

Figure 5.11 T* vs. ϕ phase behavior, as previously shown in Figure 5.8. Dotted lines fit data points indicating values of T* and ϕ at which the indicated percentages of icosahedral clusters formed by NP headgroups are found. The shaded region indicates the range of T* and ϕ over which crystalline ordering of the NPs is observed. A schematic of the model tethered nanosphere is shown at right. Reproduced from reference (67).

Applying the R_{YLM} algorithm to the DG phase, we confirm that the local arrangements of NPs are icosahedral with partial coordination as observed in Figure 5.9c. Applying this analysis to the entire T* vs. ϕ phase diagram, we observe that as T* is decreased, there is an increase in the number of icosahedrally ordered NPs with partial coordination corresponding to increased aggregation of NPs. Figure 5.11 shows the general trend of icosahedral ordering overlaid on the bulk phases; dotted lines indicate the set of values of T* and ϕ at which 10, 15, 20, 25, and 30% of the NPs are central particles in icosahedral clusters. Each line is interpolated from the analysis of the available data points (points at 6 to 16 different T* for each ϕ), where each point is averaged over $\sim$10 samples or $\sim$10000 NPs. While we see a strong increase in icosahedral ordering, we see little increase in crystalline ordering until we reach the T^*_{ODT} of the L phase, at which point NPs crystallize and the number of icosahedrally-ordered NPs drops to nearly 0% (shaded area in Figure 5.11). There we find bilayers that possess distinct hexagonal closed packed ordering of NPs as shown in Figure 5.9d, as compared to the liquid-like layers found in the PLH phase shown in Figure 5.9b.

Role of confinement

It is known that small clusters of LJ particles will favor icosahedral packing; however as the system size approaches bulk behavior, such ordering is lost in favor of close-packed crystals since icosahedra cannot tile Euclidean 3D space. The presence of icosahedral clusters in our systems is therefore surprising, since the domains contain many particles. The bulk phases that exhibit strong icosahedral ordering of NPs, namely the H, DG, and PLH phases, have in common that the NP-rich domains are shaped like cylindrical tubes; the H and DG phases are clearly tubular and the PLH phase contains interconnected tubes arranged into sheets. We observe that there is little penetration of NPs into the polymer-rich domain, thus the boundary between these domains can be thought of as a confining surface. It appears that confining NPs into tubular domains, as a result of microphase separation, allows for the formation of icosahedral clusters. To test this, we confine LJ particles of diameter 2σ within cylindrical pores of various diameters with ϕ = 0.25 and T*=0.2. The interaction between the particles and the walls of the pore are modeled by the WCA potential. Examination of the dimensionless pore diameter, d*= pore diameter/confined particle size, shows a strong presence of icosahedral particles with both full and partial coordination at $d^* < 5$, and an associated decrease in crystalline particles (Figure 5.12). This model cylindrical pore system relates well to the tubular H and DG phases where $d^* \sim 4.5$-5.

5.2.3 Summary

Our results demonstrate the important role played by the local packing of NPs within microphase-separated domains on the stability of the bulk structure for a tethered NP system. We observe a particularly interesting interplay between the local packing of NPs and domain

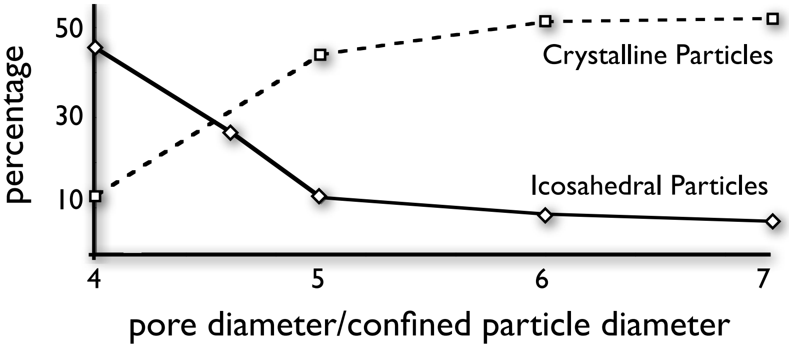

Figure 5.12 Percentage of icosahedral and crystalline NPs under cylindrical confinement vs. d*. Icosahedral ordering is favored for diameters less than 5, which corresponds to the diameter of the tubes formed in the DG and H phases. Reproduced from reference (67).

shape. More specifically, we find that cylindrical confinement, whether from hard walls or as a result of microphase separation, can be used to promote icosahedral ordering between attractive spheres.

Chapter 6

Role of nanoparticle geometry on the stability of the double gyroid structure

In chapter 5 we explored the phase behavior of mono-tethered nanospheres in both good and poor solvent. When the solvent was poor for the nanospheres, we found a variety of phases, but most notably the double gyroid structure. In this chapter, we explore the formation of the double gyroid structure for mono-tethered nanospheres in detail. We compare and contrast with the double gyroid structure formed by end-tethered nanorods, exploring the connection between local and global ordering. We demonstrate the ability of these nanoparticles to adopt distinct, minimal energy local packings, in which nanospheres form icosahedral-like clusters and nanorods form splayed hexagonal bundles. These local structures reduce packing frustration within the nodes of the double gyroid. We argue that the ability to locally order into stable structures is key to the formation of the double gyroid phase in these systems. The work presented in this chapter is published in reference (68).

6.1 Introduction

Block copolymers and surfactants have long been known to self-assemble into a wide variety of complex structures where the assembly is driven by immiscibility between chemically distinct blocks in the polymers (24) and between distinct head and tail groups in surfactants (23). These ordered structures are highly sought for applications at the nanoscale, ranging from photonic-bandgap materials (112) to templates for nanoparticle assembly (124) and hydrogen storage. Hybrid building blocks have recently been created that resemble block copolymers where the individual blocks consist of nanoparticles and polymers (125; 56; 61; 64; 63). These hybrid building blocks, or tethered nanoparticles, constitute a class of “shape amphiphiles” (126; 17) where microphase separation occurs due to the immiscibility between the nanoparticle and polymeric tether resulting in mesostructured equilibrium phases that resemble the morphologies of block copolymers and surfactants (73; 66).

In previous work, we examined the interplay between microphase separation and nanoparticle geometry for tethered nanospheres (TNS) (67; 66) and tethered nanorods (TNR) (73; 74), finding unique changes to phase behavior as compared to flexible surfactants and block copolymers. For example, the phase behavior of the nanosphere-aggregating TNS system includes hexagonally packed cylinders, the double gyroid morphology, and perforated lamellar phases where there is a predominance towards icosahedral ordering of nanospheres (67) and a lamellar phase with HCP ordering of nanospheres (67). The tether-aggregating TNS system does not form the double gyroid structure, as would be expected for surfactants, instead forming perforated lamella (66). The phase behavior of the nanorod-aggregating TNR system includes a hexagonally packed cylinder phase where the nanorods twist along the length of the cylinder, hexagonally and tetragonally perforated lamellar phases where the nanorods form a smectic structure, and a lamellar phase with smectic C-like ordering of the nanorods (73). A transition from hexagonally packed cylinders to the double gyroid morphology is seen upon reducing the length of the tether in the TNR system (74), similar to what was observered for rod-coil liquid crystals (127).

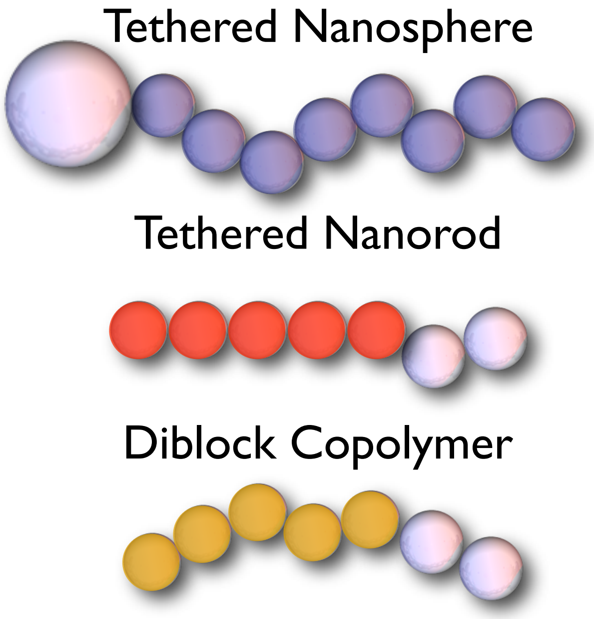

Figure 6.1 Model building blocks utilized. For more details see section 3.1. Reproduced from reference (68).

In this work, we examine and compare the double gyroid (DG) microstructure formed by the TNS and TNR building blocks with attractive nanoparticles and repulsive tethers in order to learn about the stability of the DG structure. The DG is a bicontinous structure where the nanoparticles form two distinct, interpenetrating networks. The DG structure is of particular interest as it is seen as a candidate for catalytic materials, high conductivity nanocomposites (113), and photonics applications (112). In this context we study three systems. We examine a system mono-tethered nanospheres, where nanospheres of diameter D=2.0σ are in poor solvent (i.e. nanospheres aggregate and are treated with the Lennard-Jones (LJ) potential), attached to non-aggregating polymer chains composed of eight beads of diameter σ. Polymer chains are modeled as being in good solvent (i.e. tethers do not aggregate and interact via the Weeks-Chandler-Andersen (WCA) potential). We also explore a system of end-tethered nanorods, where nanorods are modeled as a collection of five rigidly connected beads of diameter σ in poor solvent (i.e. they interact via the LJ potential) connected to polymer chains composed of two beads of diameter σ. Polymer chains are modeled as being in good solvent (i.e. they interact via the WCA potential). For additional comparison, we look at a flexible diblock copolymer (BCP) equivalent of the tethered nanorods, where the rigid constraint of the nanorod is removed and particle connectivity is instead treated using the FENE potential. The building block models follow those described in section 3.1. The method of Brownian dynamics is used to simulate these systems, as described in section 3.2.

6.2 Flory-huggins interaction parameter

Although the models for the TNS, TNR and BCP are very similar, key parameters such as T* do not necessarily correspond to the same statepoint. For example, in Reference (73) the rigidity of the tethered nanorod induced phase separation at a higher T* than the equivalent coil-coil BCP. Additionally, it is well known that the order-disorder temperature in BCP systems will scale as the number of beads (128), so we expect that a tethered nanorod system with a 5-bead rod would order at a much higher T* than a tethered nanosphere system where the nanoparticle is only a single bead, if the beads interactions were similar. In order to compare between the TNS, TNR, and BCP systems we determine the relationship between Flory-Huggins interaction parameter, χ, and T* for each of the systems. The Flory-Huggins interaction parameter allows us to make comparisons between systems regardless of the specific model details used. For example, χ has been used to compare the calculated phase boundaries of BCPs for Brownian dynamics systems that utilize attractive LJ interactions, dissipative particle dynamics systems that utilize only repulsive interactions, and mean field theory calculations (72). To determine χ, we follow a similar procedure to that outlined in

References (128) and (72). For a two-component mixture the free energy can be expressed as:

$$\frac{F}{k_bT} = \frac{f_A}{v_AN_A}lnf_A + \frac{1-f_A}{v_BN_B}ln(1-f_A) + \frac{\chi f_A(1-f_A)}{(v_Av_B)^{1/2}} \tag{6.1}$$

where f_A and $(1-f_A)$ are the fraction of constituents A and B, respectively, v_A and v_B are the volume of the beads of constituents A and B, respectively, and N_A and N_B are the number of beads of constituents A and B, respectively (21). This expression assumes incompressibility where $f_B = (1-f_A)$; note f_A should not be confused with the bulk volume fraction ϕ. If we consider the system to be in equilibrium, the free energy will be at a minimum and thus $\frac{dF}{df_A} = 0$. By taking the derivative of the free energy in Equation 6.1 with respect to f_A and setting the resulting expression equal to zero, we arrive at the following equation that relates χ to f_A:

$$\chi = -\frac{(v_Av_B)^{1/2}(-ln(f_A)v_BN_B - v_BN_B + ln(1-f_A)v_AN_A + v_AN_A)}{v_AN_Av_BN_B(2f_A-1)} \tag{6.2}$$

6.2.1 General procedure for determining χ

To determine how χ scales with T* for each system, we calculate the relative solubility of species A mixing into species B as a function of T* and solve for χ from Equation 6.2. For example, in the case of the tethered nanosphere system, we specify that the nanosphere is species A and the 8 bead polymer chain is species B, and utilize the following general procedure. Note that the immiscible components (here, nanospheres and tethers) are not bonded to each other for the determination of χ.

Utilizing a long rectangular box with aspect ratio 1:1:4 (x:y:z), we place all the nanospheres on one half of the box and all polymers on the other half, creating an interface between the two immiscible species. For a specific T*, we run the system for approximately 10 million timesteps monitoring the potential energy to ensure we reach equilibrium. After these 10 million equilibration timesteps we generate an average concentration profile along the long dimension of the box by collecting data over the next 10 million time steps. To solve for χ, we calculate the average fraction of nanoparticles that have mixed into the polymer region (i.e. f_A) from the concentration profile, then plug this value into Equation 6.2, solving for χ. We then repeat for various values of T* creating a relationship between T* and χ, as shown in Figure 6.2. Typically, for incompressible mixtures, as T* is decreased χ will increase and this relationship is often described as $\chi = \frac{R}{T^*} + Z$ (21), where R and Z are system dependent fitting parameters; consequently, we fit our data using linear regression to determine the relationship. Since our systems are compressible the χ mapping depends on the bulk volume fraction, ϕ. Specifically, the slope of the fitting will increase as ϕ is increased, i.e. there will be less desire for the two systems to mix.

6.2.2 χ mappings for TNS, TNR, and BCP

Utilizing the same procedure for each of the building blocks, we find the following relationships for χ vs. T* (also shown in Figure 6.2). These mappings were performed at $\phi_{TNS} = 0.3$ and $\phi_{TNR} = 0.21$, corresponding to the bulk volume fractions where the DG was simulated for each of the systems, respectively; the mapping for the BCPs was performed at $\phi_{BCP} = 0.21$ for appropriate comparison with the TNR system.

$$\chi_{TNS} = (0.93 \pm 0.06)/T^* - (0.12 \pm 0.05) \tag{6.3}$$

$$\chi_{TNR} = (6.89 \pm 0.53)/T^* - (1.28 \pm 0.24) \tag{6.4}$$

$$\chi_{BCP} = (6.89 \pm 0.15)/T^* - (1.70 \pm 0.09) \tag{6.5}$$

These relationships follow the expected trends. For an equivalent χ value, T* is higher for the TNR system than the BCP system; this corresponds to the behavior seen in reference (73) where the TNR system microphase separated at a higher T* than the equivalent BCP system. For an equivalent χ value, T* is substantially higher for the TNR system as compared to the TNS system; previous simulations of TNRs found the system microphase separates at approximately T*=1 (73) whereas the TNS system was found to order at about T*=0.3 (67). We should be aware that these results are for moderate bulk volume fractions ($\phi = 0.3$ for TNS and $\phi = 0.21$ for TNR and BCP); the results in References (128) and (72) show good agreement with theory using this procedure, however the comparisons were made at higher values of ϕ corresponding to melt conditions ($\phi = 0.45$). The difference in ϕ will manifest itself in the compressibility assumption, specifically $f_B = (1 - f_A)$ may not be completely valid at the lower ϕ values we utilize. However, since our simulations are for building blocks in selective solvent (i.e. tether beads are treated with the repulsive WCA potential), the tethers can fill the available space without forming low density holes and thus the χ mapping should allow for reasonable comparisons among these systems at the lower values of ϕ .

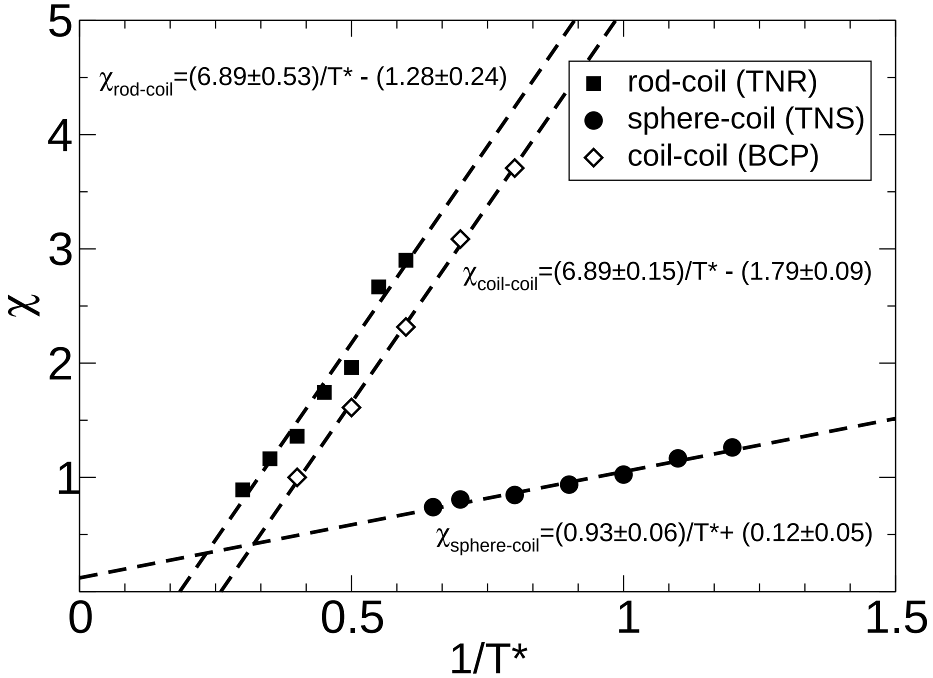

Figure 6.2 χ mappings for TNS (circles), TNR (squares), and BCP (diamonds). Reproduced from reference (68).

6.3 The double gyroid structure in tethered nanospheres and tethered nanorod systems

In previous publications we reported the presence of the double gyroid (DG) structure in both the TNS (67) and TNR (74) systems. The double gyroid is a bicontinous structure where the minority component, in our case the nanoparticles, forms two distinct, interpenetrating networks that never connect. The minority component organizes into a series of cylindrical tubes (arms) where three tubes connect at each node. Figure 6.3 shows a simulation snapshot of the DG formed by the TNS system **(a)** and the TNR system **(b)**. For clarity we have removed the tethers and show only the minority component (nanospheres or nanorods) where the two distinct networks are colored red and white; the particles in the red domain are chemically identically to those in the white domain. These structures were identified both visually and by calculating the structure factor. The structure factor for the DG shows two strong peaks with a characteristic ratio of $\sqrt{3}$:$\sqrt{4}$ as expected (116). Averaging over several runs, the DG was found to form for $\phi = 0.3$ at 1/T* $\geq$ 3.28 for the TNS system and for $\phi = 0.21$ at 1/T* ≥ 0.825 for the TNR system. Recent theoretical predictions of the order-disorder transition for TNS agree with our simulations, reporting a value of 1/T* ~ 3 for $\phi = 0.3$ (69). Using the χ mappings we calculated in section 6.2.2, we find reasonable agreement between the average order-disorder transitions for both systems as expected. Specifically, we find that $\chi^{TNS}_{order-disorder} = 3.17 \pm 0.25$ and $\chi^{TNR}_{order-disorder} = 4.40 \pm 0.70$, where the reported error for χ is calculated from the maximum error in the linear regression of χ vs. T*.

6.3.1 Packing frustration analysis

The formation of the DG in the tethered nanoparticle systems is surprising since it is known to exist only in a small region of the phase diagram for BCPs (25; 118; 119; 129), rod-coil BCPs (127; 130), and surfactants (23), and was not seen in some of our previous simulations of the TNS (66) and TNR (73) systems. The limited range of stability of the DG phase in BCP systems has been attributed to packing frustration at the nodes of the gyroid (120; 121). It has been shown that the standard deviation in mean curvature, σ_H, correlates to packing frustration and dictates the overall stability of a structure (120). For example, Matsen and Bates (120) calculated σ_H for various structures finding $\sigma_H = 0.121$ for the gyroid as compared to $\sigma_H = 0.003$ for cylinders and attributed this difference to the inability of the gyroid structure to simultaneously minimize surface area and minimize packing frustration (120). The magnitude of σ_H is important in determining which phase will form as the system should selectively prefer to form a structure with less packing frustration (120); this is why BCPs typically form the DG over, for instance, the bicontinuous double diamond structure where σ_H = 0.311 (120). In BCPs, packing frustration has been shown to manifest itself as a high void fraction (low packing density) within the nodes of the gyroid (122) where the polymer needs to stretch to fill the volume dictated by the interface (120). Martinez-Veracoechea and Escobedo have shown that packing frustration in the nodes of BCPs can be reduced by adding monomer and homopolymer to the system, increasing the stability of phases like the DG (122) and stabilizing other structures such as double diamond (26).

To assess the stability of the DG structure for the TNS and TNR systems, we examine packing frustration by calculating the relative trends in void fraction at the nodes and comparing this with the void fraction of the arms, since measuring σ_H is problematic in a system of discrete particles. To look at this trend we approximate the center of a node and calculate the void fraction within a spherical volume drawn from the center, repeating for various sphere radii, r_{cut}. If we consider a very large value of r_{cut}, we capture the bulk void fraction

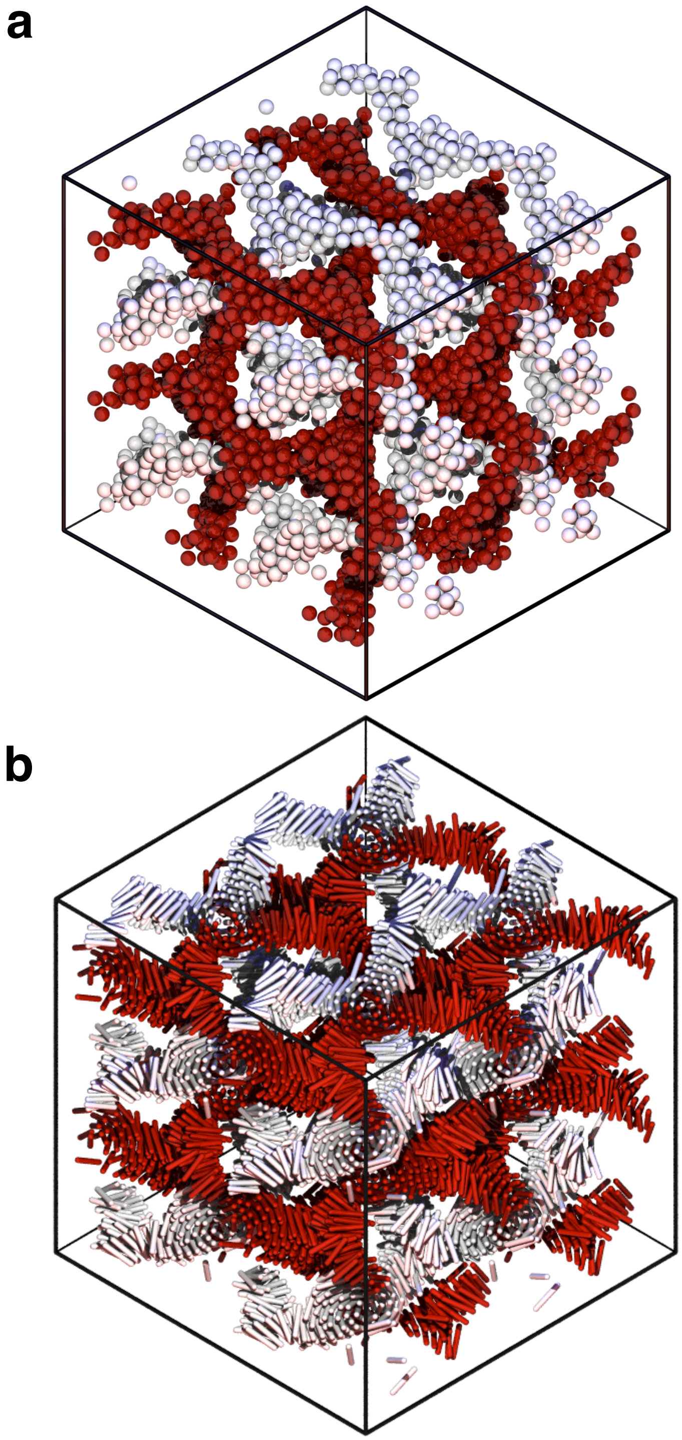

Figure 6.3 **(a)** DG phase formed by the TNS system, **(b)** DG phase formed by the TNR system. In both cases tethers have been removed for clarity. The images correspond to the minimal unit cell duplicated once in each direction for clarity. Reproduced from reference (68).

of the system and as r$_{cut}$ is decreased, we get an increasingly localized picture of what occurs at the nodes. We perform the same procedure on the arms, again, capturing a relative trend in void fraction. For both the TNS and TNR systems, the void fraction of the arms and nodes are nearly identical, as shown in Figure 6.4, suggesting there is a uniform density throughout the DG in both structures, irrespective of whether we are at the node. Hence, we do not have a characteristic high void fraction within the nodes, as has been shown for BCPs (122), thus the nanospheres and nanorods have reduced the packing frustration as compared to a flexible BCP. Additionally, we can compare the void fraction between the nodes and the bulk system. For both the TNS and TNR systems, we find that for large values of r$_{cut}$ the void fraction is approximately that of the bulk system and as r$_{cut}$ is decreased, the void fraction is also decreased, as shown in Figure 6.4. Specifically, for the TNS system, the void fraction for large values of r$_{cut}$ is ∼0.7 and for small values ∼0.5. For the TNR system, the void fraction for large values of r$_{cut}$ is ∼0.79 and for small values ∼0.55. Thus particles within the nodes pack more densely than the bulk system as a whole. Martinez-Veracoechea and Escobedo used a similar analysis to compare a monodisperse BCP system to a blend of two different length BCPs (122). In the blend, the authors found that the longer of the two polymers occupied the nodes of the DG, resulting in a larger range of stability compared to the monodisperse system (122). For the monodisperse system, the authors found that the void fraction is *higher* than the bulk for small values of r$_{cut}$ and for the blend the authors found that, like our systems, the void fraction is *lower* than the bulk for small values of r$_{cut}$ (122). This similarity in trends suggests that the DG structures formed by the TNS and TNR systems may be more stable than an equivalent flexible BCP system. We conclude that by not forming low density regions at the nodes of the DG both the TNS and TNR systems have reduced their packing frustration, and we hypothesize that this reduction is a direct result of the geometry of the minority component and its ability to pack locally into compact, low energy structures. We test this hypothesis in sections 6.4.1 and 6.4.2.

We can further assess the importance of the particle geometry on stability by specifically comparing to a BCP system. If we replace the rigid constraints in the TNR system with FENE springs, we arrive at a simple model for a flexible coil-coil BCP, as was previously described in section 3.1. If the rigidity of the nanorod does not influence the stability and packing frustration of the DG phase, we would expect to find the DG in the BCP system at $\chi \geq 4.40 \pm 0.70$ and $\phi = 0.21$. Starting from the ordered DG configuration, we run the system as a coil-coil BCP for various values of χ. We find that the DG structure is not stable for values of $\chi <\sim 8$; instead, the DG falls apart and forms a disordered aggregate. An example of the disordered structure is shown in Figure 6.5. For values of $\chi >\sim 8$, the DG structure persists, however, it is most likely a kinetically arrested structure and not at

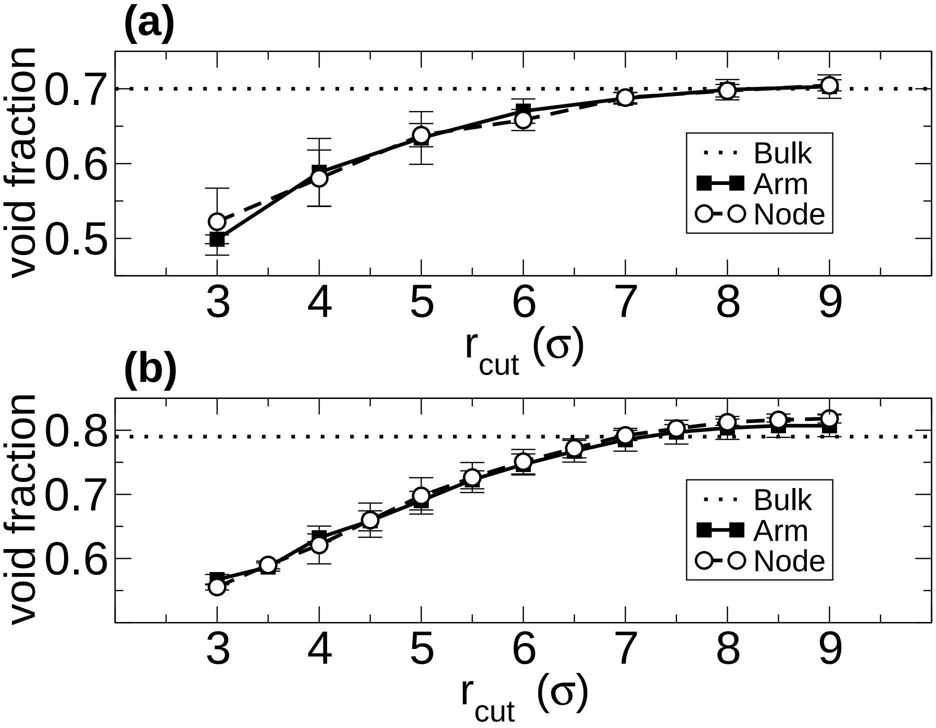

Figure 6.4 Relative void fraction within the nodes of the **(a)** TNS DG for $1/T^*$ =3.3 (χ = 3.19 ± 0.25) and **(b)** TNR DG for $1/T^*$ =0.9 (χ = 4.92 ± 0.72). Reproduced from reference (68).

equilibrium due to the large value of χ. Starting from an athermal, disordered configuration, we incrementally cool the system, finding only disordered structures, even for values of $\chi >\sim 8$. This supports the contention that the DG is not stable for the BCP system under these conditions. Note that simulations were also performed with various unit cell sizes to avoid any box size issues that are associated with 3d periodic microstructures, again, yielding only disordered structures. Thus, we find that for equivalent statepoints, we were unable to realize the DG phase when the rigid constraint was removed, which suggests that the stabilization of the DG is strongly influenced and controlled by the geometry of the aggregating species.

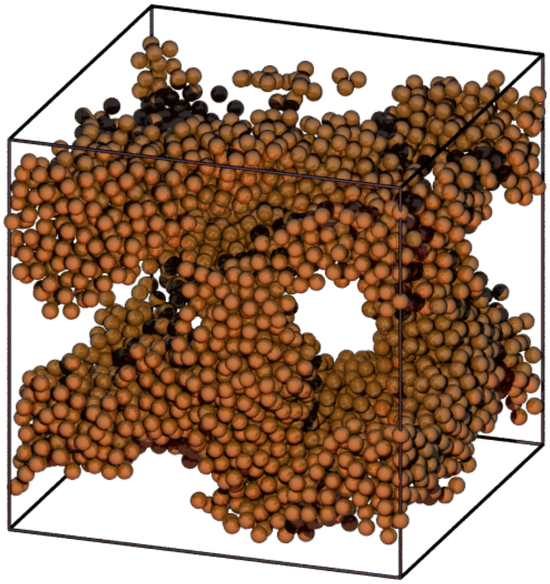

Figure 6.5 Disordered structure formed by BCP system for $\chi = 8.6 \pm 0.26$. The tethers have been removed for clarity, and only the minority, aggregating species is present. Reproduced from reference (68).

6.4 Local structure of nanoparticles

6.4.1 Local structure of the TNS gyroid

The ability of the TNS system to reduce the packing frustration in the DG can be understood by looking at the local packing of the particles at the node. Figure 6.6 shows a simulation snapshot of the TNS DG node. We see distinct local ordering in the node, specifically ring-like structures that resemble icosahedral clusters. An icosahedron is constructed of a central particle surrounded by 12 nearest neighbors and is a minimal potential energy structure for 13 Lennard-Jones particles. This ordering is not limited to the nodes and occurs throughout the entire DG structure.

We utilize the R_{ylm} method, as discussed in section 4.1, to determine the local packing of the nanospheres. Our reference library includes standard particle arrangements such as the Kasper polyhedra (Z10, Z11, Z12, Z13, Z14, Z15) (131), face centered cubic (FCC), hexagonally close packed (HCP), body centered cubic (BCC), and simple cubic (SC). Additionally, our library includes partial icosahedral clusters, where 1-4 particles are removed from the ideal Z12 Icosahedron (see Figure 6.7), and partial clusters of FCC and HCP where 1-5 particles are removed from the ideal clusters.

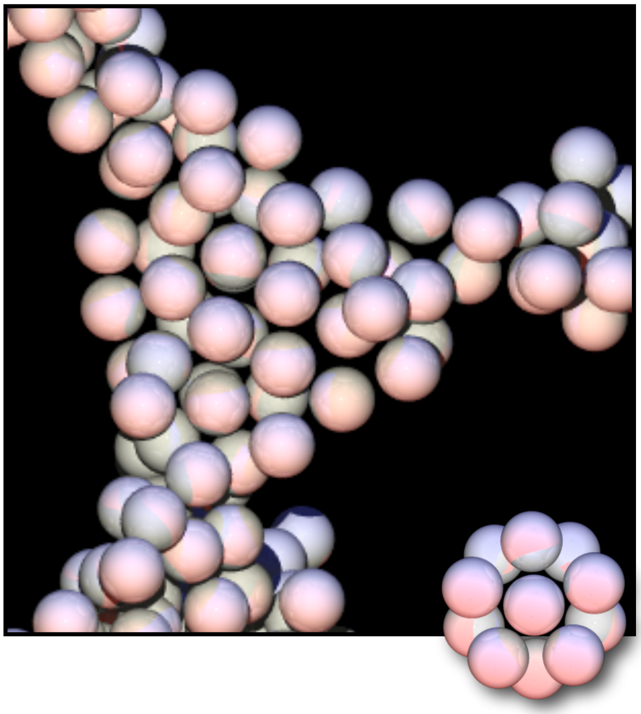

Figure 6.6 Node of the DG formed by the TNS system, with a perfect icosahedron showed in inset. Tethers have been removed for clarity. Reproduced from reference (68).

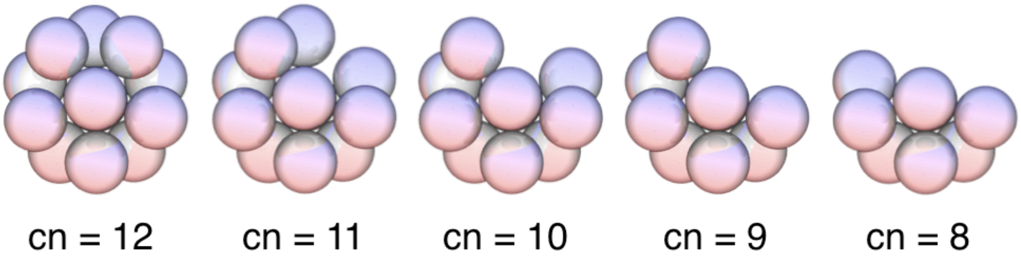

Figure 6.7 Icosahedral clusters ranging from full coordination number (cn) of 12 to partial coordination of 8. Reproduced from reference (68).

Using the R$_{ylm}$ method, we determined in reference (67) the packing of the nanoparticles in the DG to be predominantly icosahedral clusters with partial coordination, i.e. we found clusters that retain the same bond angles as a perfect icosahedron but with 1-4 particles removed (see Figure 6.7) (67); these clusters are identical to the minimal potential energy clusters found by Doye and Wales (123). Partial clusters are formed as a result of the steric effects of the tethers and the microphase separation that occurs. Table 6.1 shows the percentage of nanospheres that are "central" particles within partial icosahedral clusters, the percentage of nanospheres that are "central" particles within partial crystalline cluster (HCP and FCC in this case) along with the average coordination number, cn, of nanoparticles for an example cooling sequence. The double line in Table 6.1 signifies the transition from a disordered state to the ordered DG microphase. As we increase 1/T* (i.e. cool the system), we notice a substantial increase in the number of icosahedral-like clusters, increasing from approximately 17.5% to 30% but very little change in crystalline arrangements, with an average value approximately 16% within the ordered regime (1/T* $>$ 3.25). We also see a minor increase in average coordination number, increasing from approximately 7 to 8; this does not change as rapidly as the percentage of icosahedral clusters since coordination number does not differentiate between ordered and disordered local configurations.

Table 6.1 Local Structure of Nanospheres. Reproduced from reference (68).

$1/T^*$	$\chi \pm$ error	% Icos. ± stdev	% Crystal ± stdev	cn ± stdev
3.00	2.91 ± 0.23	17.3 ± 1.97	17.1 ± 1.76	6.9 ± 2.3
3.15	3.05 ± 0.24	18.5 ± 2.91	18.1 ± 2.53	7.2 ± 2.1
3.25	3.14 ± 0.25	21.7 ± 2.67	18.7 ± 2.66	7.4 ± 2.0
3.30	3.19 ± 0.25	23.9 ± 1.81	16.9 ± 1.91	7.4 ± 2.1
3.50	3.38 ± 0.26	26.4 ± 2.80	16.2 ± 3.13	7.5 ± 2.0
3.60	3.47 ± 0.27	28.7 ± 2.01	15.7 ± 2.49	7.6 ± 2.0
3.70	3.56 ± 0.27	28.6 ± 3.12	15.8 ± 2.34	7.6 ± 2.1
3.80	3.66 ± 0.28	30.1 ± 2.61	15.5 ± 1.62	7.8 ± 2.0

In Figure 6.8 we also present these results grouped by the coordination of the partial icosahedral cluster, i.e. we plot the data for each cluster arrangement separately. As the coordination number suggests, at all T* we are most likely to find clusters with a coordination number of 8 and likewise, we find only a very small number of particles with a coordination number of 11. The summation of all of the icosahedral clusters, as reported in Table 6.1, is shown as solid diamonds in Figure 6.8 demonstrating a clear linear increase over the range considered.

Similarly, we can group the results for crystalline partial clusters by their coordination number. This eliminates some complexity, since for HCP and FCC there are 12 unique partial clusters for coordination numbers ranging from 7-11; this is due to the fact that the partial cluster we form depends on which particle(s) we choose to remove. For example, we have two unique spherical harmonic fingerprints for an HCP cluster with coordination number of 10 depending on which particles we remove. Additionally, because of the similarities between HCP and FCC, certain partial clusters are identical and we cannot determine whether the cluster is FCC or HCP, only that it possesses characteristics of both. As such, we group together the partial clusters of both FCC and HCP by coordination number of the partial cluster, as shown in Figure 6.9. We find that for all configurations, the percentage of crystalline clusters does not change much as we increase $1/T^*$ (i.e. cool the system); there

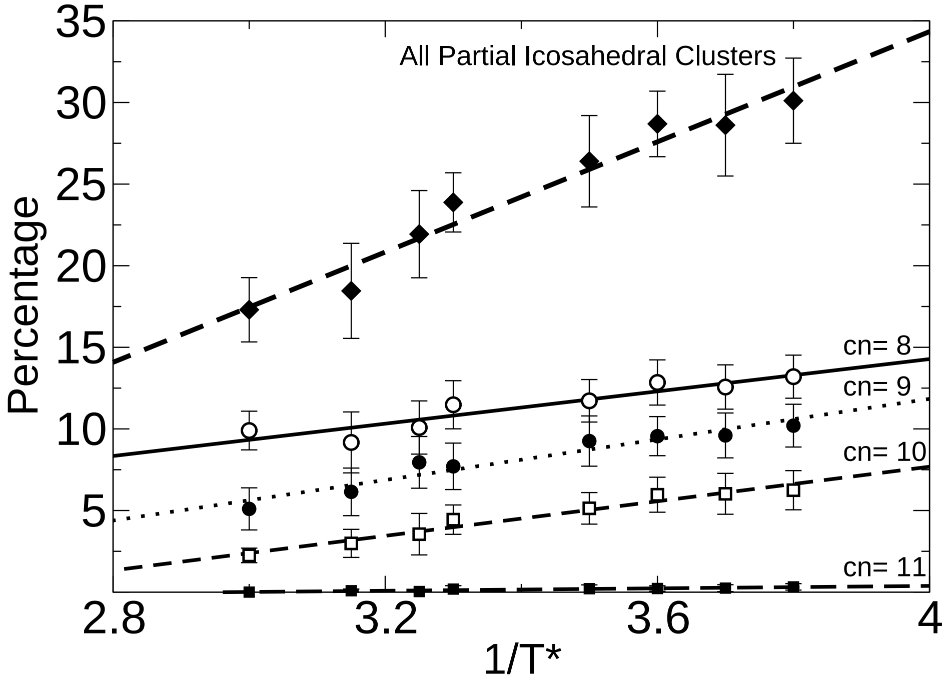

Figure 6.8 Icosahedral clusters with partial coordination. Data is grouped by the coordination number of the cluster, ranging from 8 to 11. The solid diamonds correspond to the sum of all partial icosahedral coordinations, also reported in Table 6.1. All data was fit using a linear regression. The error bars correspond to the standard deviation. Reproduced from reference (68).

is a minor decrease in the percentage of clusters on the order of the standard deviations. We also see that we are most likely to have crystalline partial clusters with coordination numbers of 9 and 7; as we saw for icosahedral clusters, we find only a small amount of clusters with large coordination numbers of 11.

The fact that icosahedral arrangements are favored over crystalline ordering is somewhat surprising, as we find for a large bulk system of nanopsheres without tethers that FCC/HCP crystalline ordering is dominant; icosahedral arrangements are favored only for simulations of small numbers of particles. In reference (67) we found that icosahedral ordering of nanoparticles was a result of the confinement that occurs as the system phase separates. We showed that by confining particles into cylinders with hard walls, there was a transition from predominantly crystalline ordering to predominantly icosahedral ordering when the diameter of the cylinder (scaled by particle size) was less than 5, corresponding to the approximate diameter of the domains in the DG system (67). For further discussion of the role of confinement, see section 5.2.2.

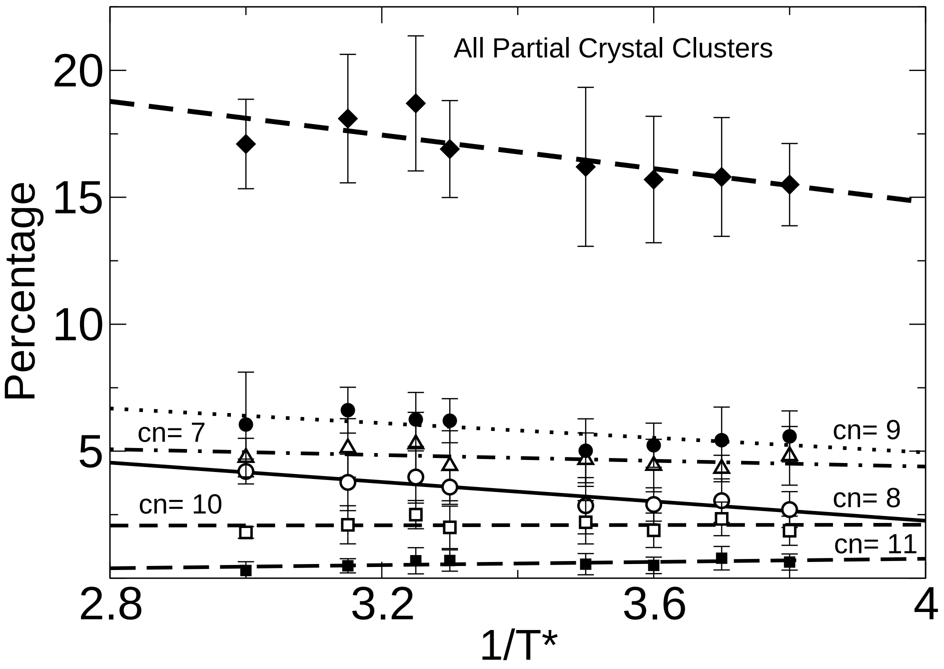

Figure 6.9 Percentage of nanospheres that are central particles in FCC and HCP clusters with partial coordination. Data is grouped by the coordination number of the cluster, ranging from 7 to 11. The solid diamonds correspond to the sum of all partial crystal coordinations, also reported in 6.1. All data was fit using linear regression. The error bars correspond to the standard deviation. Reproduced from reference (68).

6.4.2 Local structure of the TNR gyroid

Similar to the TNS system, the DG formed by the TNR system also has distinct local ordering of the nanoparticles in addition to the bulk microphase separation. Figure 6.10 shows a simulation snapshot of the TNR node. We notice that the nanorods attempt to adopt bundled structures, where a nanorod is surrounded by six nearest neighbors in a hexagonal fashion; a single bundle is highlighted in Figure 6.10. A six neighbor bundle is the densest, minimal potential energy structure for seven rods, representing full coordination, analogous to a coordination of 12 for an icosahedron. The tendency to form these bundles can be observed by examining the histogram of coordination number of the center-of-mass of each rod, shown in Figure 6.11 for 1/T* = 0.9. There is a clear bias towards high coordination numbers and we find no coordinations greater than six. We do find partially coordinated clusters as a result of rods being situated on the boundary with the tether region, as was also

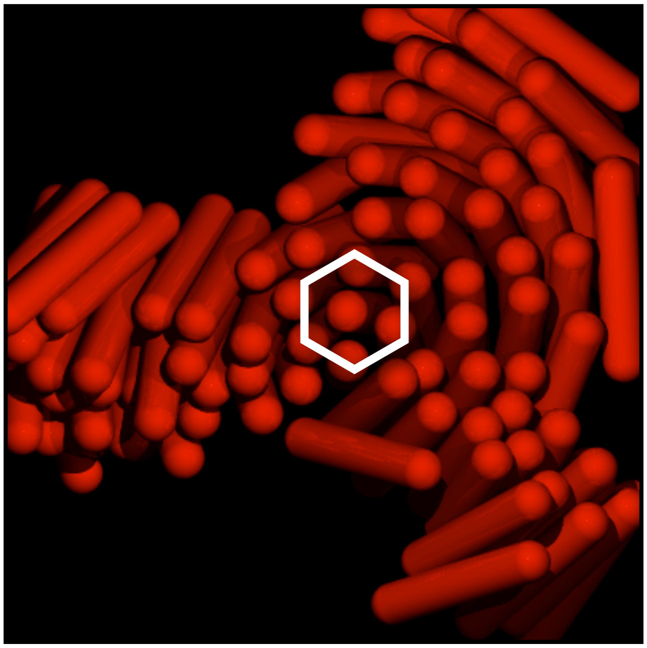

Figure 6.10 Node of the DG formed by the TNR system with a hexagonal bundle highlighted. Tethers have been removed for clarity. Reproduced from reference (68).

the case of the TNS system. Example clusters from our simulations are shown in Figure 6.12 for coordination numbers, cn = 3 - 6, where the preference to hexagonal packing is highlighted.

To reduce the grafting density of the tethers (i.e. the local density of tethers in a small region), thus maximizing entropy for the tether, we expect the grafting points of the tethers (i.e. the points in 3d space where the tether is attached to the nanorod) to be equally distributed along the interface between the nanorods and tethers. In Figure 6.11 we plot the histogram of the coordination number of the grafting points noticing a strong tendency for coordinations of one and two and do not find any coordinations above four. A bundle of seven rods would have the most unfavorable configuration in terms of entropy if the grafting point coordination number were six, corresponding to all tethers being oriented on the same side of the bundle. The histogram shows that each bundle has two or three tethers oriented in the same direction per bundle and thus tether attachment is well distributed.

We observe there is a deviation from the ideal hexagonally packed bundle structure as a result of the tether attachment; the bundles tilt and splay with respect to the central nanorod additionally reducing the grafting density of the tethers (73); this behavior is evident in the clusters in Figure 6.12. This manifests itself as a twisted structure in the tubes (arms) of the DG, as has been seen in previous simulations of tethered nanorods that form twisted

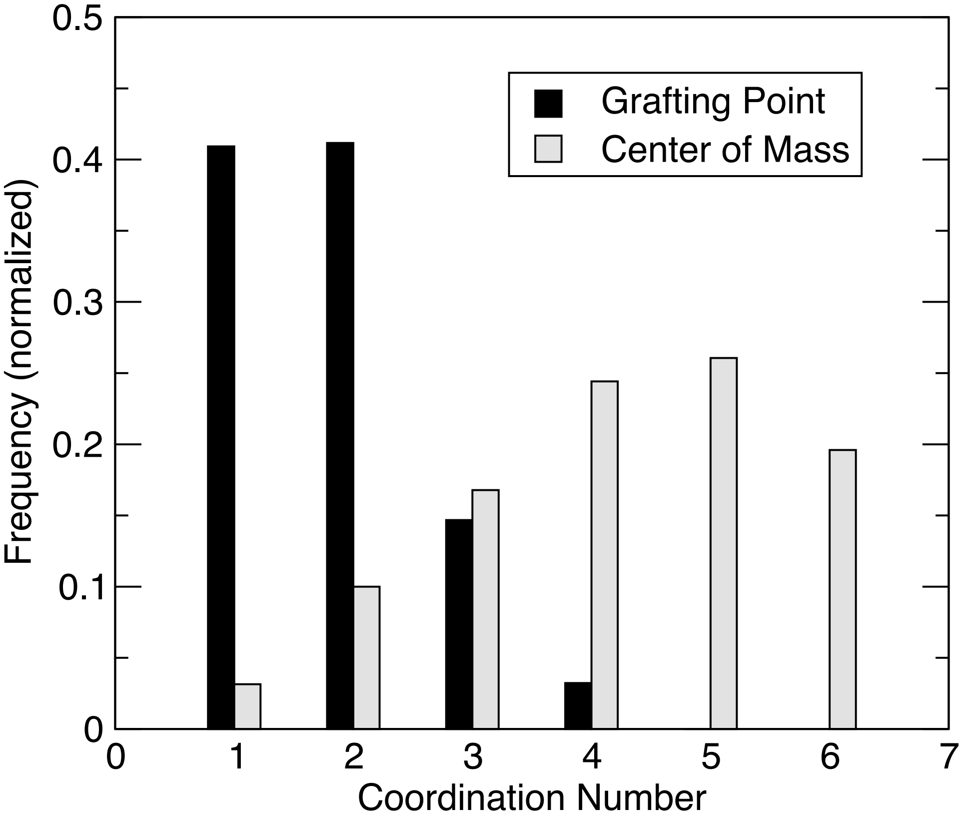

Figure 6.11 Histogram of the coordination number of centers-of-mass of the rods (grey) and a histogram of the coordination number of grafting points (black) for 1/T* = 0.9. Reproduced from reference (68).

cylinders (73). To quantify this behavior, we calculate the angle between the director of a nanorod with that of its nearest neighbors by calculating the dot product. On average we find that the angle between a nanorod and its neighbors is 10.7 degrees with a standard deviation of 6.1 degrees for a system with 1/T* = 0.9. Alternatively, we can quantify the splay of the rod bundles by calculating the nematic order parameter, *S*, for each bundle. To calculate the nematic order parameter, we first calculate the 3x3 nematic order tensor,

$$Q_{\alpha\beta} = \frac{1}{N}\sum_{i=1}^{N}\left(\frac{3}{2}u^i_\alpha u^i_\beta - \frac{\delta_{\alpha\beta}}{2}\right)$$

where α, β = x,y,z, u^i_α is the α component of the rod director and $\delta_{\alpha\beta}$ is the Kronecker delta (132). We take *S* to be the largest eigenvalue of the matrix Q (132). This construction results in perfectly crystalline systems having a value of *S*=1, nematic ordered liquid crystalline

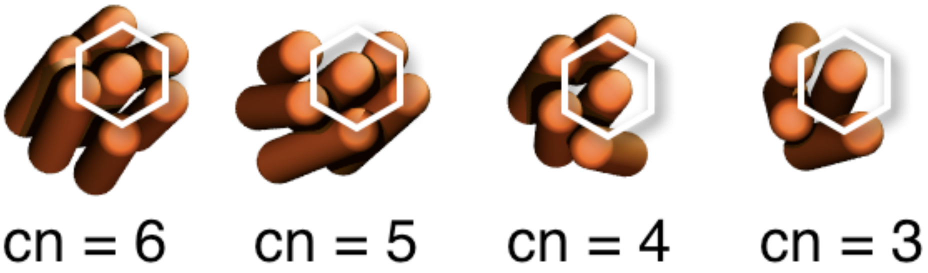

Figure 6.12 Example clusters formed by rods at 1/T* = 0.9 for coordination numbers 6, 5, 4, and 3. Reproduced from reference (68).

systems having *S*=0.3-0.9, and isotropic systems having S<0.3. We find that for a system with 1/T* = 0.9, the bundles of nanorods have an average value of *S*= 0.96, demonstrating a small deviation from the ideal crystalline behavior. Note that this is the average local nematic order parameter of the individual bundles, not the order parameter of the bulk system. An alternative form for the nematic order parameter is given by $S = (1/2)(3cos^2\theta - 1)$, where θ is the angle between a given nanrod and the director (21). Substituting the average splay angle of 10.7 degrees into this form yields a value of *S*=0.95 showing good agreement between these two methods of quantifying the splay.

In Table 6.2 we calculate both the average splay angle and nematic order parameter of the bundles for an example cooling sequence, where the system is equilibrated at each 1/T* prior to subsequent cooling; the transition from disordered to DG is denoted by the double line. We notice that for the ordered microphases (1/T* $>$ 0.8) the splay angle is roughly 10 degrees, with a standard deviation of 7.2 degrees for the lowest value of 1/T*, and 3.8 degrees for the highest value of 1/T*. Within the ordered region, the nematic order parameter deviates little from the average value of 0.965. Within the disordered region (1/T* $\leq$ 0.8), both the splay angle and standard deviation are large, suggesting that there is a large variation in alignment of a set of neighboring rods; this is supported by values of *S* that are clearly less than the average value for the ordered DG configurations, indicating that neighboring rods are not strongly aligned. The combination of splay angle and *S* allows us to conclude that, similar to the TNS system, there is a strong connection between microphase separation and local packing of the nanoparticles; we find strong local ordering where we find the DG, and very little local ordering elsewhere.

We also calculate the rotation of the rod as a function of time and 1/T* to assess the ability of the rods to reorient themselves. We calculate the average rotation of the rods by calculating the dot product of a rod's director at the current time with its initial starting

Table 6.2 Local coordination in TNR system. Reproduced from reference (68).

1/T*	Splay Angle (degrees) ± stdev	S
0.50	44.7 ± 25.7	0.73
0.70	34.8 ± 25.7	0.79
0.80	19.6 ± 17.3	0.88
0.85	11.4 ± 7.2	0.96
0.90	10.7 ± 6.1	0.96
0.95	10.0 ± 4.7	0.97
1.00	10.0 ± 4.7	0.97
1.10	9.7 ± 4.9	0.97
1.20	9.4 ± 3.8	0.97

director, as plotted in Figure 6.13. We find that at small values of 1/T* there is a large amount of rotational freedom in the rods; we note that the rods for 1/T*=0.5 have, on average, rotated approximately 85 degrees at time = 100 (i.e. 10000 timesteps). The large amount of rotational mobility explains the large splay angle and large standard deviation for high temperature disordered phases, as reported in Table 6.2. This rotational freedom is decreased as we increase 1/T* (i.e. cool the system); it is clear that for values of 1/T* $>$ 0.8, where the system has microphase separated into the DG, there is a drastic reduction in this rotational freedom and the average rotation of rods in the system is less than 15 degrees over the entire time range sampled. The lack of rotational mobility suggests that the direction of the rod is strongly correlated through time and, again, this supports the results in Table 6.2 where, for the DG, the distribution of splay angle is relatively narrow as compared to the disordered structure.

6.5 Summary

We have performed Brownian dynamics simulations of tethered nanospheres and tethered nanorods that predict the double gyroid structure. In both the tethered nanosphere and tethered nanorod systems we see a common trend towards the formation of dense, minimal potential energy structures. Tethered nanospheres predominantly form icosahedral clusters with partial coordination. Tethered nanorods form hexagonally packed bundles of rods, with both full and partial coordination, where the rods tilt and splay with respect to their neighbors. The icosahedral and hexagonal bundle structures adopted by the nanoparticles allow for a uniform density throughout the double gyroid structure; we do not see low

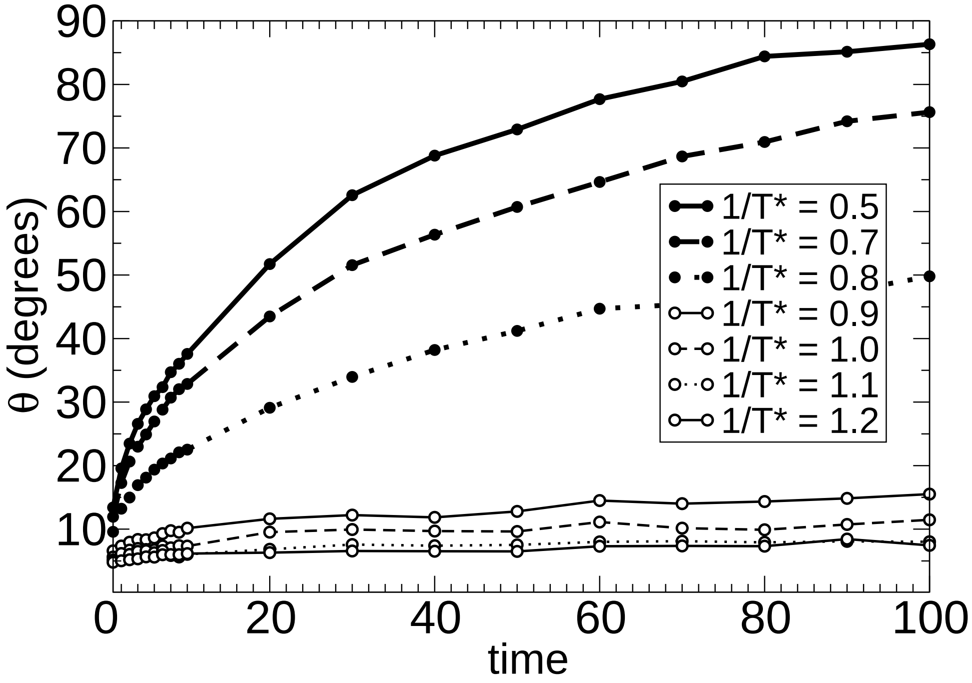

Figure 6.13 Average rotation as a function of time for various values of 1/T*. Solid black circles represent disordered microstructure, open circles correspond to the DG morphology. Reproduced from reference (68).

density regions at the nodes of the double gyroid as would be expected for flexible chains (122). The result of these local configurations is a reduction in packing frustration, which has been linked to the overall stability of the phase (120; 122; 26). We have seen that the rigidity of the nanorods is crucial for the stabilization of the double gyroid relative to BCPs; for equivalent conditions, we did not find the double gyroid structure for an analogous flexible diblock copolymer system. This suggests that by properly choosing the geometry of the nanoparticle, we may be able to not only stabilize the double gyroid, but potentially other bicontinuous structures by harnessing the unique combination of microphase separation and local packing.

Chapter 7

Quasicrystalline ordering

In this chapter we explore the emergence of quasicrystalline-like ordering of spherical micelles formed by mono-tethered nanospheres. We additionally propose a simple entropic model to explain the quasicrystalline order and explore the behavior of this model system. The work presented in this chapter is contained within a manuscript under preparation (133).

7.1 Introduction

Quasicrystals are a class of ordered structures that have long range orientational ordering but lack long range periodicity (134) possessing rotational symmetries that are "forbidden" for periodic crystals (135). Quasicrystals were first discovered for metallic alloys in the 1980s (136; 137; 138) and only recently have experiments suggested their self-assembly at larger length scales (139; 32). Quasicrystals are of particular interest for use as photonic bandgap materials (140; 141; 142) and wave guides (142), however their utility will strongly depend on size scale of the quasicrystal (i.e. mm, μm, or nm). In this work we explore the quasicrystalline-like ordering of spherical micelles formed by mono-tethered nanospheres. We compare the behavior of this system to the Dzugutov system, a system known to form quasicrystals. We propose a simple model to explain this behavior and a general scheme to create entropically stabilized quasicrystals.

7.2 Emergence of quasicrystalline-like ordering in mono-tethered nanospheres

In this work we explore the behavior of mono-tethered nanospheres (TNS) where the tethers are in a poor solvent and have a desire to aggregate. Tethered nanospheres are modeled as 8-bead tethers, where each bead is of diameter σ, connected to a single nanosphere

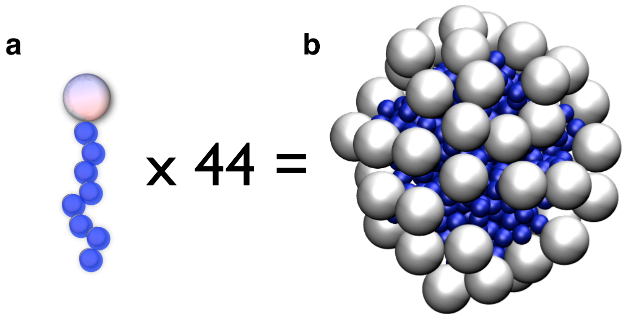

Figure 7.1 **(a)** Individual TNS building block. **(b)** Spherical micelle extracted from the TNS system. Tethers are shown as blue, nanospheres as white. Spherical micelles are composed of 44 TNS on average.

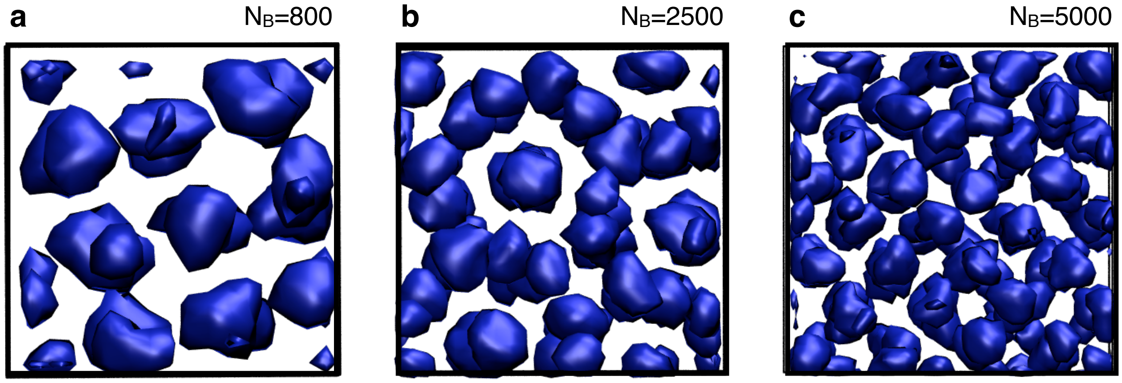

Figure 7.2 Isosurfaces of the micelles formed by the tethers as a function of the number of building blocks for ϕ = 0.27. **(a)** Nb=800 with BCC ordering of the micelles. **(b)** Nb=2500 with sigma phase ordering of the micelles. **(c)** Nb=5000 with BCC ordering of the micelles.

of diameter D=2.5σ; a schematic is shown in figure 7.1a. Tether-tether interactions are treated with the Lennard-Jones potential (LJ) and nanospheres are modeled by the Weeks-Chandler-Andersen potential (WCA) (see sections 5.1 and 3.1 for additional model details). Simulations are conducted using Brownian dynamics (BD) as described in section 3.2.

In reference (66) we found a variety of phases for the tether aggregating TNS system as a function of volume fraction, ϕ, and nanosphere diameter D. These phases include lamella, perforated lamellae, cylinders and spherical micelles (66). Spherical micelles are formed for D=2.5σ over the range of $\sim$0.25 < ϕ <$\sim$0.3. We initially identified the ordering between these spherical micelles simply as a cubic arrangement (i.e. bcc, fcc, or hcp) (66). In this work, to better understand the ordering among the spherical micelles, we explore the ordered phases as a function of system size by varying the box length, L_{box} and number of tethered nanosphere building blocks, N_B, for a fixed ϕ.

We first investigate systems at $\phi = 0.27$ for $L_{box} = [32.6, 47.6, 60.0]$ and $N_B = [800, 2500, 5000]$, respectively. As there are nine beads per building block, the total number of beads corresponds to N= [7200, 22500, 45000], respectively. We follow the same general simulation procedure used in reference (66), starting initially at a high temperature disordered state and incrementally cooling. Employing the center of mass calculation method outlined in section 4.2, we find that the three systems sizes are composed of $N_{micelles} = [20, 56, 114]$, respectively. We see that in all cases, the average number of building blocks per micelle is approximately 40-45 for all systems, thus the micelles themselves are nearly identical for the three box sizes considered. Using the R_{ylm} method introduced in section 4.1 we find that for $N_B = 800$ and 5000 the spherical micelles adopt BCC ordering; the cubic nature of these structures can be seen in figures 7.2a and c, respectively. For $N_B = 2500$ we do not find BCC ordering, but rather spherical micelles arranged in a sigma phase (143), as shown in figure 7.2b. The sigma phase is composed of ring-like arrangements of spheres that tile space in square and triangular arrangements. The sigma phase is a quasicrystalline approximate of a dodecagonal quasicrystal (143); since the box size is on the order of the size the tiling itself, even a true quasicrystal would form an approximate. Note that we utilize periodic boundary conditions and cubic boxes for the simulations shown in figure 7.2.

7.2.1 Sigma phase ordering

For N_B=2500, the sigma phase is found for the entire range of ϕ where spherical micelles form, specifically $\phi = [0.26, 0.27, 0.28, 0.29, 0.30]$. The order-disorder transition for the sigma phase appears to be approximately $1/T^* > 1.0$; Table 7.1 shows an example cooling sequence for $\phi = 0.27$. 15 independent datasets were simulated for N_B=2500 with cooling rates similar to that in table 7.1, in all cases resulting in the sigma phase. The formation of the sigma tiling is shown in figure 7.3a,b as a function of $1/T^*$ for $\phi = 0.27$, corresponding to the data presented in table 7.1.

As a result of the building block architecture and asymmetric immiscibility conditions, spherical micelles form with a core of tethers and an a surface coating of nanospheres. A micelle extracted from the system is shown in figure 7.1b where nanospheres are rendered in white and tethers in blue. The nanosphere “shell” around the micelle inner core produces micelles that interact only with a short ranged repulsive interaction (i.e. a potential that resembles WCA). Monoatomic systems of WCA spheres are not known to form the sigma tiling or quasicrystals for any box size. We perform NVT Nose-Hoover molecular dynamics (MD) simulations of WCA spheres at $\phi = 0.442$ using the LAMMPS simulation package

Table 7.1 Example cooling sequence for ϕ = 0.27, N_B = 2500, Δt = 0.01

1/T*	phase	number of timesteps
0.900	Disordered	$\sim 1.5 \times 10^6$
0.925	Disordered	$\sim 4.5 \times 10^6$
0.950	Disordered	$\sim 6.8 \times 10^6$
0.975	Disordered	$\sim 4.2 \times 10^6$
1.000	Sigma	$\sim 4.8 \times 10^6$
1.025	Sigma	$\sim 1.0 \times 10^7$
1.050	Sigma	$\sim 2.1 \times 10^6$
1.075	Sigma	$\sim 3.4 \times 10^6$

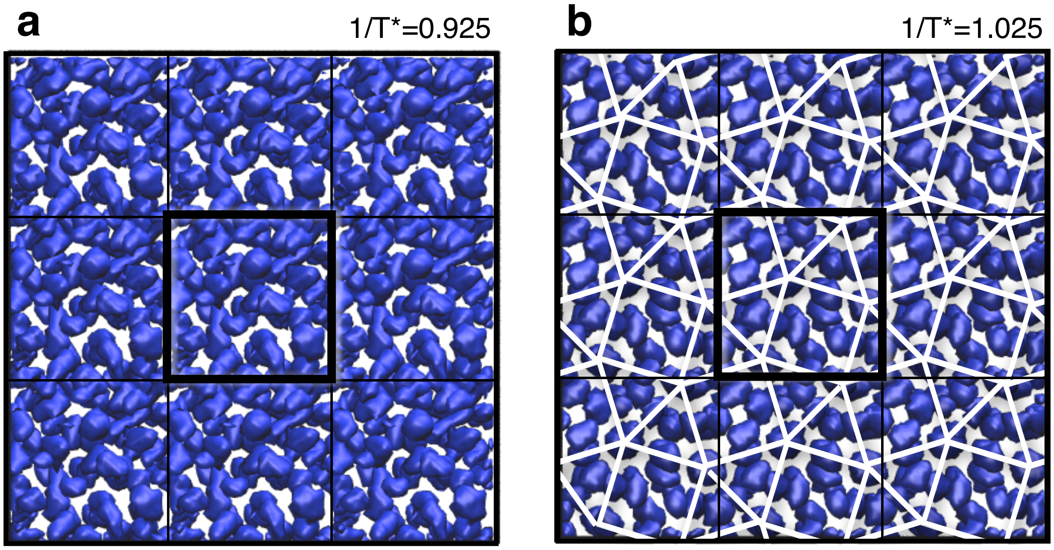

Figure 7.3 **(a)** Isosurfaces of the micelle cores (i.e. the tether regions) of the TNS system showing a disordered state at 1/T* = 0.925. **(b)** Isosurfaces of the tethers showing the sigma phase at 1/T* = 1.025. Both data sets at ϕ=0.27; the original systems were duplicated twice in each direction of the plane, unwrapping periodic boundary conditions, to clearly show the sigma tiling; the original system size is highlighted. Nanospheres are not shown.

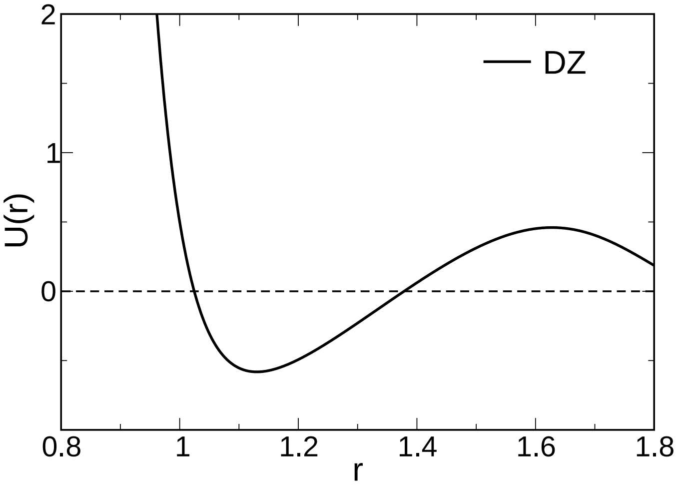

Figure 7.4 Plot of the Dzugutov potential (145).

(144) at various cooling rates finding only BCC ordered structures for $N_{particles}$ = [20, 56, 114] (corresponding to N_B = [800, 2500, 5000] in the TNS system, respectively).

However, it may still appear that the formation of the sigma phase is purely a box size effect, as both the smaller and larger systems we studied form BCC. As we previously noted, the size of our box for N_B=2500 is on the order of the size of the sigma tiling. Just as crystalline structures require box sizes commensurate with the lattice spacing, especially for small systems, the sigma phase also requires a commensurate box size for small systems. We can further address this by examining the Dzugutov potential (DZ) (145) which is known to form both crystalline structures and dodecagonal quasicrystals and approximates (i.e. the sigma phase). The DZ potential is shown in figure 7.4. We perform NVT Nose-Hoover MD simulations of the DZ potential for several different cooling rates at ϕ = 0.442 using the LAMMPS simulation package. For systems with $N_{particles}$ = [20, 56, 114] we find BCC, sigma phase, and BCC, respectively. Even for a known quasicrystal forming system, small systems can be biased towards BCC if the box size is not commensurate with the sigma/quasiperiodic tiling.

To additionally demonstrate that these results are robust and not finite size effect, we explore larger systems. Figure 7.5 shows isosurfaces of the tethers for a system of N_B = 5000, ϕ=0.27, 1/T* = 1.1 and a box length ratio of 2:1:1 (x:y:z). We find the system can be described by a tiling constructed of squares, triangles, and rhombs. The increased system size helps to minimize the impact of the box dimensions, suggesting that box size is not the

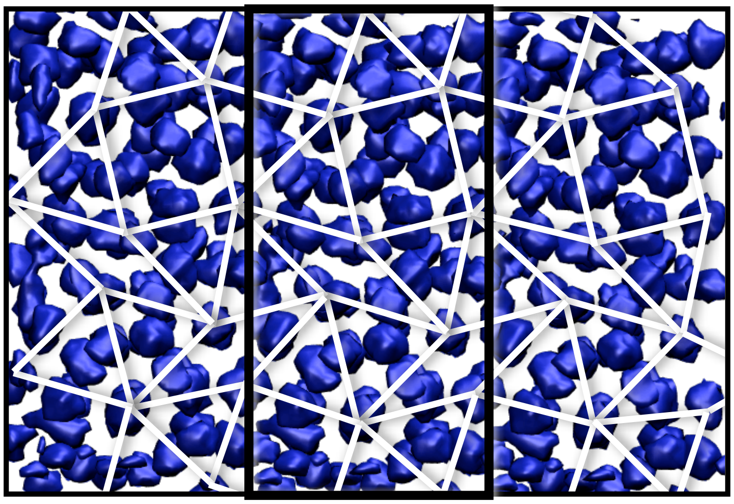

Figure 7.5 Isosurfaces of the tether domains of the TNS micelles showing an order state at 1/T* = 1.1, ϕ=0.27 and box dimensions ratio of 2:1:1. We find an arrangement of square, triangle, and rhomb tiles. The original system was duplicated twice in the x-direction to show the tiling; the original system size is highlighted.

sole cause of the quasiperiodic-like ordering we observe. However, we should note that this system is not completely independent of our original result for N_B = 2500 since the system length is an integer multiple of the N_B = 2500 box size.

Simulating a system large enough to be not biased by the box size requires a system containing a large number of particles. Large systems not only require longer CPU time to perform the same number of time steps, but since quasicrystals form via nucleation and growth (143), the time frame to grow the appropriately sized critical nucleus may be computationally intractable. By seeding the system we can speed the growth of the nucleus and then heterogeneous nucleation, thus speeding up the ordering processing. As such, we simulate systems with stationary seeds. We utilize a system with aspect ratio of 2:2:1, N_B=10000, ϕ=0.27 and 1/T*=1.075. Figure 7.6a shows the time evolution of a system seeded with two "rings". The seed was extracted from a previous simulation with N_B = 2500. The end result of this simulation is a sigma phase at time $\sim 10^7$, shown in figure 7.6a with the ideal tiling overlaid.

For comparison, we also simulate the DZ and WCA systems with seeds composed of two "rings". Both systems are cooled from T* = 1.0 to 0.25 over 5 x 10^5 timesteps, then run for another 5 x 10^5 timesteps at T* = 0.25; simulations were performed using NVT Nose-Hoover MD with a timestep of 0.01 in the LAMMPS simulation package (144). The time evolution of the DZ system is shown in figure 7.6b, where the sigma phase clearly

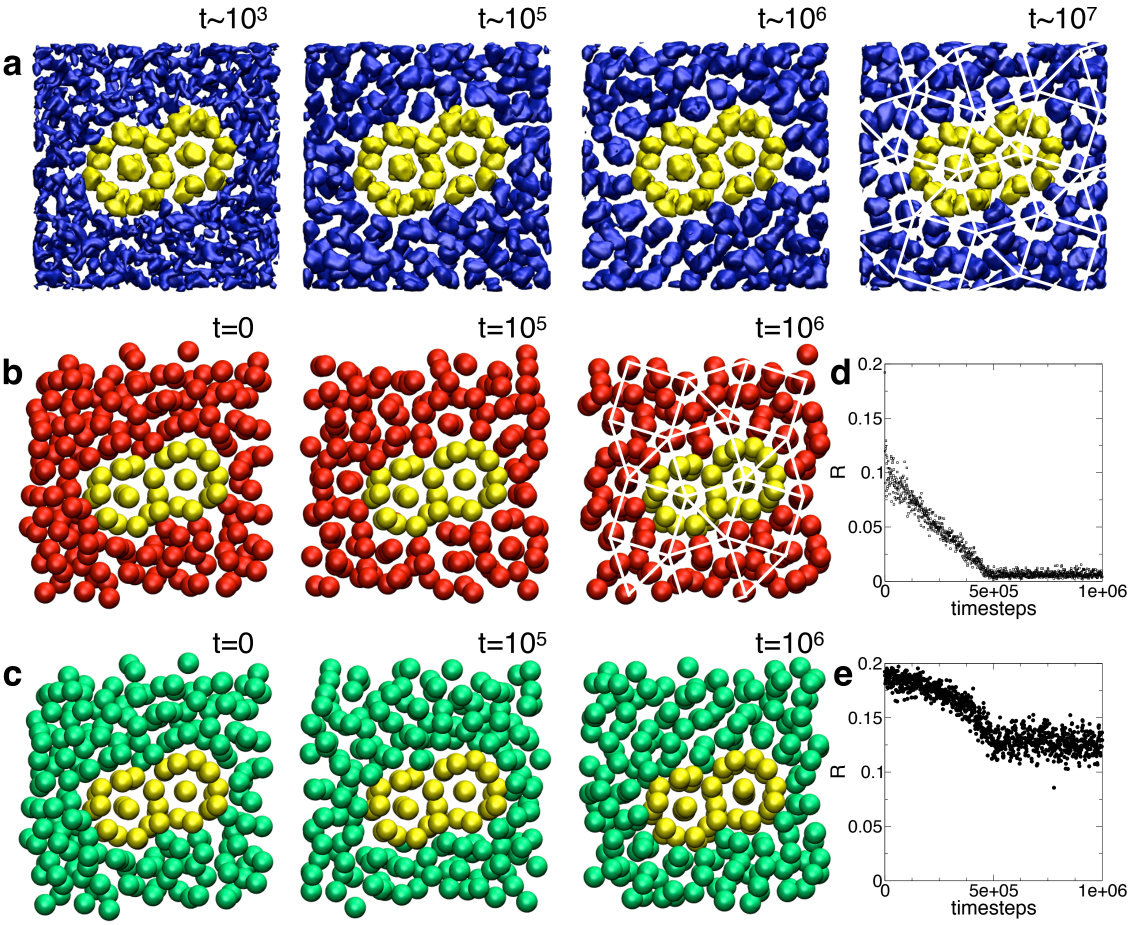

Figure 7.6 **(a)** Isosurfaces of the tether domains of the TNS micelle system seeded with a 2-ring seed as a function of time for aspect ratio of 2:2:1. For t $\sim 10^7$ the system evolves into a clear sigma phase. **(b)** DZ system seeded with a 2 ring seed as a function of time for aspect ratio of 2:2:1, forming a sigma phase at t=10^6. **(c)** WCA system seeded with a 2 ring seed as a function of time for aspect ratio of 2:2:1; the system remains liquid like over the entire time range. **(d)** Comparison between the DZ system and a perfect sigma phase as a function of time. **(e)** Comparison between the WCA system and a perfect sigma phase as a function of time. Both (d) and (e) use the R_{ylm} method to compare average system descriptors; a smaller R value denotes a closer match. Note that DZ and WCA systems are rendered at ~75% of their true size for clarity.

forms at t = 10^6. The time evolution of the WCA system is shown in figure 7.6b where it is clear that the sigma phase does not form. To quantify the ordering of the DZ and WCA systems, we modify the R_{ylm} method; rather than comparing individual clusters, we average the descriptors of all clusters and compare to the average descriptor describing the sigma tiling. Plots of the comparison with the sigma phase are shown for DZ and WCA in figures 7.6d and e, respectively. These plots support our visual observations; the DZ system has a near perfect match with the sigma phase for t $> 10^5$ attaining an R value of ~ 0, whereas

WCA does not match well and attains an R value of ~ 0.12 for $t > 10^5$.

From these seeding experiments we can draw two conclusions. First, since TNS micelles form the sigma tiling and WCA spheres remain disordered we can conclude that TNS micelles do not behave as WCA spheres. Our examination of the behavior of the WCA spheres as a function of system size also supports the conclusion that considering only the short ranged repulsion of the micelles is not a sufficient model to capture the essential physics of the TNS micelles (since we do not see the formation of the sigma phase). Second, since both the TNS micelles and DZ spheres form the sigma phase, this suggests that TNS micelles may be capable of forming quasiperiodic arrangements at large system sizes without seeding, as the DZ systems do. To better understand this unique ordering, we explore a simplified model system below.

7.2.2 Entropy stabilized quasicrystal model

We propose a simple model of the spherical micelles formed by the TNS to help us better understand the formation of the sigma phase. We treat the micelle core formed by the tethers as a single large sphere. Small spheres (analogous to the nanospheres) are attached to the surface of the large sphere using harmonic springs. Note that the small spheres are attached to the surface, not the center of the large sphere. This allows the small spheres a measure of mobility around their equilibrium point on the surface, while still ensuring a uniform surface coverage (this requires moving each large sphere as a rigid body). As a first approximation, we treat all interactions of the model “micelles” with the WCA potential; the potential between particles is appropriately shifted to properly account for the excluded volume of the large spheres (as discussed in section 3.1). For comparison, we roughly map to the TNS micelles by treating large spheres with a mass of 22 and small spheres a mass of 1. A schematic of the model micelles in comparison to the TNS micelles is shown in figure 7.7.

We explore a system with size ratio of large to small spheres of 3.75:1 and attach 44 small particles to the surface of each large sphere. We utilize systems of 56 building blocks with a harmonic spring constant, k=30. Starting from a disordered state, we cool systems from T* = 1.0 to 0.25 over 2 million time steps, and then allow the system to run for 100k timesteps at T*=0.25 using the LAMMPS simulation package (simulated using the Brownian dynamics method). We explore the phase behavior over a range of volume fractions. In figure 7.8a we plot the percentage of times the sigma phase forms, as determined using the R_{ylm} method with average descriptors. Each data point is calculated from at least 9 independent simulation runs with over 400 total simulations used to construct the plot. An

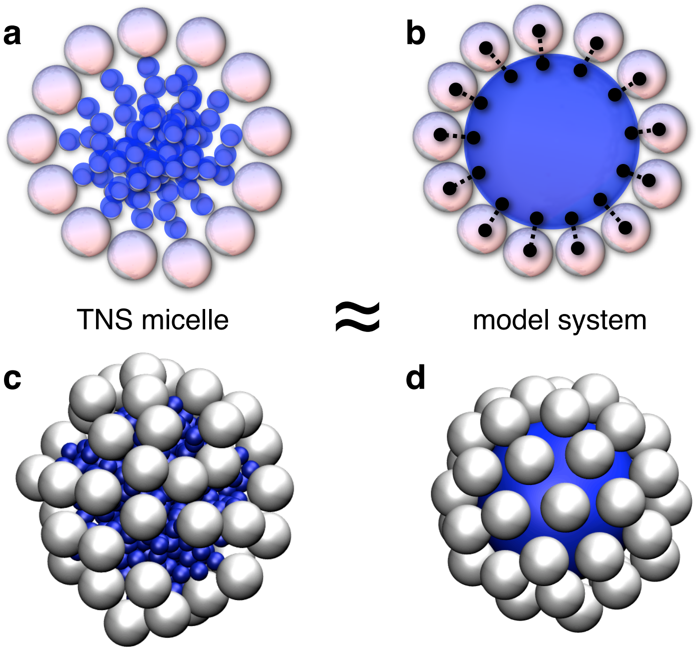

Figure 7.7 **(a)** Schematic of a spherical micelle formed by the TNS. **(b)** Schematic of the proposed model system. **(c)** An individual micelle extracted from a TNS simulation. **(d)** An individual "micelle" used in the model system.

example sigma phase formed by the model system is shown in 7.8b. A detailed study of this model system along with optimization of the model parameters will be explored in future studies. However, it is clear that the sigma phase reproducibly forms over a wide volume fraction range for our simplified, unoptimized model system.

7.3 Discussion

If we were to remove the small spheres from the surface of our model micelles, we would essentially have a WCA sphere; again, WCA spheres are only known to form cubic crystals over this volume fraction range. Clearly, the surface coating of small particles is very important to the formation of the sigma phase. In the DZ system, the formation of the quasicrystal is relatively easy to rationalize. The DZ potential has a repulsive bump at r $\sim 1.6\sigma$ (see figure 7.4) which corresponds to the intermediate length scale of ordering present in an FCC lattice. This makes it energetically unfavorable for the system to crystallize into FCC (as would be expected for an attractive LJ system) and drives the system to form the sigma phase or a dodecagonal quasicrystal (146).

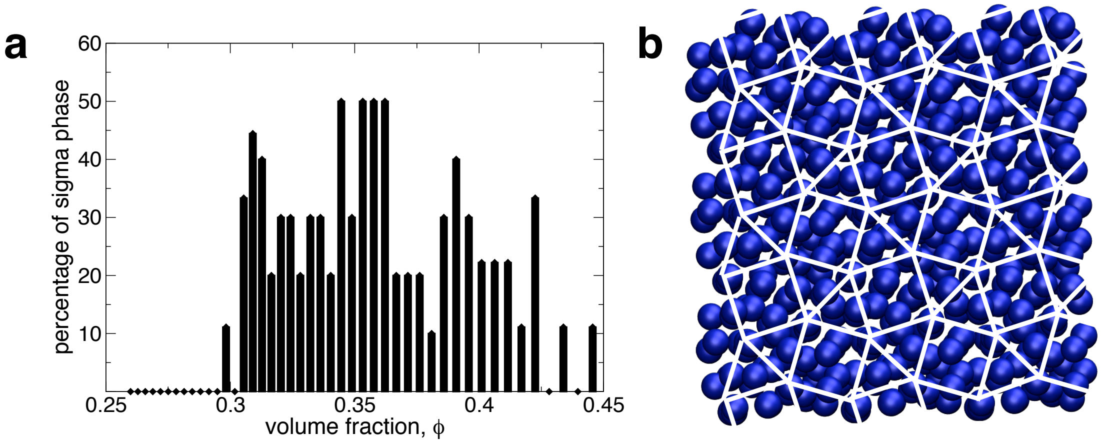

Figure 7.8 **(a)** Percentage of sigma phases that were observed as a function of volume fraction. Each data point is generated from at least 9 independent simulations, with over 400 total simulations used to construct the entire plot. **(b)** Rendering of the sigma tiling for the model system, duplicated twice in each direction of the plane to show the tiling at $\phi = 0.328$. Note only the large spheres are shown for clarity.

The tendency for our micelle system to form the sigma phase is less straight forward than the DZ system since the micelles essentially have no energetic component (i.e. the interactions between spheres on the surface of the micelles is essentially only excluded volume, and we've previous shown that WCA spheres only form BCC). By coating the large spheres with mobile small spheres, we create a system with two entropic contributions to the free energy. The ordering of the system is driven by the tendency of both the large and small spheres to maximize their entropy. We can understand why the sigma phase forms if we consider the entropy of the small spheres to be maximized when their accessible free volume is uniformly maximized throughout the system (i.e the accessible free volume is the same for each of the small spheres, regardless of position). In order for this condition to be satisfied, the small spheres would prefer the large spheres adopt a spherically symmetric configuration. If we compare a cubic crystal (such as FCC or BCC) to a Frank-Kasper polyhedra (such as those found in quasicrystal), it is clear that the polyhedra is more spherically symmetric than a cubic crystal, as shown in figures 7.9a and b. A cubic crystalline arrangement of the large spheres will tend to compress the small spheres in certain directions, while allowing for more free volume in other directions; a schematic of this behavior comparing a 2D "equivalent" of BCC to a 2D equivalent of an icosahedron is shown in figures 7.9c and d. Polyhedral arrangements found in quasicrystals essentially have one length scale accessible to the small spheres, thus all particles will have essentially the same amount of free volume available to them, regardless of location in the system.

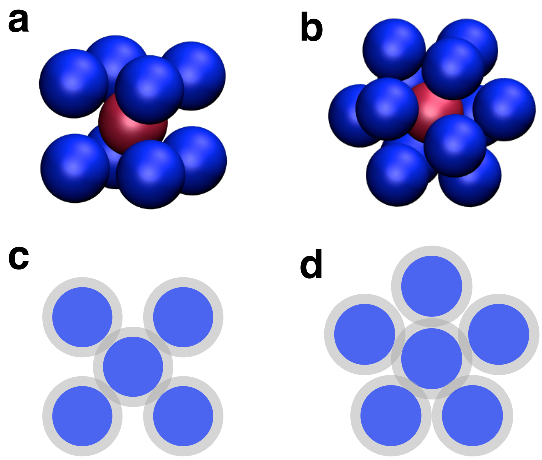

Figure 7.9 **(a)** Unit cell of BCC, where the central particle is shown in red. **(b)** An icosahedron, which is a 13 particle polyhedra, where the central particle is shown in red. **(c)** 2D schematic of the a cubic crystalline structure. **(d)** 2D schematic of a polyhedral arrangement. The polyhedra shown in (b) and (d) have more spherically symmetric than the cubic crystal structures shown in (a) and (c).

To validate this, we investigate the behavior of the model system as a function of spring constant. If we increase the spring constant that ties the small spheres to the large spheres, we reduce their entropic contribution to the free energy; the amount of accessible free volume available to the small spheres will reduce as a result of being more strongly tied to the surface. We therefore expect that as the entropic contribution of the small spheres is decreased, the likelihood of sigma phase ordering also decreases. In figure 7.10 we plot the percentage of times the the sigma phase was observed as a function of spring constant for a fixed volume fraction, $\phi = 0.358$, where each data point is generated from 20 simulations. We observe that smaller spring constants are much more likely to form the sigma phase than large spring constants, as expected.

Furthermore, this simple model can also be used to explain the formation of the sigma phase (147) and dodecagonal quasicrystal phase (139) reported for dendrimer "micelles" (i.e. spherical dendrimers molecules). These dendrimers are highly branched molecules with relatively impenetrable spherical cores, functionalized with short polymer molecules. There is a clear analogy between our spherical micelles and the dendrimer system; our spherical micelles are essentially impenetrable cores decorated with the one-bead limit of a bead spring polymer chain. The entropy constraints of the short polymers and nanospheres act in much the same way, driving the system away from cubic crystalline arrangements in favor of more uniform polyhedra found in quasicrystals. As such we believe our model provides a general method to control crystallization; by controlling the entropy contribution of the

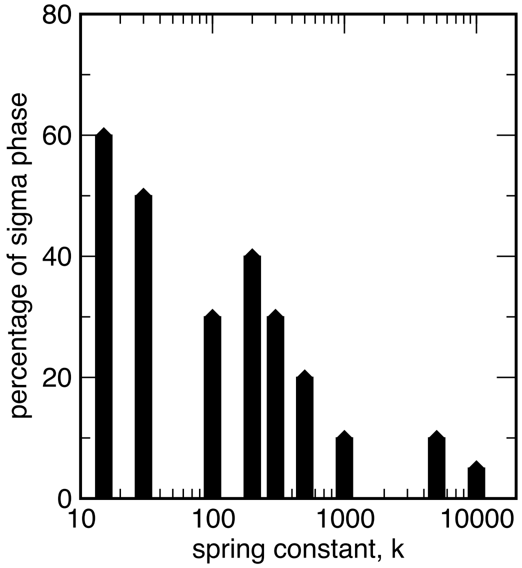

Figure 7.10 Percentage of times the sigma phase formed as a function of spring constant, k, for ϕ = 0.358 and N=56. The same cooling rate was used as described previously.

surface coating of a micelle or particle, we can drive the system to form quasicrystalline structures.

7.4 Summary

In this work we explored the ordering of spherical micelles formed by tether-aggregating TNS. We find BCC ordered spherical micelles, as we might expect from block copolymers and surfactants (23; 25). We also find micelles that order into the sigma phase, a dodecagonal quasicrystal approximate. Within this work, we find nearly identical behavior between the TNS system and the quasicrystal forming Dzugutov system. We also propose a simple entropic model to explain the formation of the TNS quasicrystal approximate. Our model also can be used to explain the formation of quasicrystalline materials found in dendrimers (139; 147). Our model provides a general method to control crystallization, potentially allowing experimentalists to design building blocks that can be predictively used to fabricate quasicrystals on a variety of length scales. For example, core-satellite nanoassemblies fabricated by Sebba, *et al.* consist of 13 nm gold satellite particles connected by reconfigurable DNA to 50 nm gold core particles(148). The size ratio of the particles is 3.85, closely matching the size ratio of 3.75 used in our model system. Thus one might only need to tune the characteristics of the DNA linkers to drive the system to form quasicrystalline materials.

Chapter 8

Phase behavior of di-tethered nanospheres

In this chapter we explore the phase behavior of di-tethered nanospheres under melt-like conditions. In section 8.2 we explore the phase behavior as a function of planar angle separating the tethers, nanosphere diameter, and immiscibility. We find a robust phase behavior and compare this phase behavior with linear and star triblock copolymers. We also explore the phase behavior as a function of block fraction and immiscibility in section 8.3 to understand how asymmetry can impact the phase behavior. The work presented in this chapter has been accepted for publication in reference (71) and is also contained in an additional manuscript in preparation (86).

8.1 Introduction

Recent attention in the literature has focused on methods to self-assemble nanometer and micron sized particles into highly ordered structures for use in photonic (149; 150), electronic (151), and medicinal applications (152). For example, binary nanoparticle superlattices (153; 150) and ionic colloidal crystals (154) have been reported with structures reminiscent of atomic crystals, e.g. NaCl and CsCl. Complex phases, such as the double diamond lattice (155), have been synthesized for covalently linked systems of tetrapods. Other methods to assemble nanoparticles have relied on anisotropic interactions, e.g. dipole moments (156; 157; 158; 50) and surface patterns (159; 160; 161; 63; 162), to create wires(156; 158; 163), free-floating sheets (50), and 2-d crystals (159). In previous work, we examined two methods to assemble particles into ordered arrays and other complex structures using anisotropic interactions: "patchy particles" (162) and "tethered nanoparticles" (17). Patchy particles are nano or micron sized particles with directional interactions conferred via patches on their surface. The location of patches dictates the local ordering and structure, ranging from square packed sheets (162) to the diamond lattice (164). Tethered nanoparticles are hybrid nanoparticle-polymer building blocks where nanoparticles are bonded as “head groups” to immiscible polymer tethers to create a new type of amphiphile. The immiscibility between the nanoparticle and polymer tether facilitates microphase separation into bulk periodic structures similar to those observed in block copolymers, including phases such as lamellar sheets (66; 67; 73), ordered cylinders (66; 67; 73), and the double gyroid (67; 68), but with additional ordering arising from the nanoparticle shape.

In this work, we examine the self-assembly of di-tethered nanospheres that possess characteristics of both patchy particles and tethered nanoparticles. Just as mono-tethered nanoparticles are analogous to single-tailed surfactants and diblock copolymers, DTNS have some analogy with double-tailed surfactants and triblock copolymers, however, with additional levels of complexity and anisotropy that can be exploited for self-assembly. Recent work in the literature has demonstrated the synthesis of nanospheres functionalized with diametrically opposed tethers, showing the formation of wires under dilute conditions (63; 165) and preliminary indications of self-assembled cylinders (166), as predicted in earlier simulations (17). This makes DTNS an interesting new building block that heretofore has not been studied exhaustively but which holds great promise for self-assembly. Here we explore the phase behavior as a function of both immiscibility (via interaction strength) and directionality of the interactions (via the planar angle θ between tethers). As a result of the immiscibility and directionality of the interactions, DTNS possess characteristics of both tethered nanoparticles and patchy particles, combining phase separation with architectural constraints. Such constraints are often found in liquid crystalline molecules that have been shown to assemble into a wide array of complex structures such as toroids (167) and helices (168). We explore the phase behavior of nanospheres that have two short polymer tethers attached to their surfaces, separated by an angle θ. We explore a regime where tether length is short enough such that tether location is correlated to the attachment point, but not so short as to approach the limit of a patchy particle. A schematic of this range is shown in figure 8.1a-c. The di-tethered nanosphere system can be loosely thought of as a nanoparticle equivalent of an ABC triblock copolymer where, in this case, the center block of a triblock has been replaced by a nanosphere. We would expect the phase behavior of di-tethered nanospheres to be similar in some respects to an ABC triblock copolymer, since both objects contain three distinct, immiscible “blocks.” Triblock copolymers possess a complex phase behavior with a greater diversity of structures than those observed in diblock copolymers or their monotethered nanoparticle equivalents. In the following sections, we explore the phase behavior of di-tethered nanospheres and compare with the behavior of linear and star triblock copolymers.

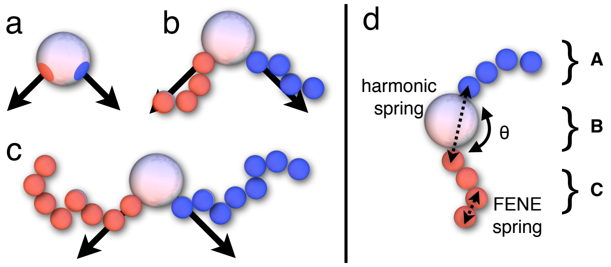

Figure 8.1 Schematic of **(a)** patchy particle with localized patches on the surface, **(b)** DTNS with short tethers, and **(c)** DTNS with long tethers. The arrows are drawn from the center of the nanosphere through the attachment site to highlight the correlation between tether location and attachment. We conduct simulations in the range of schematic (b) where tether locations are correlated to their attachment points. **(d)** Schematic of the DTNS building block. The blue colored tether is labeled as A, the nanoparticle as B, and the red tether as C. Reproduced from reference (71).

8.2 Phase behavior as a function of planar angle, nanoparticle diameter and immiscibility

In this section we explore the phase behavior of di-tethered nanospheres under melt-like conditions as a function of planar angle, immiscibility, and nanoparticle diameter. Nanospheres are modeled as spheres of diameter D connected to two chemically distinct tethers of length 4 beads, where each bead has a diameter σ. The diameter of the nanosphere is varied, where D=1.5σ, 2.0σ, and 2.5σ. Simulations are conducted under melt-like conditions where like species interact with the Lennard-Jones (LJ) potential and dislike species interact with the repulsive Weeks-Chandler-Andersen (WCA) potential, consistent with the model described in section 3.1. The angle between tethers, θ, is controlled by a harmonic spring with with k = 30 and $R_0 = (D+\sigma)sin(\theta/2)$ (see section 3.1 for more details). Simulations are performed at a fixed volume fraction of ϕ=0.45 using the method of Brownian dynamics (BD), as described in section 3.2. We vary θ from 30° to 180°; this spans the range from a situation where tethers are essentially tethered to the same point on the nanosphere (i.e. θ=30°) to the limit where they are diametrically opposed (i.e. θ = 180°). A schematic of the building block is shown in figure 8.1d.

First, we describe the overall phase behavior, grouped by nanosphere diameter D, summarized in the phase diagrams shown in figures 8.2a-c. The individual structures are discussed in detail in the subsections that follow. Throughout this chapter, figures are color coded as shown in figure 8.1d; A tethers and the aggregates they form are colored blue, B nanoparticles are white/gray, and C tethers are red.

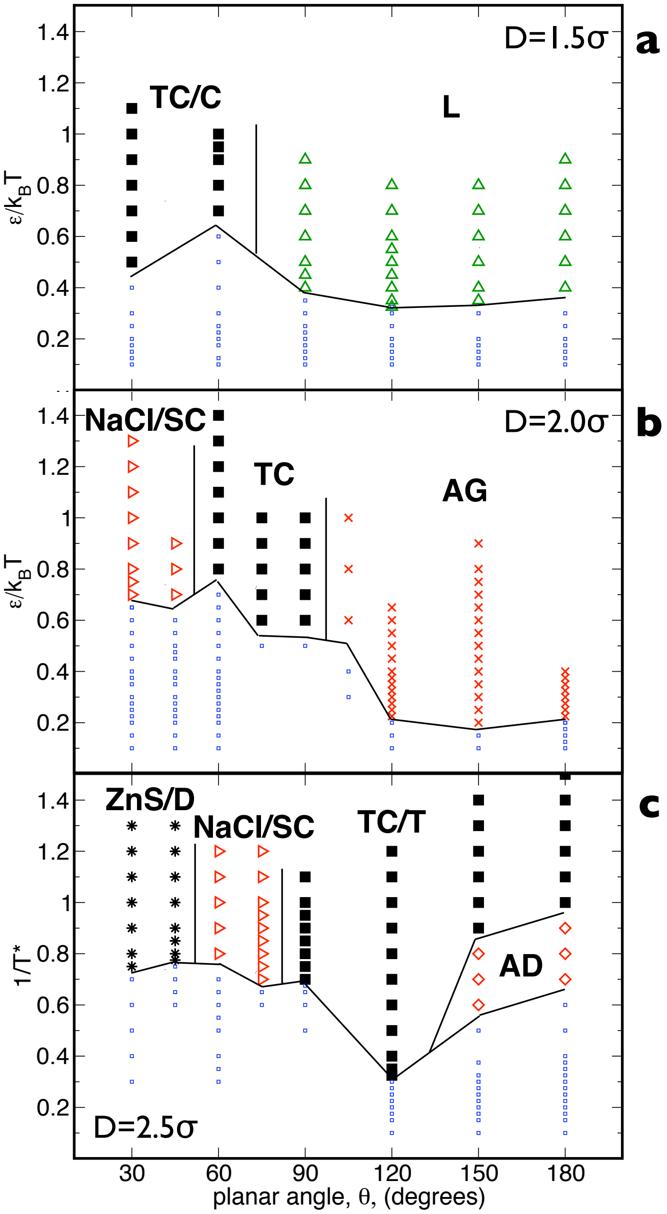

Figure 8.2 Phase diagrams as a function of planar angle, θ, and T*. **(a)** For nanosphere diameter D=1.5σ we find two structures: 1) alternating tetragonally ordered cylinders formed by the tethers where the nanospheres also form cylinders (TC/C); and 2) lamellar sheets (L). **(b)** For nanosphere diameter D=2.0σ we find three structures: 1) NaCl ordered spherical micelles where nanospheres form a complementary simple cubic network (NaCl/SC); 2) alternating tetragonally ordered cylinders formed by the tethers where the nanospheres form cylinders or a tetragonal mesh (TC); and 3) alternating double gyroid structure within a nanosphere matrix (AG). **(c)** For nanosphere diameter D=2.5σ we find four structures: 1) ZnS (i.e. binary diamond) ordered spherical micelles where nanospheres form a complementary diamond network (ZnS/D); 2) NaCl ordered spherical micelles where nanospheres form a complementary simple cubic network (NaCl/SC); 3) alternating tetragonally ordered cylinders formed by the tethers where the nanospheres form a tetragonal mesh (TC/T); and 4) alternating double diamond structure within a nanosphere matrix (AD). Phase boundaries are approximate and drawn to guide the eye. Adapted from references (71) and (86).

8.2.1 D=1.5σ phase behavior

For a nanosphere diameter of D=1.5σ the phase behavior is limited to two structures, specifically cylinders and lamella, as shown in figure 8.2a . For $30^\circ < \theta < 60^\circ$ we find a phase of alternating tetragonally ordered cylinders formed by the tethers where nanospheres also form cylinders (TC/C). For $90^\circ < \theta < 180^\circ$ we find lamellar sheets where nanospheres form monolayers (L/M).

8.2.2 D=2.0σ phase behavior

As the nanosphere diameter is increased to D=2.0σ, three phases are found as shown in the phase diagram in figure 8.2b. For $30^\circ < \theta < 45^\circ$ we find a phase of NaCl ordered spherical micelles formed by the tethers with a complementary simple cubic network of nanospheres (NaCl/SC). For $60^\circ < \theta < 90^\circ$ we find alternating cylinders formed by the tethers (TC). Depending on the value of θ and T*, the nanospheres either order into a tetragonal mesh that separates the tethers or into individual cylinders. For $105^\circ < \theta < 180^\circ$ we find the alternating gyroid structure within a matrix of nanospheres (AG).

8.2.3 D=2.5σ phase behavior

For a nanosphere diameter of D=2.5σ we find four distinct structures: two spherical micelle structures, alternating cylinders, and alternating diamond, as shown in the phase diagram in figure 8.2c. For $30^\circ < \theta < 45^\circ$ we find a phase of zincblende (binary diamond) ordered spherical micelles formed by the tethers with a complementary diamond network of nanospheres (ZnS/D). For $60^\circ < \theta < 75^\circ$ we find NaCl ordered spherical micelles formed by the tethers with a complementary simple cubic network of nanospheres (NaCl/SC). For $90^\circ < \theta < 180^\circ$ we find alternating cylinders formed by the tethers where the nanospheres form a tetragonal mesh that separates the cylinders (TC/T). For $150^\circ < \theta < 180^\circ$ we find the alternating diamond structure (AD) within a matrix of nanospheres.

8.2.4 Lamellar sheets/nanosphere monolayer (L/M)

A simulation snapshot of a lamellar structure for D=1.5σ, θ=150° and 1/T*= 0.8 is shown in figure 8.3. Nanospheres form monolayers sandwiched between alternating layers of tethers. The spacing between the layers varies with θ. To determine the spacing between the layers, we first calculate S(q). For lamella, the spacing between layers (i.e. periodicity) can be calculated using $L_{spacing} = (2\Pi/q*)$, where $q*$ is the modulus of the wave vector at which the first principal S(q) maximum is located (122; 116). From this, we find that for D=1.5σ and θ = 90° the average spacing $L_{spacing} \sim$ = 3.9σ and for D=1.5σ and θ = 180° $L_{spacing} \sim$ = 4.3σ; the spacing does not appear to depend on 1/T* given we are in the ordered regime.

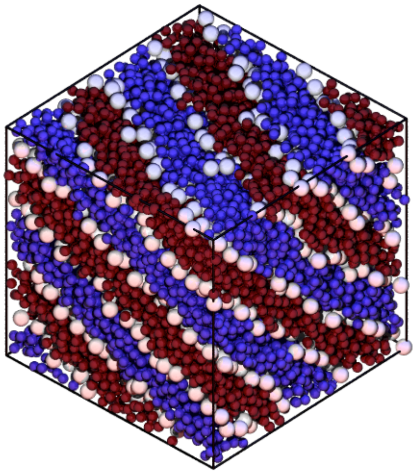

Figure 8.3 Lamella structure formed for D=1.5σ, θ=150° and 1/T*= 0.8 showing a monolayer of nanospheres. The spacing between the nanosphere layers is ∼4.2σ. Reproduced from reference (86).

8.2.5 Alternating tetragonally ordered cylinders/nanosphere cylinders or tetragonal mesh (TC/C and TC/T)

Each nanosphere diameter investigated demonstrated a cylinder phase. In all cases, we find a cross-sectional checkerboard pattern of alternating tetragonally ordered cylinders formed by the tethers. However, the arrangement of the nanospheres is different when we considere different nanosphere diameters. For D=1.5σ nanospheres organize into cylinders, as shown in figure 8.4a. In contrast, for$D$=2.5σ nanospheres organize into a tetragonal mesh that separates the alternating cylinders, as shown in figure 8.4b. In both cases, the structures can be described by the [8,8,4] Archimedean tiling constructed of octagons and squares, shown in figure 8.4c for D=1.5σ and figure 8.4d for D=2.5σ. We should note that for D=1.5σ tethers occupy the octagonal tiles and nanospheres occupy the square tiles, where as for D=2.5σ both tethers and nanospheres occupy the octagonal tiles and only nanospheres occupy the square tiles.

For D=2.0σ we see a both tetragonal and cylindrical morphologies of nanospheres. As the value of 1/T* increases (i.e. we cool the system), there is a gradual transition from a tetragonal mesh of nanospheres to distinct cylinders of nanospheres, shown in figures 8.4e-f.

Figure 8.4e shows an isosurface of the nanoparticles corresponding to 1/T* = 0.8 and figure 8.4f corresponds to 1/T* = 1.6, both for D=2.0σ and θ=60° and the same isovalue. Conceptually, the tetragonal phase is the cylinder phase with connections between the cylinders; figure 8.4e demonstrates a large number of connections between cylinders, where as in figure 8.4f there are almost none. There appears to be a gradual reduction of the number connection between the cylinders as 1/T* increases (i.e. the transition from tetragonal to cylinders), making the transition difficult to definitively identify.

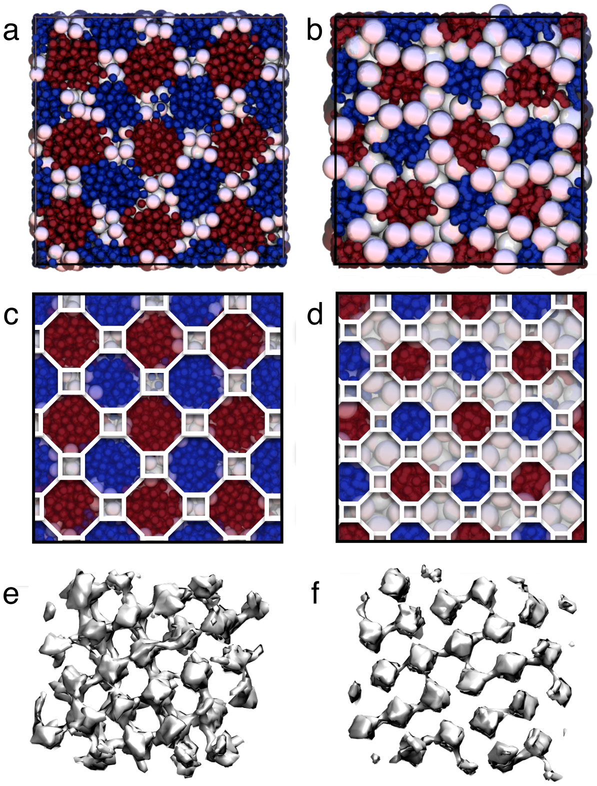

Figure 8.4 **(a)** Simulation snapshot of the end view of the TC/C phase for D=1.5σ, θ = 60°, and 1/T* = 0.8. **(b)** Simulation snapshot of the end view of the TC/T phase for D=2.5σ, θ = 90°, and 1/T* = 0.8. **(c)** [8,8,4] Archimedean tiling overlayed on the simulation snapshot in (a). **(d)** [8,8,4] Archimedean tiling overlayed on the simulation snapshot in (b). **(e)** Isosurface of the tetragonal mesh for D=2.0σ, θ = 60°, and 1/T* = 0.8. **(f)** Isosurface of the cylinder phase for D=2.0σ, θ = 60°, and 1/T* = 1.6. Reproduced from reference (86).

8.2.6 Alternating gyroid/nanosphere matrix (AG)

A simulation snapshot of the alternating gyroid structure is shown for D=2.0σ, θ=180°, and 1/T* = 0.4 in figure 8.5. The AG structure consists of two chemically distinct gyroid networks, one network formed by the A tether and one formed by the C tether, separated by a matrix of nanospheres. The AG structure has the same Ia3d space group of the double gyroid (DG) structure previously discussed in section 6, however each gyroid network is chemically distinct in the AG phase. This structure was identified both visually and by the use of the structure factor, S(q),(169) finding characteristic peaks in ratio $\sqrt{3} : \sqrt{4} : \sqrt{10} : \sqrt{11}$ as expected (122) and shown in figure 8.5d.

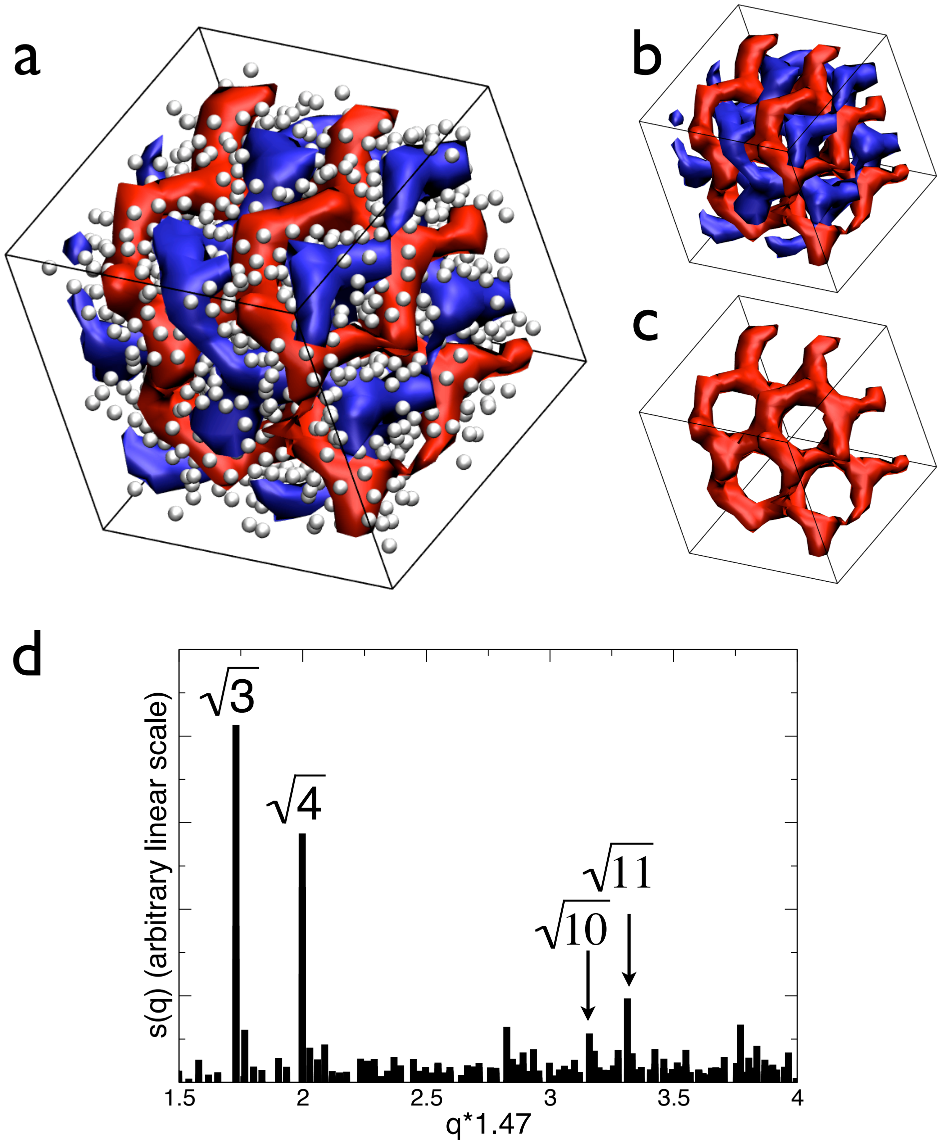

Figure 8.5 **(a)** Isosurfaces of the two tether domains, which self-assembled into the AG structure showing 8 unit cells with a unit cell size of 13σ; nanospheres are rendered at half their true size. **(b)** Isosurface of the two tether domains. **(c)** Isosurface of a single gyroid network formed by the tethers. **(d)** Structure factor of the AG phase. All data for D=2.0σ, θ = 180° and 1/T* = 0.4. Reproduced from reference (86).

8.2.7 Alternating diamond/nanosphere matrix (AD)

The alternating diamond phase, shown in figure 8.6a for D=2.5σ, θ =180° and 1/T*=0.8, consists of two chemically distinct, interpenetrating diamond networks, one formed by the A tether and one formed by the C tether, separated by a matrix of nanospheres. A snapshot of a single diamond network is shown in 8.6b. This phase could also be classified as the double diamond structure (DD) if we ignore the chemical specificity of the two diamond networks. Each diamond network is composed of cylindrical tubes, where four tubes connect at a node in a tetrahedral arrangement. An individual node of the AD phase is shown in figure 8.6c. This structure was identified visually and by calculating the structure factor, S(q). S(q) for the alternating diamond phase is plotted in figure 8.6b, showing characteristic peaks with ratio $\sqrt{2} : \sqrt{3} : \sqrt{4} : \sqrt{6}$ as expected (26); for ease of viewing the x-axis was scaled by 1.34, such that the numerical values on the x-axis correspond to the values in the characteristic ratio (i.e. the first peak occurs at a numerical value of $\sqrt{2}$).

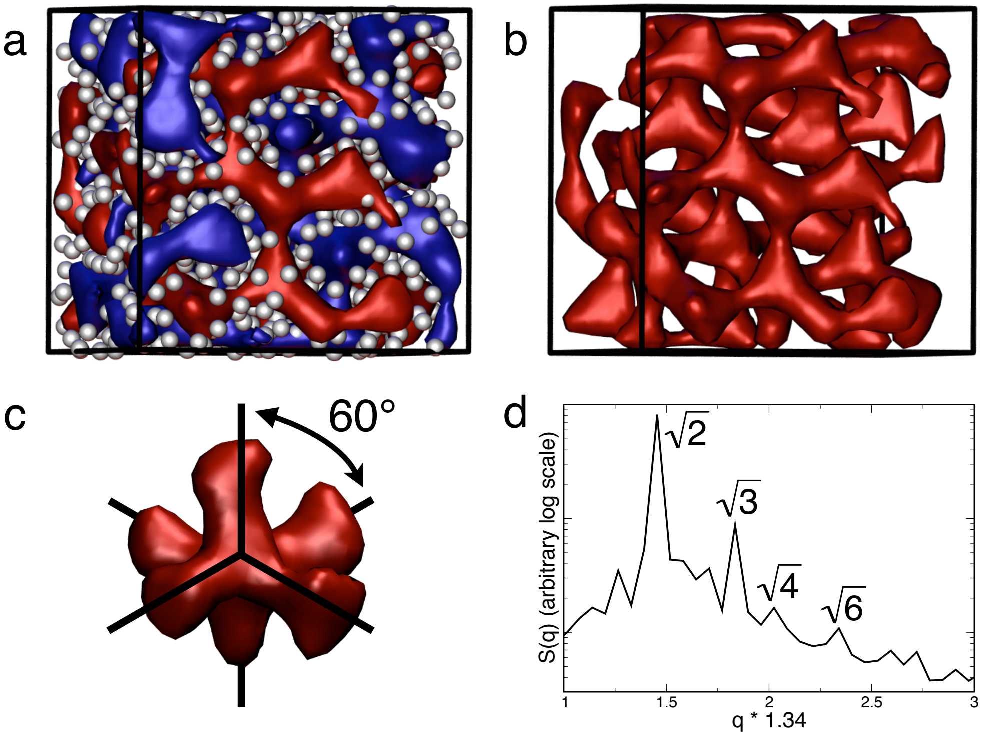

Figure 8.6 **(a)** Isosurfaces of the two tether domains, which self-assembled into the AD structure showing 27 unit cells with a unit cell size of 10σ; nanospheres are rendered at half their true size. **(b)** Isosurface of a single diamond network formed by the tethers. **(c)** Simulation snapshot of a single diamond node, extracted from the system. **(d)** Structure factor of the AD phase. All data for D=2.5σ, θ = 180° and 1/T* = 0.8. Reproduced from reference (71).

8.2.8 NaCl ordered spherical micelles/nanosphere simple cubic network (NaCl/SC)

For D=2.0σ and 2.5σ the tethers form spherical micelles that order into an NaCl lattice with a complementary simple cubic network formed by nanoparticles (NaCl/SC). In figure 8.7a we plot a simulation snapshot of the centers of mass of the micelles formed by the tethers that order into a NaCl lattice for D=2.5σ, θ=60°, and 1/T*=0.8. Note, centers of mass were calculated using the procedure outlined in section 4.2. We can see that the structure clearly demonstrates alternating chemical specificity. Figure 8.7b shows the bond order diagram (BOD) for the centers of mass of the micelles, where we ignore chemical specificity of the micelles and simply calculate the BOD for nearest neighbor micelles; for more information on the BOD, see section 4.3. The resulting BOD shows a simple cubic arrangement of the micelles, which corresponds to the BOD of a perfect NaCl system, shown as lines in 8.7b. Figure 8.7c shows the BOD for a perfect CsCl structure (often observed in triblock copolymers, as discussed later); it is clear that we have formed NaCl rather than CsCl.

In this phase the nanoparticles fill the space between the micelles, aggregating at the interstitials and arranging into a simple cubic network; an isosurface of the nanoparticles is shown in figure 8.7d. The nodes of the simple cubic structure each have six connections points; a single node is shown in figure 8.7e. The highest density of nanoparticles (i.e. the node) resides in the center of an eight-particle NaCl unit cell, as shown in 8.7e – this high density location corresponds to the placement of the central particle in a BCC lattice. We utilized the same procedure to approximate the location of the nodes as we used to calculate center of mass of the spherical micelles (see section 4.2). Figure 8.7f shows an eight-particle unit cell of NaCl extracted from our system with the locations of the nanoparticle nodes rendered as gray spheres. The overall phase corresponds to the $AlCu_2Mn$ structure, also known as the Heusler (L_21) phase (170). The $AlCu_2Mn$ structure is a three-component analog of BCC (CsCl is the two-component analog to BCC).

8.2.9 Zincblende ordered spherical micelles/nanosphere diamond network (ZnS/D)

For D=2.5σ we find a binary mixture of spherical micelles ordered into a zincblende (binary diamond) lattice of tethers with a complementary diamond network formed by the nanospheres (ZnS/D). In figure 8.8a, we show a simulation snapshot of the centers of mass of the micelles formed by the tethers in the zincblende structure. This structure is the two-component analog of the diamond lattice (170). Figures 8.8b-d show the BODs of the

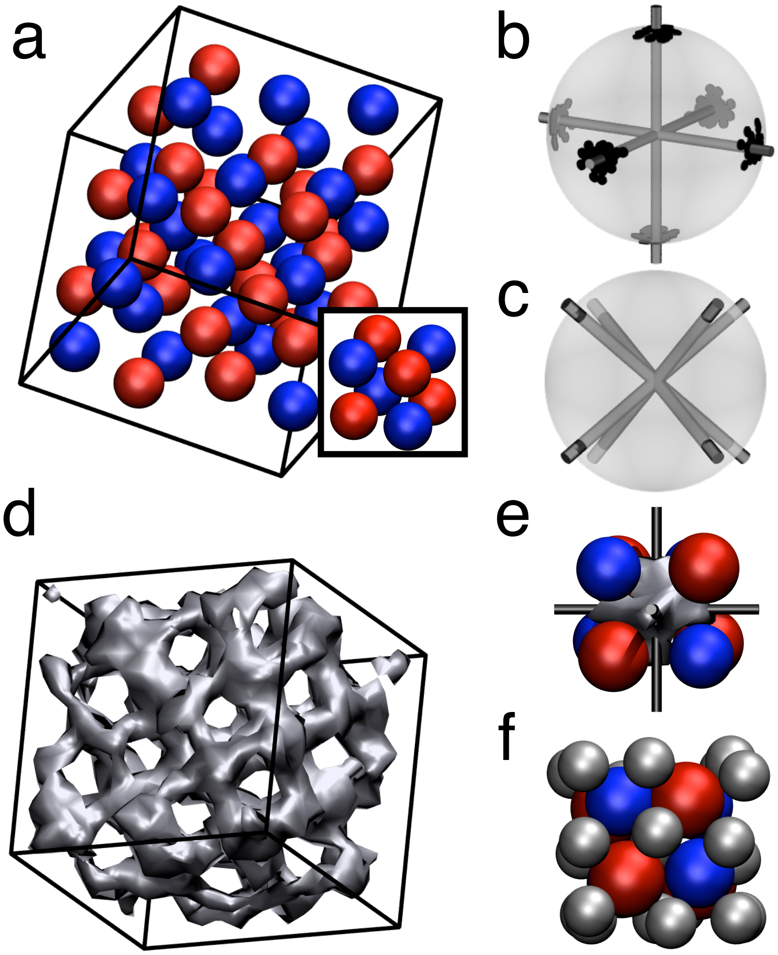

Figure 8.7 **(a)** Centers of mass of the NaCl ordered micelles formed by the tethers; the unit cell size is approximately 6.5σ. A perfect NaCl unit cell is inset. **(b)** BOD of the micelles center of mass; the BOD of a perfect NaCl structure is shown as lines. **(c)** BOD of a perfect CsCl structure for comparison. **(d)** Isosurface of the nanoparticles showing a simple cubic network arrangement. **(e)** Eight particle unit cell of NaCl formed by the micelles in the system, with the node of the nanoparticles network at the interstitial shown as an isosurface. **(f)** 8 particle unit cell of NaCl formed by the micelles in the system with the nodes of the nanoparticle network drawn as gray spheres showing the $AlCu_2Mn$ structure. All data for D=2.5σ, $\theta = 60^\circ$ and 1/T*=0.8. Reproduced from reference (71).

micelles centers of mass for the zincblende structure. We split the BOD into two separate diagrams, since the diamond phase possesses two bond configurations that are 60° rotations of each other. We plotted clusters where a “blue” particle (i.e. micelle formed by the A portion) is at the center surrounded by “red” particles (i.e. micelles formed by the C portion), and a second diagram where clusters have a “red” particle at the center surrounded by “blue” particles; these cluster definitions properly group the data by orientation of the tetrahedrons.

Both BODs in figure 8.8b and c show clear tetrahedral arrangements; the BODs for an ideal zincblende structure are plotted as lines in both plots, and agree with our simulation results. The blue centered and red centered tetrahedrons have complementary orientations (i.e. rotations of 60°), as shown in figure 8.8d.

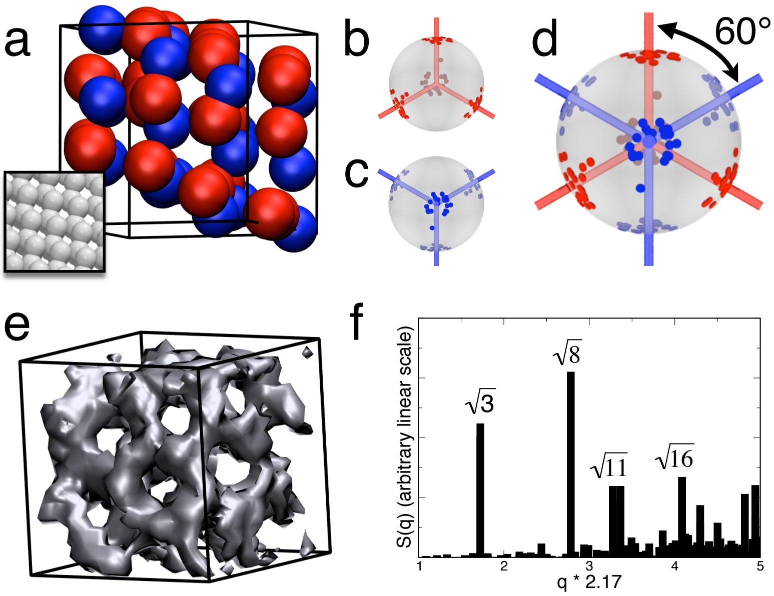

Figure 8.8 **(a)** Centers of mass of the micelles formed by tethers that order into the ZnS lattice showing 27 unit cells with a unit cell size of approximately 8σ. A perfect diamond lattice is shown in the inset. **(b-c)** BOD for nearest neighbors in the ZnS structure for the two different tetrahedral arrangements. **(d)** The combination of figures (b) and (c). **(e)** Diamond network formed by the nanoparticles in the Zns/D phase. **(f)** Diamond network formed by the nanoparticles in the Zns/D phase. **(f)** Average S(q) for the nanoparticle network, showing strong peaks with ratios $\sqrt{3} : \sqrt{8} : \sqrt{11} : \sqrt{16}$. Note that q was scaled such that the first peak corresponds to $\sqrt{3}$ for ease of viewing. All DTNS data at D=2.5σ, $\theta = 30°$ and 1/T* = 0.8. Reproduced from reference (71).

Within this phase, the nanoparticles organize into a diamond network that is woven into the micellar lattice. An isosurface of the nanoparticle diamond network structure is shown in figure 8.8e. In figure 8.8f we plot S(q) for the nanoparticles, finding strong peaks at ratios $\sqrt{3} : \sqrt{8} : \sqrt{11} : \sqrt{16}$ as expected for diamond (171); note that q was scaled such that the first peak corresponds to $\sqrt{3}$ for ease of viewing. The overall ZnS/D phase is composed of two interwoven diamond structures where one network is formed by nanoparticles and the other consists of a binary lattice of spherical micelles.

8.2.10 Discussion

We can obtain insight into the observed DTNS phases by comparing with what is known about triblock copolymers. The DTNS system can be loosely thought of as a nanoparticle equivalent of an ABC triblock copolymer where, in this case, the center block of a triblock has been replaced by a nanosphere. For example, as we decrease θ between the two tethers in the D=2.5σ DTNS system, we see a change from alternating diamond to alternating tetragonal cylinders to spherical micelle phases, as shown in figure 8.2. In linear triblock copolymers, as the length of the middle block (B block) is decreased, we typically see a change from a tricontinuous structure (e.g. the alternating gyroid (27) or alternating diamond phase (28; 29; 30)) to alternating tetragonal cylinders (27; 30) to CsCl structured micelles (27; 30). In both cases, the net effect is that the A and C blocks are brought closer together, constraining the possible tether configurations and resulting in a phase transition. In a rough sense, the overall progression of phases is similar whether we change the angle between tethers or, in linear triblocks, decrease the length of the middle block.

The overall phase behavior as a function of nanosphere diameter can be better understood by constructing a plot of D verses θ for a fixed 1/T* (similar to F_v verses ϕ constructed for mono-tethered nanospheres in section 5.1.3). In figure 8.9 we present the phase behavior for 1/T* = 0.8. We see that spherical micelle phases are only stable in regions where tethers are close together (i.e. small θ) and nanosphere diameter is large. Conversely, lamellar phases are stable in regions where tethers are well spaced (i.e. large θ) and nanosphere diameter is small. This diagram also demonstrates the strong dependence many of the phases have on nanosphere diameter; alternating tetragonally ordered cylinders appear to have the largest range of stability.

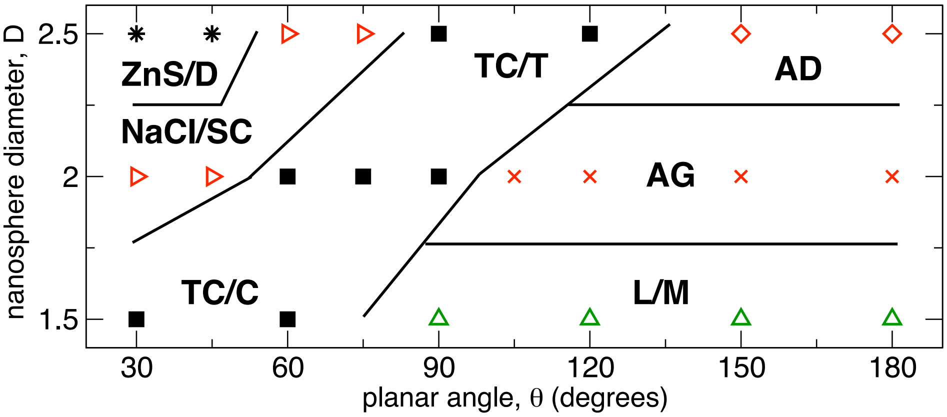

Figure 8.9 Phase diagram for D verses θ at 1/T* = 0.8, created from the data presented in figure 8.2. Phase boundaries are approximate and drawn to guide the eye. Reproduced from reference (86).

The lamella, alternating diamond, alternating gyroid, and tetragonal cylinder phases are all well known in the linear triblock copolymer literature and their formation in the DTNS system is not entirely surprising; in these cases, the DTNS behave very similar to linear triblocks and the geometry of the nanoparticle appears to have little impact on the resulting structure. However, as we noted earlier, linear triblock copolymers have been shown to form CsCl ordered spherical micelles rather than the NaCl ordered micelles we find for DTNS. Furthermore, it has been calculated that for linear triblock copolymers CsCl has a lower free energy than NaCl (172), thus, we would expect that DTNS might also form the CsCl structure. In previous work (66), we found that under selective solvent conditions, mono-tethered nanospheres could be roughly mapped to surfactants and block copolymers by considering the ratio of the excluded volume of head to tail, F_v (66) (see section 5.1.3), however, even when a nanosphere and polymer chain have the same excluded volume, there can be important, subtle differences. A nanosphere has fewer configurational degrees of freedom than an equivalent polymer with the same excluded volume; the radius and effective volume (i.e. shape or mass distribution) of the nanosphere are constant, whereas the radius of gyration and effective volume of a flexible polymer can vary based on solvent conditions, temperature and volume fraction. As a result, the flexible middle block in a triblock copolymer may reduce the correlation between the A and C blocks, e.g. by bending or stretching, allowing the A and C blocks a larger configuration space. In the DTNS system, we remove many of the degrees of freedom of the middle block by replacing it with a nanosphere that has a fixed volume/geometric contribution and by including a bond angle constraint, both of which limit the configurational entropy of the A and C tethers. As such, it is reasonable to conclude that for the DTNS system, these changes may result in a different favorable configuration of the individual blocks, thus changing the overall global structure, in this case stabilizing the NaCl structure over CsCl.

The effect of architecture of the DTNS (via the planar angle) is clear when we examine the transition from NaCl/SC to the ZnS/D for D=2.5σ. As the spacing between the first beads of the two tethers approaches $\sim 1\sigma$, the tethers are essentially connected to the same location on the nanosphere, increasing the prominence of the nanosphere and making it less linear with respect to the tethers; in this limit the DTNS more closely resembles a star triblock copolymer with one collapsed block, as sketched in figures 8.10a-b. This change in architecture brings the tethers closer together which in turn brings the micelles closer together; the average distance between the centers of mass of the micelles in the NaCl configuration is $6.61\sigma \pm 0.57$ for θ = 60° and 1/T* = 0.8, while in the zincblende configuration the distance is $5.86\sigma \pm 0.91$ for θ = 30° and 1/T* = 0.8 (note: both data sets are Gaussian and the size of the micelles are equivalent between the two systems). By

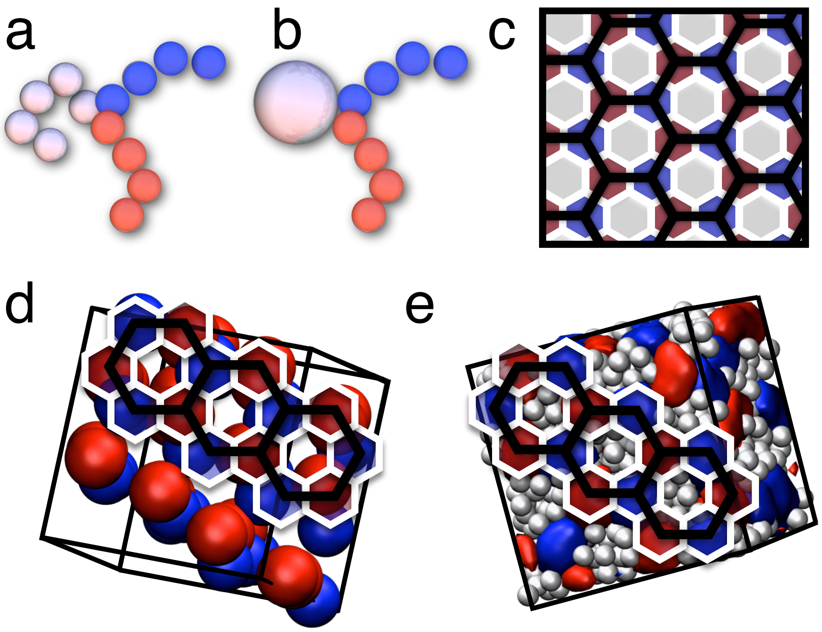

Figure 8.10 **(a)** Schematic of a star triblock copolymer. **(b)** Schematic of the DTNS building block at θ=30°. **(c)** Schematic of the [6,6,6] Archimedean tiling. A graphite structure is shown as the black hexagonal lattice. **(d)** Three equivalent graphite tiles are overlaid on the projection on the zincblende structure. **(e)** Reducing the size of the nanoparticle from D=2.5σ to 2.0σ results in the formation of the [6,6,6] columnar structure. Cylinders of tethers are shown as isosurfaces for clarity. Reproduced from reference (71).

bringing the micelles closer together we force a change in the aggregation behavior of the nanospheres, which can be observed not only be the change from a simple cubic network to diamond network, but also by the difference in nanoparticle coordination where cn = 6.86 ± 1.24 for NaCl/SC verses cn = 7.46 ± 1.37 for Zns/D. Star triblock copolymers alone are not known to form the ZnS/D structure, but are known to exhibit a columnar phase described by the [6,6,6] Archimedean tiling (31). In the [6,6,6] phase, all three blocks form cylinders that are arranged in an alternating hexagonal pattern (31), as shown in figure 8.10c. If we only consider two of the three types of hexagons (e.g. red and blue), essentially excluding the portion that would correspond to the nanoparticles in our system, we find a binary arrangement of hexagons in six-member rings that closely resemble the structure of graphite. This [6,6,6] structure is nearly identical to the 2-d projection of the ZnS/D structure, as shown in figure 8.10d where three "graphite" hexagons are highlighted. In other words, the ZnS/D structure formed by the spherical micelles is essentially the 3-d micellar equivalent of the columnar [6,6,6] phase. Just as in the NaCl/SC phase, the geometry and volume contribution of the nanoparticle seems to be important in stabilizing the ZnS/D structure over the typically observed triblock copolymer phase; the bulky geometry of the nanoparticle helps to induce curvature, stabilizing spherical rather than cylindrical micelles. If we decrease the diameter of the nanoparticle from D=2.5σ to 2.0σ, we reduce the ability of the nanoparticle to induce curvature. We simulated a system with D=2.0σ at θ = 30° finding the [6,6,6] columnar phase, as shown in figure 8.10e rather than ZnS/D. If the length of the B block for a star triblock copolymer in the [6,6,6] phase were increased, similar to changing the nanosphere diameter from D=2.0σ to 2.5σ, the system has been shown to form the [8,6,4;8,6,6] columnar phase (31), not ZnS/D. Recently, ZnS ordered spherical micelles were reported for a system composed of a mixture of ABC star triblock copolymers and B homopolymers (33). The addition of the B homopolymer acts to increase the bulk of the B block in the star triblock rather than just the length. This is directly analogous to the impact of the geometry of the spherical nanoparticle and clearly highlights its importance; it is not only the volume of the nanoparticle that is important but also the distribution of volume (i.e. the shape). We should note that the [6,6,6] phase at D=2.0σ and θ = 30° does not appear to be the stable structure and was only reproducible for a single box size; simulations of larger systems resulted in the NaCl/SC phase, as reported in figure 8.2b.

8.3 Phase behavior as a function of block fraction and immiscibility

In this section we explore the phase behavior of di-tethered nanospheres under melt-like conditions as a function of immiscibility (via interaction strength) and block fraction. Nanospheres are modeled as spheres of diameter D=2.0σ connected to two chemically distinct tethers, where each bead in the tether has a diameter σ. The angle between the tethers, θ, is fixed at 180° by the use of a harmonic spring with k = 30 and $R_0 = (D+\sigma)sin(\theta/2)$ (see section 3.1 for more details). A schematic of the building block is shown in figure 8.1d. We fix the total number of polymer beads at eight and vary their distribution between the two tethers (i.e. block fraction). We explore systems where the ratio of lengths of the A to C tethers is 4:4, 5:3, 6:2 7:1, and 8:0. In this study, we span a block fraction range that starts with a symmetric system (i.e. 4:4) that is identical to the θ=180° in the D=2.0σ phase diagram presented in figure 8.2 to the limit of a mono-tethered nanosphere (i.e. 8:0), comparable to the upper limit of ϕ investigated in section 5.1.

We find three phases as a function of block fraction, summarized in figure 8.11. For block fractions of 4:4 and 5:3 we find the alternating gyroid (AG), shown in figure 8.5a. The AG phase is constructed of two chemically distinct gyroid networks, one formed by the A tether the other formed by the C tether, embedded in a matrix of nanospheres. The AG phase

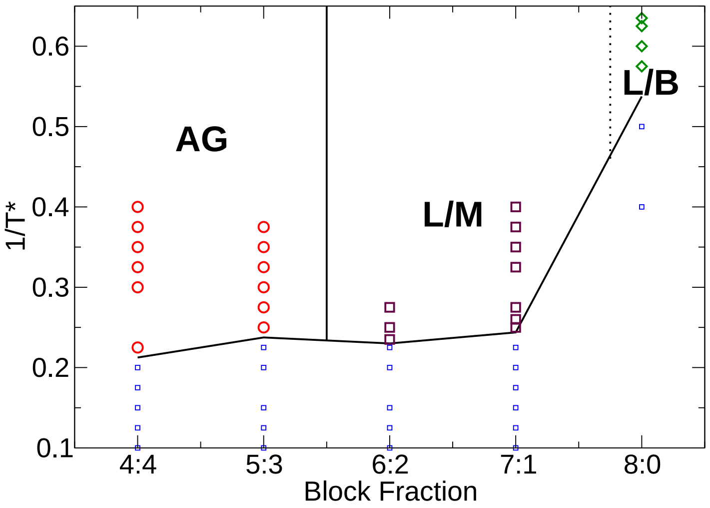

Figure 8.11 Phase diagram as a function of 1/T* and block fraction for nanosphere diameter D=2.0σ. With increasing asymmetry in block fraction we find: the alternating gyroid structure formed by the tethers in matrix of nanospheres (AG); lamellar sheets where the nanospheres form a monolayer (L/M); and lamellar sheets where the nanospheres form a bilayer (L/B). Phase boundaries are approximate and drawn to help guide the eye. Reproduced from reference (86).

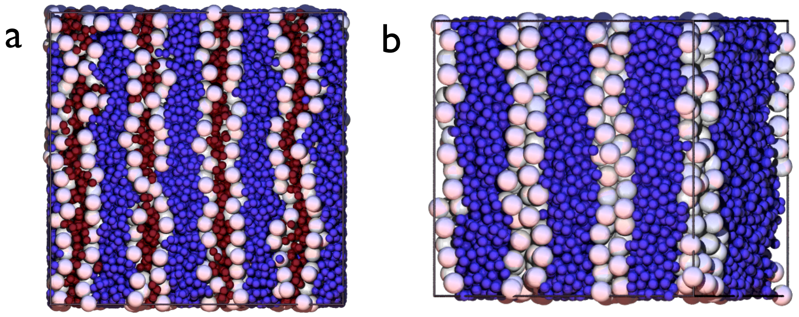

Figure 8.12 **(a)** Simulation snapshot of lamellar sheets where nanospheres form a monolayer (L/M) for a block fraction ratio of 6:2. **(b)** Simulation snapshot of a lamellar sheets where nanospheres form a bilayer (L/B) for a block fraction ratio of 8:0 (i.e. a mono-tethered nanosphere). Reproduced from reference (86).

was previously shown in figure 8.5 and discussed in section 8.2.6. For block fractions of 6:2 and 7:1 we find lamellar sheets where the nanospheres organize into a monolayer (L/M), as shown in figure 8.12a. In the limit of a mono-tethered nanosphere (i.e. block fraction 8:0), we find lamellar sheets where the nanospheres organize into a bilayer, shown in figure 8.12b. The formation of a bilayer structure is consistent with the high density phase behavior seen in chapter 5 for mono-tethered nanospheres under selective solvent conditions.

8.3.1 Discussion

As the block fraction becomes more asymmetric (i.e. 4:4 to 8:0), we see a transition from the AG phase to lamellar phases. Typically for diblock copolymers under melt conditions, the trends is the opposite; symmetric block fractions result in lamella where as asymmetric systems result in structures with curved interfaces, such as the double gyroid (25). Here, the presence of the nanosphere adds an additional volumetric constraint not found in diblock copolymers. As the length of the A-block increases, it can better balance the volumetric contribution of the nanospheres. In the limit of a mono-tethered nanospheres (i.e. 8 tether beads, ratio of 8:0), the ratio of the volume of the nanosphere to the A tether, $F_v = 1.0$, hence the two blocks are completely balanced (i.e. symmetric, see section 5.1.2 for more details). The nanosphere volume and how it relates to tether voume adds additional parameters that must be considered when predicting the phase behavior of di-tethered nanospheres

8.4 Summary

Our results show that the structural phase behavior of di-tethered nanospheres is a function of the directionality and strength of the tether-tether interactions in addition to the nanosphere diameter. We have shown that DTNS can produce unique structural arrangements of both tethers and nanoparticles and that these arrangements are controlled by the geometry of the nanoparticle and location of the attached tethers. We have demonstrated a novel route to form diamond and SC networks of nanoparticles, two structures highly sought for photonics applications (112). Overall, we have shown that the use of soft-matter tethers with directionality can be used to produce highly ordered periodic structures that would not necessarily be expected of either equivalent flexible polymer systems or pure nanoparticle systems in the absence of tethers.

Chapter 9

Conclusions and future directions

9.1 Contributions

This dissertation has focused on exploring the phase behavior of mesoscale models of tethered shape amphiphiles using computer simulation. Morphological phase diagrams of mono-tethered and di-tethered nanospheres were constructed with the goal of understanding to what extent tethered nanoparticles behave like equivalent flexible amphiphiles. These phase diagrams were meant to provide insight into how parameters such as volume fraction, nanosphere diameter, solvent selectivity, and building block architecture influence the self-assembled morphologies. The approach was to utilize minimal models that capture shared features of tethered nanoparticles and yield information that can be universally applied. These phase diagrams are meant to give experimentalists insight into the nature of the phase behavior, as well as to highlight the key parameters that must be controlled for the fabrication of specific structures.

In our studies of mono-tethered nanospheres where the solvent is good for the nanospheres, the phase diagrams and trends are qualitatively similar to those of equivalent flexible amphiphiles (e.g. surfactants and block copolymers). We find a variety of phases including micelles, cylinders, perforated lamellae, and lamellae, as would be expected for surfactants and block copolymers (23; 25). These results are not entirely surprising as the tethered nanosphere building block architecture closely resembles the architecture of a surfactant or block copolymer. Moreover, we found that by calculating the ratio of excluded volumes, F_v, there is quantitative agreement between the phase behavior of surfactants and tethered nanospheres. These phase diagrams are currently being utilized to guide and explain the formation of structures by experimentally realized mono-tethered nanospheres (173).

These studies have also yielded one of the first predictions of an entropically stabilized quasicrystalline approximate structure as well as a simple model to describe the formation. This model not only elucidates the origin of the quasicrystalline behavior of the tethered nanospheres system, but also experimentally observed quasicrystalline behavior of dendrimers (139; 147). Our results and model may provide experimentalists with a unique method to self-assemble quasicrystals on the nanometer length scale.

Our subsequent studies of mono-tethered nanospheres where the nanospheres are in poor solvent, have also yielded a phase diagram that is qualitatively similar to those of equivalent flexible amphiphiles. However, unlike flexible amphiphiles, tethered nanospheres adopt distinct local packings due to the hard particle shape. Within the cylinder, double gyroid, and perforated lamella phases, nanospheres adopt icosahedral packings, and within the lamellae phase nanospheres adopt hexagonally close packed structures. We proposed that this icosahedral ordering is important to reducing the packing frustration within the nodes of the double gyroid structure, making it potentially more stable than an equivalent flexible system. Additional studies of the double gyroid structures formed by tethered nanorods yielded similar results; the formation of hexagonal bundles of rods reduced packing frustration in the double gyroid phase, highlighting the importance of the nanoparticle geometry. The formation of the tethered nanorod double gyroid structure also provides insight into the local structure of double gyroids formed experimentally by rod-coil block copolymers, as this local ordering cannot be easily observed in experiment (127).

We also proposed that the icosahedral ordering of the nanospheres was a result of the 2D confinement that occurs during the microphase separation. We confirmed this by confining nanospheres within cylindrical pores of varied diameter, finding a crossover between crystalline and icosahedral ordering as the diameter of the pore was decreased. This may provide experimentalists with a novel route to create icosahedral assemblies of nanoparticles.

Our studies of di-tethered nanospheres under melt-like conditions have yielded phase behavior that shares characteristics with equivalent flexible amphiphiles but with several unique changes. We found phases such as lamellae, the alternating gyroid, alternating double diamond, and tetragonally ordered cylinders which are all known for triblock copolymers (120). We additionally found the formation of NaCl ordered micelles of tethers with a complementary simple cubic network of nanoparticles and zinc blende (binary diamond) ordered micelles of tethers with a complementary diamond network of nanoparticles. These phases are unique and not previously reported for pure triblock copolymer systems. We showed that the formation of these two micelle structures is a direct result of the shape of the nanosphere; the nanosphere is able to induce a larger decrease of curvature than a flexible polymer block. Our predictions of the zinc blende structure bolster experimental observations of the zinc blende phase in blends of homopolymers and star triblock copolymers (33), where the addition of homopolymer acts to increase the bulk, rather than length, of one of the blocks, similar to what the shape of the nanosphere. Our simulations provide a novel route to form highly complex crystalline structures at the nanometer scale, such as diamond and simple cubic, that are highly sought for photonics applications (112).

Our studies of icosahedrally ordered nanospheres spurred the development of the R$_{ylm}$ method for detecting local structure, which is currently being developed as part of a free, open source shape matching code to be distributed by the Glotzer group under the Glotzilla pacakage. In conjunction with the shape matching code, we have developed a highly optimized and flexible image processing code, based on the algorithms of Crocker and Grier (88), that we utilized to detect the the centers of mass of micellar structures formed by mono- and di-tethered nanospheres. Both codes will be distributed freely to the community as part of Glotzilla.

While we have observed a rich phase behavior in our studies of tethered nanoparticles, we should note that our simulations suffer from several shortcomings as a result of the simplifications utilized in our models. First, we do not explicitly include solvent particles, but rather implicitly include solvent effects (i.e. random bombardment and viscosity via the Brownian dynamics method). We do not account for the volume occupied by the solvent molecules, which may become important if the size of the solvent molecules is on the order of the polymer tether or if any strong interactions occur between solvent and our building blocks. Additionally, our simulations treat nanospheres as monodisperse with respect to diameter; typical synthesis methods yield nanospheres with polydispersity on the order of 10% (47). Polydispersity may have a strong impact on the ability of nanospheres to local order, potentially impacting the overall bulk structure. Also, our models use the 12-6 Lennard-Jones potential (LJ) to model attractive interactions. The range and diameter of the attractive well is fixed for all simulations and our models do not incorporate the impact of the shape of the potential or account for longer range interactions that may exist in real systems. We discuss future studies of these simplifications below.

9.2 Future directions

The work presented in this dissertation provides a foundation for future studies. We have explored the phase behavior of several simplified models of tethered nanospheres. Assessing the impact of these simplifications is of great interest, specifically exploring the role of polydispersity and the impact of interaction range and shape. Additionally, the work in this dissertation has presented a new route for the creation of quasicrystalline materials; further investigations into this quasicrystal forming model are also proposed.

9.2.1 Polydispersity of nanospheres

In our studies of mono-tethered nanospheres where the solvent was poor for the nanospheres, we found distinct icosahedral ordering between the nanospheres (see section 5.2 for more details). We argued that the formation of the icosahedral clusters was important to the overall stability of the double gyroid structure. These results correspond to a system where the nanospheres are monodisperse with respect to particle diameter (i.e. all the same diameter). However, in practice, it is not uncommon for nanospheres to have polydispersity levels of between 5 and 20%. The connection between local and bulk ordering makes understanding the impact of polydispersity very important to assessing the experimental feasibility of the structures we have predicted. For example, a small amount of polydispersity may actually act to augment icosahedral ordering and increase the density of the local clusters, resulting in an increased range of stability for the double gyroid structures. A high amount of polydispersity may lead to a destabilization of icosahedral ordering, resulting in a change in phase behavior.

We also found hcp ordering between the nanospheres in the lamellar phase. It has been predicted that large amounts of polydispersity will prevent crystallization, which in this case may alter the ordering of the nanospheres, potentially changing the phase behavior.

9.2.2 Interaction range and shape

Within this thesis, interactions have been treated with the standard 12-6 Lennard-Jones (LJ) potential truncated at 2.5σ. As such the attraction between our nanoparticles has been essentially limited to only first neighbor interactions (the diameter of our nanospheres was varied between 1.5σ and 2.5σ). Since our ultimate goal is to use tethered particles as a means for assembling specific structures, understanding how these structures might be perturbed by interaction range is paramount; we cannot guarantee that nanoparticles will only interact with nearest neighbors. In particular, longer-range interactions may result in increased long range ordering between nanoparticles, since nanoparticles would now interact well beyond their first and second neighbor shells.

Interparticle interactions between nanoparticles are not well understood, however, predictions of the VDW interaction in vacuum between nanoparticles has been shown to exhibit a functional form similar to the LJ potential (49). It has additionally been hypothesized that the interaction range of many nanoparticles is of the order of 3 to 10 nanoparticle diameters for nanoparticles in the 1-10 nm range (47). The standard 12-6 LJ potential we have thus far utilized decays to zero at approximately 2.5 particle diameters, thus it fits with the estimated lower range of nanoparticle interaction. To understand the impact of interaction range, one could utilize different functional forms of the traditional LJ potential, as applied to the nanoparticles. For example, the 12-2.5 LJ potential decays to zero at approximately 10σ (shown in Fig 9.1).

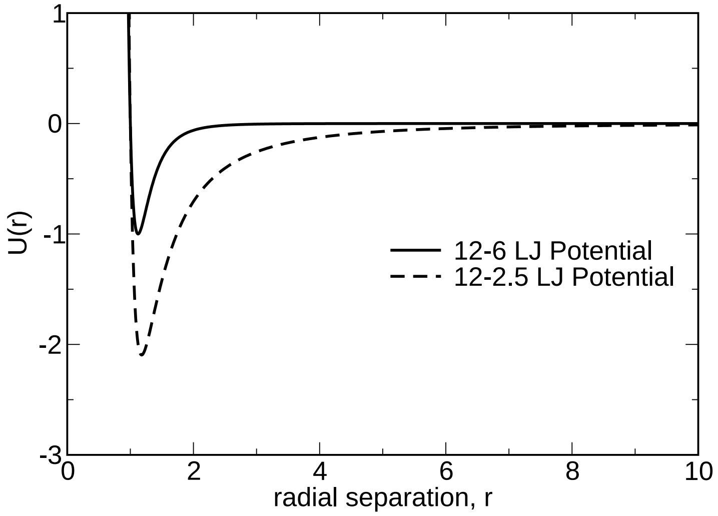

Figure 9.1 Attractive portions of the LJ potential with exponents 6 and 2.5.

Just as important as considering the range and shape of the attractive potential is considering the range of repulsion. In several of our studies we treated nanospheres with the Weeks-Chandler-Andersen potential. The WCA potential primarily accounts for excluded volume exhibiting a very short-ranged repulsion. Exploring the impact on phase behavior as a function of the range of repulsion is important to understanding the phase behavior trends. The inclusion of a long range repulsion may increase the effective volume of the nanospheres, causing a shift towards structures with a high degree of curvature (20). This may also result in an increase in the ordering between nanospheres, as was previously seen in chapter 5.

It is important to note that the inclusion of longer-range forces vastly increases the number of force calculations needed in the simulation, which dramatically increases the amount of cpu time needed. Such simulations would have been computationally unfeasible for large systems only a short time ago. However, recent advances in GPU technology have resulted in an unprecedented increase in computational power, making such studies now feasible with codes such as HOOMD (174).

9.2.3 Entropy stabilized quasicrystals

In chapter 7 we demonstrated the formation of a dodecagonal quasicrystal approximate formed by the micelles of tethered nanospheres. We also proposed a simplified model of the micelles to better understand the key parameters in the formation of the quasicrystal approximate. Our model was essentially an entropic model, where particle-particle interactions captured only excluded volume. Physical systems of colloids are likely to have electrostatic interactions. The range of these electrostatic interactions are often tunable by changing properties of the solvent (e.g. salt concentration) (21; 20). Exploring the impact of electrostatic interactions on the formation of the quasicrystal, and stability of, is an important step to making this model more physically realistic and useful to experimentalists.

Additionally, we are interested in tuning the model parameters (e.g. surface coverage, size ratio, spring constant, interaction range) to produce an optimal quasicrystal forming system. Such optimization will require the application (143) and/or development of new order parameters (90) for quasicrystals as well as a smart methodology to explore the phase space. Developing a "learning algorithm" to generate parameter sets may be an effective method to solve this type of optimization problem.

9.3 Outlook

This thesis has focused on exploring the phase behavior of model tethered nanospheres. We have discovered a rich and complex phase behavior, yet many important questions still need to be answered. In this chapter, I outlined only a few of the many important questions that can be addressed in future studies. I feel the future studies I selected are fundamental to the ongoing development within the nanoscience community. It is my hope that as a result of the many recent advances in computational tools and hardware, simulation will continue to grow in importance within the nanoscience community and provide a deeper understanding of the nature of these nanomaterials.

Appendices

Appendix A

Space Groups

Throughout this dissertation, we encountered many morphologies formed by tethered nanospheres. Knowing the space group of these systems is important for predicting the characteristic ratios expected from the structure factor (discussed in appendix B). Here we summarize the space group symmetries of some of the basic structures we encounter.

double gyroid (DG) (27): $Ia\bar{3}d$

double diamond (DD) (27): $Pn\bar{3}m$

sigma phase (170): $P4_2/mnm$

body centered cubic (BCC) (170): $Im\bar{3}m$

simple cubic (SC) (170): $Pm\bar{3}m$

face centered cubic (FCC) (170): $Fm\bar{3}m$

diamond (D) (170): $Fd\bar{3}m$

We should note that if we ignore chemical specificity, phases such as the double gyroid and alternating gyroid become equivalent. These equivalent phases we observed include:

alternating gyroid (AG) = double gyroid (DG)

alternating diamond (AD) = double diamond (DD)

sodium chloride (NaCl) = simple cubic (SC)

Heusler $L2_1$ ($AlCu_2Mn$) = body centered cubic (BCC)

cesium chloride (CsCl) = body centered cubic (BCC)

zincblende (ZnS) = diamond (D)

Appendix B

Standard analysis methods

Untraditional analysis methods used throughout this thesis, such as the R$_{ylm}$ method, micelle center of mass calculation, and bond order diagram, are described in chapter 4. In this appendix we describe the structure factor, S(q), and radial distribution function, g(r), which are both traditionally, commonly used

B.1 The structure factor

The structure factor is a mathematical description of how a structure scatters incident radiation due the arrangement of its particles (171). S(q) produces a set of peaks whose ratio indicates the spacing of different planes within a structure and this characteristic ratio can then be used to identify specific structures (171). The structure factor of a set of particles is calculated following Schultz (169):

$$S(\vec{q}) = \frac{\left(\sum_j cos(\vec{q}\cdot\vec{r})\right)^2 + \left(\sum_j sin(\vec{q}\cdot\vec{r})\right)^2}{N} \tag{B.1}$$

where N is the number of particles, $\vec{r}$ is the spatial vector of the particles, and $\vec{q}$ is the wave vector. $\vec{q}$ is restricted to integer number of wavelengths within the simulation box,

$$\vec{q} = \left\langle \frac{n_x}{L_x}, \frac{n_y}{L_y}, \frac{n_z}{L_z} \right\rangle \tag{B.2}$$

where n_x, n_y, n_z are the integers in the x,y,z directions and L_x, L_y, L_z are the box lengths in the x,y,z directions, respectively. Typically, this is presented as $S(\vec{q})$ verses the magnitude of $\vec{q}$, q. The ratio of q values that show strong values of $S(\vec{q})$ are characteristic and used to identify the structures. For example, the characteristic ratio of q values for various structures we observe are as follows:

double gyroid (DG)/alternating gyroid(AG) (122): $\sqrt{3} : \sqrt{4} : \sqrt{10} : \sqrt{11}$

double diamond (DD)/alternating diamond (AD) (26): $\sqrt{2} : \sqrt{3} : \sqrt{4} : \sqrt{6}$

diamond (D) (171): $\sqrt{3} : \sqrt{8} : \sqrt{11} : \sqrt{16}$

Example plots of the structure factor can be found in figures 8.5d, 8.6d, and 8.8f for AG, AD, and D respectively.

The structure factor can also be used to calculate the periodic spacing (i.e. unit cell size) of a structure, $L_{spacing}$. The periodic spacing can be calculated via $L_{spacing} = (2\pi/q*)m$, where $q*$ is the modulus of the wave vector at which the first principal $S(\vec{q})$ maximum is located, and m is the first observed reflection spacing for the structure(122; 116); for example, m = 1 for a lamellar structure, and $m = \sqrt{6}$ for a gyroid structure (122; 116).

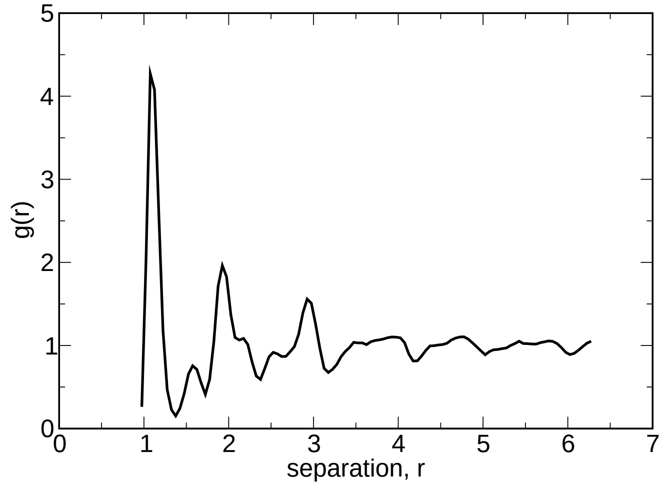

Figure B.1 Radial distribution function, g(r), of a Lennard-Jones system of 2000 particles at T*=0.5 and ϕ = 0.52.

B.2 The radial distribution function

This text was adapted from the Radial Distribution Function wiki entry I contributed to the MatDL SoftMatter Wiki http://matdl.org/matdlwiki/.

The radial distribution function, also known as g(r) or the pair correlation function, is a measure used to determine the correlation between particles within a system. g(r) is an average measure of the probability of finding a particle at a distance of *r* away from a given reference particle, relative to an ideal gas at the same density.

g(r) is constructed by calculating the distance between all particle pairs in the system and binning them into a histogram. The histogram is then normalized with respect to an ideal gas, where particle histograms are completely uncorrelated. For three dimensions, this normalization is the number density of the system multiplied by the volume of the spherical shell, which mathematically can be expressed as $\mathrm{N}_{i.g.}(r) = 4\pi r^2 \rho \delta r$, where ρ is the number density.

Typically we use g(r) to determine the average distance between nearest neighbors in our calculation of R_{ylm} and the BOD. We also use g(r) to determine if long range ordering is present. Figure B.1 shows an example system in an FCC crystal with long range ordering; for R_{ylm} and the BOD we would utilize a cutoff of approximately 1.3 for this system.

Appendix C

Codes

The work contained in this thesis utilized the LAMMPS simulation package (C++ version, May 2008) (144) http://lammps.sandia.gov/ and an in-house Glotzer group code. The Glotzer group code was annotated in Appendix A of the Ph.D. thesis of Dr. Mark A. Horsch (175). In this appendix, key analysis codes developed as part of this thesis are presented.

C.1 R_{ylm} code

The R_{ylm} method (67; 68) is contained within the shape matching library under development within the Glotzer group. The source code will be made available through the MatForge development site (http://matforge.org/glotzer) as part of Glotzilla. The key routines for calculating the R_{ylm} method are summarized below.

C.1.1 Fourier coefficients

The following routine calculates the Fourier coefficients. The Fourier coefficient is used to calculate q and w.

x An array of coordinates that we will calculate the Fourier coefficient from.

l The frequency of the coefficient.

sd An array of complex numbers representing the computed Fourier coefficient shape descriptor.

```
void sd_fourier_coefficient_3d(std::vector<double*>& x, int l,
    std::vector< std::complex<double> >& sd)
{
    assert(l>=0);
    sd.resize(2*l+1);
```

```
/*init to zero*/
for(unsigned int i=0; i<sd.size(); i++) {
  sd[i] = (std::complex<double>) (0.0);
}

int n = x.size();
/*if there are no particles, exit*/
if (n==0) {
  return;
}
int n_used = n;
/*remove any particle that is located at the origin*/
for (int i=0; i<n; i++) {
  if (fabs(x[i][0]) < 1e-5
     && fabs(x[i][1]) < 1e-5
     && fabs(x[i][2]) < 1e-5) {
    n_used--;
    continue;
  }
  //-- STEP 1: Convert to spherical coordinates --
  double r = sqrt(x[i][0]*x[i][0] +
                  x[i][1]*x[i][1] +
                  x[i][2]*x[i][2]);
  double theta, phi;

  if(x[i][0] ==0 ) {
    if(x[i][1]==0) {
      phi = 0.0;
    }
    else if(x[i][1] > 0 ) {
      phi = M_PI * 0.5;
    }
    else {
      phi = 3.0 * M_PI * 0.5;
    }
  }
  else {
    phi = atan( x[i][1]/x[i][0] );
    if( x[i][0] < 0.0 ) {
      phi += M_PI;
    }
    else if( x[i][1] < 0.0 ) {
      phi += 2.0 * M_PI;
```

```
            }
        }

        double cos_theta = x[i][2]/r;
        theta = acos(cos_theta);


        //-- STEP 2: compute Ylm(theta, phi) for each theta, phi --
        //Notes:
        //1) We compute Yl(m) and Yl(-m) concurrently within the same loop
        //   by using the symmetry of the ls
        //2) We don't really need to calculate factorials and then divide
        //   for the the Ylm function, since we really only need the ratio
        //   of factorials.  Thus, we use the ratio_of_two_factorial_terms
        //   temp variable which a) allows us again to move the calculation
        //   into a single loop for efficiency and b) solves the problem of
        //   roundoff error that occurs if we divide two huge factorials
        //   for large l

        double c, ratio_of_two_factorial_terms = 1.0;

        for (int m=0; m<=l; m++) {
            if (m > 0) {
                ratio_of_two_factorial_terms *= (l + m) * (l - m + 1);
            }
            c = sqrt((2.0*l+1.0) /(4.0*M_PI)/ratio_of_two_factorial_terms);
            c *= plgndr(l, m, cos_theta);
            std::complex <double> ylm(c * cos(m*phi), c * sin(m*phi));
            sd[m+l] += ylm;

            if (m > 0) {
                int sign = (int)(pow(-1.0 , (double)m));
                std::complex <double> ylminusm(
                    sign*c*cos(m*phi),
                    -1.0*sign*c*sin(m*phi));
                sd[-m+l] += ylminusm;
            }
        }
    }

    for(unsigned int i=0; i<sd.size(); i++) {
        sd[i] /= (double) n_used;
    }
```

```
}
```

C.1.2 Q_l and w_l Calculation

The following routines read in the result from the calculation of the Fourier coefficient, **sd**, to calculate Q_l and w_l.

sd 3d fourier transform descriptor we use to convert to Q_l and w_l.

```
double sd_fourier_q(std::vector< std::complex<double> >&sd)
{
   //|qlm|^2 = the projection of the harmonic descriptor onto itelsef
   double qlm_sq = sd_matching_metric_P(sd, sd);
   //normalize by 4pi/(2l+1) and take sqrt
   //the size of the sd vector is 2*l + 1;
   return sqrt(4.0*M_PI / (sd.size()) * qlm_sq );
}

double sd_fourier_w3j(std::vector< std::complex<double> >&sd)
{
   int l = (sd.size()-1) / 2;
   // minimum and maximum values of m2
   double m2min, m2max;
   double w3jl[2*l + 1];
   int errflag;
   std::complex<double> numerator;

   for (int m1=-l; m1<=l; m1++ ) {
      w3j(l, l, l, m1, m2min, m2max, w3jl, (2*l+1), errflag);
      if( errflag ) {
         std::cerr << " w3j: Error number " << errflag << std::endl;
         exit( 1 );
      }
      std::complex<double> temp;
      for (int m2 = int(m2min); m2<=int(m2max); m2++) {
         temp += sd[m2+l]*sd[l-m2-m1]*w3jl[m2-int(m2min)];
      }
      temp *= sd[m1+l];
      numerator += temp;
   }
   double wl = real(numerator);
   double denominator = 0.0;
```

```
    for (int m=-l; m<=l; m++) {
        denominator += real(sd[ m+l ])*real(sd[m+l]) +
            imag(sd[m+l])*imag(sd[m+l]);
    }
    if (denominator == 0.0) {
        wl = 0.0;
    }
    else {
        wl /= sqrt(denominator*denominator*denominator);
    }

    return wl;
}
```

C.1.3 R matching metric

The R$_{ylm}$ method relies on calculating the sum of the square differences, R. We construct shape descriptors (**sd1** and **sd2** below) by concatenating together the values of Q_l and w_l calculated above for l = 4,6,8,10, and 12.

sd1 Shape descriptor “fingerprint” of our reference structure.

sd2 Shape descriptor “fingerprint” of our test structure.

```
double sd_matching_metric_R(std::vector<double>& sd1,
    std::vector<double>& sd2)
{
    //make sure the two fingerprints we are comparing
    //are the same size
    assert(sd1.size() == sd2.size());

    double residual = 0.0;
    std::complex<double> diff_i;

    for (unsigned int i=0; i<sd1.size(); i++) {
        double diff_i = sd1[i]-sd2[i];
        residual += diff_i*diff_i;
    }

    return sqrt(residual);
}
```

C.2 Image processing code

The source code for the image processing algorithms used to identify the center of mass of spherical micelles is available for download from the MatForge development site (http://matforge.org/IPGZ). The key blocks of code are summarized below and adapted from the original algorithm developed in reference (88) and subsequent application to 3D systems in reference (89). This is a general purpose code useful for the identification of centers of mass of micelles but also centers of mass of colloidal particles from microscopy data.

C.2.1 Gaussian filter

We implement the 3-d Gaussian filter by breaking it into three 1-d filters for speed. This reduces the overall number of calculations and allows for better cache streaming.

rawData Class that stores unprocessed intensity data.

filteredData Class that stores processed intensity data.

filterWidth Radius of filter along the width dimension of the array. Filter processes from -filterWidth to +filterWidth for each pixel.

filterHeight Radius of filter along the height dimension of the array. Filter processes from -filterHeight to +filterHeight for each pixel.

filterDepth Radius of filter along the depth dimension of the array. Filter processes from -filterDepth to +filterDepth for each pixel.

```
void gaussianFilter3DfastPBC(PixelArray3D <float> *rawData,
                     PixelArray3D <float> *filteredData,
                     int filterWidth, int filterHeight,
                     int filterDepth)
{
   int bFilterWidth = 2*filterWidth + 1;
   int bFilterHeight = 2*filterHeight + 1;
   int bFilterDepth = 2*filterDepth + 1;

   float filter_volume = bFilterWidth*bFilterHeight*bFilterDepth;
   filteredData -> height = rawData -> height;
   filteredData -> width = rawData -> width;
   filteredData -> depth = rawData -> depth;
```

```
/*resize the output array*/
filteredData ->    resize(filteredData->width,
                   filteredData->height,
                   filteredData->depth);

int width = filteredData -> width;
int area = filteredData -> width * filteredData -> height;

float gauss_array_width[bFilterWidth];
float gauss_array_height[bFilterHeight];
float gauss_array_depth[bFilterDepth];

float l_n_sq = 1.0;
float invr_neg_four = -1.0/4.0;
float invr_l_n_sq = 1.0/l_n_sq;
float B_width = 0.0;
float B_height = 0.0;
float B_depth = 0.0;

float exp_term = invr_neg_four*invr_l_n_sq;
/*pre-calculate the filtering matrices*/
for (int i = 0; i < bFilterWidth; i++){
      int ll = i - filterWidth;
      gauss_array_width[i] = exp((ll*ll)*exp_term);
      B_width += gauss_array_width[i];

}
for (int j = 0; j < bFilterHeight; j++){
      int mm = j - filterHeight;
      gauss_array_height[j] = exp((mm*mm)*exp_term);
      B_height += gauss_array_height[j];

}
for (int k = 0; k < bFilterDepth; k++){
      int nn = k - filterDepth;
      gauss_array_depth[k] = exp((nn*nn)*exp_term);
      B_depth += gauss_array_depth[k];
}


int ii_t, jj_t, kk_t;
float f;
int r,s,t;
```

```
double count=0;
/*first filtering pass in the x-direction*/
for ( t = 0 ; t < rawData->depth; t++) {
   for (s = 0; s < rawData->height; s++) {
      for (r = 0; r < rawData->width; r++) {
         ii_t = r-filterWidth;
         f=0.0;
         for (int i = 0; i < bFilterWidth; i++) {
            if(ii_t+i < 0)
               ii_t += width;
            else if(ii_t+i >= width)
               ii_t -= width;
            int index = (ii_t+i) +(s)*width +(t)*area;
            f += gauss_array_width[i] * rawData->pixels[index];
            count++;
         }
         filteredData -> pixels[t*area + s*width+r] = f/B_width;
      }
   }
}
/*temporary array to hold filtered data*/
PixelArray3D <float> *temp = new PixelArray3D<float>();
temp -> resize(filteredData->width,
            filteredData->height,
            filteredData->depth);
/*second filtering pass in the y-direction*/
for ( t = 0 ; t < rawData->depth; t++) {
   for (s = 0; s < rawData->height; s++) {
      jj_t = s-filterHeight;
      for (r = 0; r < rawData->width; r++) {
         f=0.0;
         for (int j = 0; j < bFilterHeight; j++)   {
            if(jj_t+j < 0)
               jj_t += rawData->height;
            else if (jj_t+j >= rawData->height)
               jj_t -= rawData->height;
            int index = (r) +((jj_t+j)*width)+ t*area;
            f += gauss_array_height[j]*filteredData->pixels[index];
            count++;
         }
         temp -> pixels[t*area + s*width+r] = f/B_height;
      }
   }
```

```
    }
    /*third filtering pass in the z-direction*/
    for ( t = 0; t < rawData->depth; t++) {
        kk_t = t-filterDepth;
        for (s = 0; s < rawData->height; s++) {
            for (r = 0; r < rawData->width; r++) {
                f=0.0;
                for (int k = 0; k < bFilterDepth; k++){
                    if(kk_t+k < 0)
                        kk_t += rawData->depth;
                    else if(kk_t+k >= rawData->depth)
                        kk_t -= rawData->depth;
                    int index = (r) +(s)*width+ ((kk_t+k)*area);
                    f += gauss_array_depth[k]*temp->pixels[index];
                    count++;

                }
                filteredData -> pixels[t*area + s*width+r] = f/B_depth;
            }
        }
    }
    delete temp;
}
```

C.2.2 Local maximum

This function calculates the total number of particles centers by identifying the brightest pixels.

inIsMaxData Class instance that contains local maximum data.

outIsMaxData Class instance where filtered data will be saved.

inPosition Class instance that contains particle positions.

outPosition Class instance where filtered particle positions will be saved.

filterWidth Radius of filter along the width dimension of the array. Filter processes from -filterWidth to +filterWidth for each pixel.

filterHeight Radius of filter along the height dimension of the array. Filter processes from -filterHeight to +filterHeight for each pixel.

filterDepth Radius of filter along the depth dimension of the array. Filter processes from -filterDepth to +filterDepth for each pixel.

```
void localMaximum3D(PixelArray3D <float> *intensityData,
                    PixelArray3D <bool> *isMaxData,
                    ParticleArray *positionData,
                    int filterWidth, int filterHeight,
                    int filterDepth, float minimumThreshold)
{
  int r, s, t;
  float intensity=0;
  int candidateParticlesLocal =0;

  isMaxData -> resize(intensityData -> height,
                      intensityData -> width,
                      intensityData -> depth);
  int width = intensityData -> width;
  int area = (intensityData -> width)*(intensityData -> height);
  int volume = area * intensityData -> depth;
  bool isLocalMax = false;

  PixelArray3D <bool> *coarseGrain = new PixelArray3D<bool>();
  coarseGrain ->resize(intensityData -> width,
                       intensityData -> height,
                       intensityData -> depth);

  for(int i=0; i<volume; i++) {
    isMaxData -> pixels[i] = false;
    coarseGrain -> pixels[i] = false;
    if(intensityData -> pixels[i] > minimumThreshold)
      coarseGrain -> pixels[i] = true;
  }
  /*loop over the kernel surrounding each pixel*/
  int twoD =2*filterDepth;
  int twoH =2*filterWidth;
  int twoW =2*filterHeight;

  for(t=twoD; t<intensityData->depth-twoD; t++) {
    for(s=twoH; s<intensityData->height-twoW; s++) {
      for(r=twoW; r<intensityData->width-twoH; r++) {
        if(coarseGrain -> pixels[r+s*width+t*area]) {
          isLocalMax = true;
          intensity = intensityData -> pixels[r+s*width+t*area];
          for(int k = 0; k < 2*filterDepth+1; k++) {
```

```
               for(int i = 0; i < 2*filterHeight+1; i++) {
                  for(int j = 0; j < 2*filterWidth+1; j++) {
                     int kk = t-filterHeight+k;
                     int ii = s-filterHeight+i;
                     int jj = r-filterWidth+j;
                     int indexa = kk*area+ii*width+jj;
                     if(coarseGrain -> pixels[indexa])
                     {
                        int index = kk*area+ii*width+jj;
                        if(intensity<intensityData -> pixels[index]){
                           isLocalMax = false;
                           goto outside_of_loop;
                        }
                     }
                  }
               }
            }
            if(isLocalMax){
               isMaxData -> pixels[r+s*width+t*area] = true;
               candidateParticlesLocal++;
            }
         }
         outside_of_loop:
         10;
      }
   }
}
int np=0;
positionData -> resize(candidateParticlesLocal);
/*Identify the location of the brightest pixel*/
int D = filterDepth;
int H = filterHeight;
int W = filterWidth;
for(t = D; t < intensityData->depth-D; t++) {
   for(s = H; s < intensityData->height-H; s++) {
      for(r = W; r < intensityData->width-W; r++) {
         if(isMaxData -> pixels[r+s*width+t*area]) {
            positionData ->particle[np*8]= r;
            positionData ->particle[np*8+1]= s;
            positionData ->particle[np*8+2]= t;
            for(int i=3; i<8; i++)
               positionData ->particle[np*8+i]= 0;
            np++;
```

```
                }
            }
        }
    }
    positionData -> total = np;
}
```

Bibliography

[1] C. B. Murray, C. R. Kagan, and M. G. Bawendi, “Synthesis and characterization of monodisperse nanocrystals and close-packed nanocrystal assemblies,” *Annual Review of Materials Science*, vol. 30, pp. 545–610, 2000.

[2] B. D. Busbee, S. O. Obare, and C. J. Murphy, “An improved synthesis of high-aspect-ratio gold nanorods,” *Advanced Materials*, vol. 15, pp. 414+, MAR 4 2003.

[3] Y. G. Sun and Y. N. Xia, “Gold and silver nanoparticles: A class of chromophores with colors tunable in the range from 400 to 750 nm,” *Analyst*, vol. 128, no. 6, pp. 686–691, 2003.

[4] F. M. van der Kooij, K. Kassapidou, and H. N. W. Lekkerkerker, “Liquid crystal phase transitions in suspensions of polydisperse plate-like particles,” *Nature*, vol. 406, pp. 868–871, AUG 24 2000.

[5] N. Pinna, K. Weiss, J. Urban, and M. P. Pileni, “Triangular CdS nanocrystals: Structural and optical studies,” *Advanced Materials*, vol. 13, pp. 261+, FEB 19 2001.

[6] L. Manna, D. J. Milliron, A. Meisel, E. C. Scher, and A. P. Alivisatos, “Controlled growth of tetrapod-branched inorganic nanocrystals,” *Nature Materials*, vol. 2, pp. 382–385, JUN 2003.

[7] L. E. Euliss, J. A. DuPont, S. Gratton, and J. DeSimone, “Imparting size, shape, and composition control of materials for nanomedicine,” *Chemical Society Reviews*, vol. 35, no. 11, pp. 1095–1104, 2006.

[8] L. Roschier, R. Tarkiainen, M. Ahlskog, M. Paalanen, and P. Hakonen, “Manufacture of single electron transistors using AFM manipulation on multiwalled carbon nanotubes,” *Microelectronic Engineering*, vol. 61-2, pp. 687–691, JUL 2002. 27th International Conference on Micro- and Nano-Engineering, GRENOBLE, SPAIN, SEP 16-19, 2001.

[9] “Intel corporation, 60 years of the transistor: 1947 – 2007.”

[10] R. D. Kamien, “Topology from the bottom up,” *Science*, vol. 299, pp. 1671–1673, MAR 14 2003.

[11] G. M. Whitesides and B. Grzybowski, “Self-assembly at all scales,” *Science*, vol. 295, pp. 2418–2421, MAR 29 2002.

[12] W. A. Lopes and H. M. Jaeger, “Hierarchical self-assembly of metal nanostructures on diblock copolymer scaffolds,” *Nature*, vol. 414, pp. 735–738, DEC 13 2001.

[13] F. Gauffre and D. Roux, “Studying a new type of surfactant aggregate (”Spherulites”) as chemical microreactors. A first example: Copper ion entrapping and particle synthesis,” *Langmuir*, vol. 15, pp. 3738–3747, MAY 25 1999.

[14] M. P. Pileni, “Nanocrystal self-assemblies: Fabrication and collective properties,” *Journal of Physical Chemistry B*, vol. 105, pp. 3358–3371, MAY 3 2001.

[15] C. A. Mirkin, “Programming the assembly of two- and three-dimensional architectures with dna and nanoscale inorganic building blocks,” *Inorganic Chemistry*, vol. 39, no. 11, pp. 2258–2272, 2000.

[16] H. Zhang, S.-W. Chung, and C. A. Mirkin, “Fabrication of sub-50-nm solid-state nanostructures on the basis of dip-pen nanolithography,” *Nano Letters*, vol. 3, no. 1, pp. 43–45, 2003.

[17] Z.-L. Zhang, M. Horsch, M. H. Lamm, and S. C. Glotzer, “Tethered nano building blocks: Toward a conceptual framework for nanoparticle self-assembly,” *Nano Letters*, vol. 3, pp. 1341–1346, OCT 2003.

[18] S. C. Glotzer, M. A. Horsch, C. R. Iacovella, Z. L. Zhang, E. R. Chan, and X. Zhang, “Self-assembly of anisotropic tethered nanoparticle shape amphiphiles,” *Current Opinion in Colloid and Interface Science*, vol. 10, pp. 287–295, DEC 2005.

[19] C. Tanford, *The hydrophobic effect : formation of micelles and biological membranes*. Wiley New York, 1980.

[20] J. N. Israelachvili, *Intermolecular and surface forces*. Academic London, 1992.

[21] R. Larson, *The Structure and Rheology of Complex Fluids*. Oxford University Press, 1998.

[22] R. G. Larson, “Molecular Simulation of Ordered Amphiphilic Phases,” *Chemical Engineering Science*, vol. 49, pp. 2833–2850, SEP 1994.

[23] R. G. Larson, “Monte Carlo simulations of the phase behavior of surfactant solutions,” *Journal De Physique II*, vol. 6, pp. 1441–1463, OCT 1996.

[24] F. S. Bates and G. Fredrickson, “Block copolymer thermodynamics - theory and experiment,” *Annual Review of Physical Chemistry*, vol. 41, pp. 525–557, 1990.

[25] M. W. Matsen and F. S. Bates, “Unifying weak- and strong-segregation block copolymer theories,” *Macromolecules*, vol. 29, no. 4, pp. 1091–1098, 1996.

[26] F. J. Martinez-Veracoechea and F. A. Escobedo, “Monte carlo study of the stabilization of complex bicontinuous phases in diblock copolymer systems,” *Macromolecules*, vol. 40, pp. 7354–7365, OCT 2007.

[27] M. W. Matsen, “Gyroid versus double-diamond in abc triblock copolymer melts,” *Journal of Chemical Physics*, vol. 108, pp. 785–796, JAN 1998.

[28] T. Dotera and A. Hatano, “The diagonal bond method: A new lattice polymer model for simulation study of block copolymers,” *Journal of Chemical Physics*, vol. 105, pp. 8413–1427, NOV 1996.

[29] Y. Mogi, K. Mori, Y. Matsushita, and I. Noda, “Tricontinuous morphology of triblock copolymers of the abc type,” *Macromolecules*, vol. 25, pp. 5412–5415, SEP 1992.

[30] Y. Mogi, H. Kotsuji, Y. Kaneko, Y. Matsushita, and I. Noda, "Preparation and morphology of triblock copolymers of the abc type," *Macromolecules*, vol. 25, pp. 5408–5411, SEP 1992.

[31] T. Gemma, A. Hatano, and T. Dotera, "Monte carlo simulations of the morphology of abc star polymers using the diagonal bond method," *Macromolecules*, vol. 35, pp. 3225–3237, APR 2002.

[32] K. Hayashida, T. Dotera, A. Takano, and Y. Matsushita, "Polymeric quasicrystal: Mesoscopic quasicrystalline tiling in ABC star polymers," *Physical Review Letters*, vol. 98, MAY 11 2007.

[33] K. Hayashida, A. Takano, T. Dotera, and Y. Matsushita, "Giant zincblende structures formed by an ABC star-shaped terpolymer/homopolymer blend system," *Macromolecules*, vol. 41, pp. 6269–6271, SEP 9 2008.

[34] A. M. Jackson, J. W. Myerson, and F. Stellacci, "Spontaneous assembly of subnanometre-ordered domains in the ligand shell of monolayer-protected nanoparticles," *Nature Materials*, vol. 3, pp. 330–336, MAY 2004.

[35] M. C. Daniel and D. Astruc, "Gold nanoparticles: Assembly, supramolecular chemistry, quantum-size-related properties, and applications toward biology, catalysis, and nanotechnology," *Chemical Reviews*, vol. 104, pp. 293–346, JAN 2004.

[36] S. H. Im, Y. T. Lee, B. Wiley, and Y. N. Xia, "Large-scale synthesis of silver nanocubes: The role of HCl in promoting cube perfection and monodispersity," *Angewandte Chemie-International Edition*, vol. 44, no. 14, pp. 2154–2157, 2005.

[37] R. C. Jin, Y. W. Cao, C. A. Mirkin, K. L. Kelly, G. C. Schatz, and J. G. Zheng, "Photoinduced conversion of silver nanospheres to nanoprisms," *Science*, vol. 294, pp. 1901–1903, NOV 30 2001.

[38] T. Ohno and S. Yatsuya, "Growth of fullerene nanoparticles prepared by the gas-evaporation technique," *Journal of Materials Science*, vol. 33, pp. 5843–5847, DEC 15 1998.

[39] T. Sakai and P. Alexandridis, "Single-step synthesis and stabilization of metal nanoparticles in aqueous pluronic block copolymer solutions at ambient temperature," *Langmuir*, vol. 20, pp. 8426–8430, SEP 28 2004.

[40] Y. G. Sun and Y. N. Xia, "Shape-controlled synthesis of gold and silver nanoparticles," *Science*, vol. 298, pp. 2176–2179, DEC 13 2002.

[41] B. Wiley, Y. G. Sun, B. Mayers, and Y. N. Xia, "Shape-controlled synthesis of metal nanostructures: The case of silver," *Chemistry-A European Journal*, vol. 11, pp. 454–463, JAN 7 2005.

[42] B. Wiley, T. Herricks, Y. G. Sun, and Y. N. Xia, "Polyol synthesis of silver nanoparticles: Use of chloride and oxygen to promote the formation of single-crystal, truncated cubes and tetrahedrons," *Nano Letters*, vol. 4, pp. 1733–1739, SEP 2004.

[43] A. Margolin, R. Popovitz-Biro, A. Albu-Yaron, L. Rapoport, and R. Tenne, "Inorganic fullerene-like nanoparticles of TiS2," *Chemical Physics Letters*, vol. 411, pp. 162–166, AUG 5 2005.

[44] X. C. Gong, T. Milic, C. Xu, J. D. Batteas, and C. M. Drain, "Preparation and characterization of porphyrin nanoparticles," *Journal of the American Chemical Society*, vol. 124, pp. 14290–14291, DEC 4 2002.

[45] J. Pyun, K. Matyjaszewski, J. Wu, G. M. Kim, S. B. Chun, and P. T. Mather, "ABA triblock copolymers containing polyhedral oligomeric silsesquioxane pendant groups: synthesis and unique properties," *Polymer*, vol. 44, pp. 2739–2750, APR 2003.

[46] A. J. Waddon, L. Zheng, R. J. Farris, and E. B. Coughlin, "Nanostructured polyethylene-POSS copolymers: Control of crystallization and aggregation," *Nano Letters*, vol. 2, pp. 1149–1155, OCT 2002.

[47] N. A. Kotov, "Chemical engineering 696: Introduction to nanotechnology, course notes." 2005.

[48] G. Carotenuto and L. Nicolais, "Size-controlled synthesis of thiol-derivatized gold clusters," *Journal of Materials Chemistry*, vol. 13, no. 5, pp. 1038–1041, 2003.

[49] S. M. Gatica, M. W. Cole, and D. Velegol, "Designing van der Waals forces between nanocolloids," *Nano Letters*, vol. 5, pp. 169–173, JAN 2005.

[50] Z. Y. Tang, Z.-L. Zhang, Y. Wang, S. C. Glotzer, and N. A. Kotov, "Self-assembly of cdte nanocrystals into free-floating sheets," *Science*, vol. 314, pp. 274–278, OCT 2006.

[51] A. K. Boal, F. Ilhan, J. E. DeRouchey, T. Thurn-Albrecht, T. P. Russell, and V. M. Rotello, "Self-assembly of nanoparticles into structured spherical and network aggregates," *Nature*, vol. 404, pp. 746–748, 04 2000.

[52] J. J. Storhoff, R. Elghanian, C. A. Mirkin, and R. L. Letsinger, "Sequence-dependent stability of dna-modified gold nanoparticles," *Langmuir*, vol. 18, no. 17, pp. 6666–6670, 2002.

[53] Z. Li, R. Jin, C. A. Mirkin, and R. L. Letsinger, "Multiple thiol-anchor capped DNA-gold nanoparticle conjugates," *Nucleic Acids Research*, vol. 30, no. 7, pp. 1558–1562, 2002.

[54] I. Tokareva and E. Hutter, "Hybridization of oligonucleotide-modified silver and gold nanoparticles in aqueous dispersions and on gold films," *Journal of the American Chemical Society*, vol. 126, no. 48, pp. 15784–15789, 2004.

[55] H. D. Hill, R. J. Macfarlane, A. J. Senesi, B. Lee, S. Y. Park, and C. A. Mirkin, "Controlling the lattice parameters of gold nanoparticle fcc crystals with duplex dna linkers," *Nano Letters*, vol. 8, no. 8, pp. 2341–2344, 2008.

[56] T. Song, S. Dai, K. C. Tam, S. Y. Lee, and S. H. Goh, "Aggregation behavior of C-60-end-capped poly(ethylene oxide)s," *Langmuir*, vol. 19, pp. 4798–4803, MAY 27 2003.

[57] T. Song, S. Dai, K. C. Tam, S. Y. Lee, and S. H. Goh, "Aggregation behavior of two-arm fullerene-containing poly(ethylene oxide)," *Polymer*, vol. 44, pp. 2529–2536, APR 2003.

[58] S. Westenhoff and N. A. Kotov, "Quantum dot on a rope," *Journal of the American Chemical Society*, vol. 124, pp. 2448–2449, MAR 20 2002.

[59] S. Park, K. A. Brown, and K. Hamad-Schifferli, "Changes in oligonucleotide conformation on nanoparticle surfaces by modification with mercaptohexanol," *Nano Letters*, vol. 4, pp. 1925–1929, OCT 2004.

[60] S. J. Park, A. A. Lazarides, J. J. Storhoff, L. Pesce, and C. A. Mirkin, "The structural characterization of oligonucleotide-modified gold nanoparticle networks formed by DNA hybridization," *Journal of Physical Chemistry B*, vol. 108, pp. 12375–12380, AUG 19 2004.

[61] Y. Kim, J. Pyun, J. M. J. Frechet, C. J. Hawker, and C. W. Frank, "The dramatic effect of architecture on the self-assembly of block copolymers at interfaces," *Langmuir*, vol. 21, no. 23, pp. 10444–10458, 2005.

[62] K.-M. Sung, D. W. Mosley, B. R. Peelle, S. Zhang, and J. M. Jacobson, "Synthesis of monofunctionalized gold nanoparticles by fmoc solid-phase reactions," *Journal of the American Chemical Society*, vol. 126, no. 16, pp. 5064–5065, 2004.

[63] G. A. DeVries, M. Brunnbauer, Y. Hu, A. M. Jackson, B. Long, B. T. Neltner, O. Uzun, B. H. Wunsch, and F. Stellacci, "Divalent metal nanoparticles," *Science*, vol. 315, pp. 358–361, JAN 2007.

[64] Z. H. Nie, D. Fava, E. Kumacheva, S. Zou, G. C. Walker, and M. Rubinstein, "Self-assembly of metal-polymer analogues of amphiphilic triblock copolymers," *Nature Materials*, vol. 6, pp. 609–614, AUG 2007.

[65] W. Kai, L. Hua, T. Dong, P. Pan, B. Zhu, and Y. Inoue, "Polyhedral oligomeric silsesquioxane- and fullerene-end-capped Poly(epsilon-caprolactone)," *Macromolecular Chemistry and Physics*, vol. 209, pp. 1191–1197, JUN 19 2008.

[66] C. R. Iacovella, M. A. Horsch, Z. Zhang, and S. C. Glotzer, "Phase diagrams of self-assembled mono-tethered nanospheres from molecular simulation and comparison to surfactants," *Langmuir*, vol. 21, no. 21, pp. 9488–9494, 2005.

[67] C. R. Iacovella, A. S. Keys, M. A. Horsch, and S. C. Glotzer, "Icosahedral packing of polymer-tethered nanospheres and stabilization of the gyroid phase," *Physical Review E*, vol. 75, p. 040801, APR 2007.

[68] C. R. Iacovella, M. A. Horsch, and S. C. Glotzer, "Local ordering of polymer-tethered nanospheres and nanorods and the stabilization of the double gyroid phase," *Journal of Chemical Physics*, vol. 129, no. 044902, p. 044902, 2008.

[69] A. Jayaraman and K. S. Schweizer, "Structure and assembly of dense solutions and melts of single tethered nanoparticles," *Journal of Chemical Physics*, vol. 128, APR 28 2008.

[70] A. Jayaraman and K. S. Schweizer, "Effect of the number and placement of polymer tethers on the structure of concentrated solutions and melts of hybrid nanoparticles," *Langmuir*, vol. 24, pp. 11119–11130, OCT 7 2008.

[71] C. R. Iacovella and S. C. Glotzer, "Complex crystal structures formed by the self assembly of di-tethered nanospheres," *Nano Letters*, vol. In Press, 2009.

[72] M. A. Horsch, Z.-L. Zhang, C. R. Iacovella, and S. C. Glotzer, "Hydrodynamics and microphase ordering in block copolymers: Are hydrodynamics required for ordered phases with periodicity in more than one dimension?," *Journal of Chemical Physics*, vol. 121, pp. 11455–11462, DEC 2004.

[73] M. A. Horsch, Z. L. Zhang, and S. C. Glotzer, "Self-assembly of polymer-tethered nanorods," *Physical Review Letters*, vol. 95, no. 5, p. 056105, 2005. 056105.

[74] M. A. Horsch, Z. L. Zhang, and S. C. Glotzer, "Simulation studies of self-assembly of end-tethered nanorods in solution and role of rod aspect ratio and tether length," *Journal of Chemical Physics*, vol. 125, NOV 2006.

[75] X. Zhang, E. R. Chan, and S. C. Glotzer, "Self-assembled morphologies of monotethered polyhedral oligomeric silsesquioxane nanocubes from computer simulation," *Journal of Chemical Physics*, vol. 123, NOV 8 2005.

[76] E. R. Chan, X. Zhang, C. Y. Lee, M. Neurock, and S. C. Glotzer, "Simulations of tetra-tethered organic/inorganic nanocube-polymer assemblies," *Macromolecules*, vol. 38, p. 14, 2005.

[77] E. R. Chan, L. C. Ho, and S. C. Glotzer, "Computer simulations of block copolymer tethered nanoparticle self-assembly," *Journal of Chemical Physics*, vol. 125, AUG 14 2006.

[78] T. D. Nguyen, Z. Zhang, and S. C. Glotzer, "Molecular simulation study of self-assembly of tethered v-shaped nanoparticles," *Journal of Chemical Physics*, vol. 129, no. 24, p. 244903, 2008.

[79] T. Soddemann, B. Dunweg, and K. Kremer, "A generic computer model for amphiphilic systems," *European Physical Journal E*, vol. 6, pp. 409–419, DEC 2001.

[80] G. S. Grest and K. Kremer, "Molecular dynamics simulation for polymers in the presence of a heat bath," *Physical Review A*, vol. 33, pp. 3628–3631, 1986.

[81] F. K. vonGottberg, K. A. Smith, and T. A. Hatton, "Stochastic dynamics simulation of surfactant self-assembly," *Journal of Chemical Physics*, vol. 106, pp. 9850–9857, JUN 15 1997.

[82] F. K. von Gottberg, K. A. Smith, and T. A. Hatton, "Dynamics of self-assembled surfactant systems," *Journal of Chemical Physics*, vol. 108, pp. 2232–2244, FEB 1 1998.

[83] D. Frenkel and B. Smit, *Understanding Molecular Simulation*. Academic Press, Inc. Orlando, FL, USA, 2001.

[84] M. P. Allen and D. J. Tildesley, *Computer simulation of liquids*. Clarendon Press; Oxford University Press, 1989.

[85] A. J. Schultz, C. K. Hall, and J. Genzer, "Box length search algorithm for molecular simulation of systems containing periodic structures," *The Journal of Chemical Physics*, vol. 120, no. 4, pp. 2049–2055, 2004.

[86] C. R. Iacovella and S. C. Glotzer, "Phase behavior of di-tethered nanospheres," *In preparation*, 2009.

[87] P. J. Steinhardt, D. R. Nelson, and M. Ronchetti, "Bond-orientational order in liquids and glasses," *Physical Review B*, vol. 28, no. 2, pp. 784–805, 1983.

[88] J. C. Crocker and D. G. Grier, "Methods of digital video microscopy for colloidal studies," *Journal of Colloid and Interface Science*, vol. 179, pp. 298–310, APR 1996.

[89] P. Varadan and M. J. Solomon, "Direct visualization of long-range heterogeneous structure in dense colloidal gels," *Langmuir*, vol. 19, no. 3, pp. 509–512, 2003.

[90] A. S. Keys, C. R. Iacovella, and S. C. Glotzer, "Order parameters for assembly based on shape matching," *In preparation*, 2009.

[91] J. Yang, J. Y. Lee, T. C. Deivaraj, and H. P. Too, "A highly efficient phase transfer method for preparing alkylamine-stabilized Ru, Pt, and Au nanoparticles," *Journal of Colloid and Interface Science*, vol. 277, pp. 95–99, SEP 1 2004.

[92] D. van der Beek and H. N. W. Lekkerkerker, "Nematic ordering vs. gelation in suspensions of charged platelets," *Europhysics Letters*, vol. 61, pp. 702–707, MAR 2003.

[93] N. Malikova, I. Pastoriza-Santos, M. Schierhorn, N. A. Kotov, and L. M. Liz-Marzan, "Layer-by-layer assembled mixed spherical and planar gold nanoparticles: Control of interparticle interactions," *Langmuir*, vol. 18, pp. 3694–3697, APR 30 2002.

[94] S. C. Glotzer, M. J. Solomon, and N. A. Kotov, "Self-assembly: From nanoscale to microscale colloids," *AICHE Journal*, vol. 50, pp. 2978–2985, DEC 2004.

[95] S. C. Glotzer, “Some assembly required,” *Science*, vol. 306, pp. 419–420, OCT 15 2004.

[96] W. J. Parak, T. Pellegrino, C. M. Micheel, D. Gerion, S. Williams, and A. P. Alivisatos, “Conformation of oligonucleotides attached to gold nanocrystals probed by gel electrophoresis,” *Nano Letters*, vol. 3, pp. 33–36, JAN 2003.

[97] X. M. Lu, T. Hanrath, K. P. Johnston, and B. A. Korgel, “Growth of single crystal nanowires in supercritical silicon solution from tethered gold particles on a silicon substrate,” *Nano Letters*, vol. 3, pp. 93–99, JAN 2003.

[98] F. R. Siperstein and K. E. Gubbins, “Phase separation and liquid crystal self-assembly in surfactant-inorganic-solvent systems,” *Langmuir*, vol. 19, pp. 2049–2057, MAR 18 2003.

[99] M. Lisal, C. K. Hall, K. E. Gubbins, and A. Z. Panagiotopoulos, “Formation of Spherical Micelles in a supercritical Solvent: Lattice Monte Carlo simulation and multicomponent solution model,” *Molecular Simulation*, vol. 29, no. 2, pp. 139–157, 2003.

[100] G. K. Bourov and A. Bhattacharya, “The role of geometric constraints in amphiphilic self-assembly: A Brownian dynamics study,” *Journal of Chemical Physics*, vol. 119, pp. 9219–9225, NOV 1 2003.

[101] G. K. Bourov and A. Bhattacharya, “Brownian dynamics simulation study of self-assembly of amphiphiles with large hydrophilic heads,” *Journal of Chemical Physics*, vol. 122, JAN 22 2005.

[102] C. Loison, M. Mareschal, K. Kremer, and F. Schmid, “Thermal fluctuations in a lamellar phase of a binary amphiphile-solvent mixture: A molecular-dynamics study,” *Journal of Chemical Physics*, vol. 119, pp. 13138–13148, DEC 22 2003.

[103] C. Loison, M. Mareschal, and F. Schmid, “Pores in bilayer membranes of amphiphilic molecules: Coarse-grained molecular dynamics simulations compared with simple mesoscopic models,” *Journal of Chemical Physics*, vol. 121, pp. 1890–1900, JUL 22 2004.

[104] B. Fodi and R. Hentschke, “Simulated phase behavior of model surfactant solutions,” *Langmuir*, vol. 16, pp. 1626–1633, FEB 22 2000.

[105] S. Salaniwal, S. T. Cui, H. D. Cochran, and P. T. Cummings, “Molecular simulation of a dichain surfactant water carbon dioxide system. 1. Structural properties of aggregates,” *Langmuir*, vol. 17, pp. 1773–1783, MAR 6 2001.

[106] A. J. Schultz, C. K. Hall, and J. Genzer, “Computer simulation of copolymer phase behavior,” *Journal of Chemical Physics*, vol. 117, pp. 10329–10338, DEC 8 2002.

[107] M. Imai, A. Kawaguchi, A. Saeki, K. Nakaya, T. Kato, K. Ito, and Y. Amemiya, "Fluctuations of lamellar structure prior to a lamellar -¿ gyroid transition in a nonionic surfactant system," *Physical Review E*, vol. 62, no. 5, pp. 6865–6874, 2000.

[108] M. F. Schulz, A. K. Khandpur, F. S. Bates, K. Almdal, K. Mortensen, D. A. Hajduk, and S. M. Gruner, "Phase behavior of polystyrene-poly(2-vinylpyridine) diblock copolymers," *Macromolecules*, vol. 29, pp. 2857–2867, APR 8 1996.

[109] L. Leibler, "Theory of microphase separation in block co-polymers," *Macromolecules*, vol. 13, no. 6, pp. 1602–1617, 1980.

[110] P. Prinsen, P. B. Warren, and M. A. J. Michels, "Mesoscale simulations of surfactant dissolution and mesophase formation," *Physical Review Letters*, vol. 89, SEP 30 2002.

[111] K. Kataoka, A. Harada, and Y. Nagasaki, "Block copolymer micelles for drug delivery: design, characterization and biological significance," *Advanced Drug Delivery Reviews*, vol. 47, no. 1, pp. 113–131, 2001.

[112] M. Maldovan, A. M. Urbas, N. Yufa, W. C. Carter, and E. L. Thomas, "Photonic properties of bicontinuous cubic microphases," *Physical Review B*, vol. 65, no. 16, 2002. 165123.

[113] B. K. Cho, A. Jain, S. M. Gruner, and U. Wiesner, "Mesophase structure-mechanical and ionic transport correlations in extended amphiphilic dendrons," *Science*, vol. 305, no. 5690, pp. 1598–1601, 2004.

[114] Y. D. Yin and Y. N. Xia, "Self-assembly of spherical colloids into helical chains with well-controlled handedness," *Journal of the American Chemical Society*, vol. 125, no. 8, pp. 2048–2049, 2003.

[115] B. Yu, P. C. Sun, T. C. Chen, Q. H. Jin, D. T. Ding, B. H. Li, and A. C. Shi, "Confinement-induced novel morphologies of block copolymers," *Physical Review Letters*, vol. 96, no. 13, 2006. 138306.

[116] D. A. Hajduk, P. E. Harper, S. M. Gruner, C. C. Honeker, G. Kim, E. L. Thomas, and L. J. Fetters, "The gyroid - a new equilibrium morphology in weakly segregated diblock copolymers," *Macromolecules*, vol. 27, no. 15, pp. 4063–4075, 1994.

[117] I. W. Hamley, K. A. Koppi, J. H. Rosedale, F. S. Bates, K. Almdal, and K. Mortensen, "Hexagonal mesophases between lamellae and cylinders in a diblock copolymer melt," *Macromolecules*, vol. 26, no. 22, pp. 5959–5970, 1993.

[118] F. J. Martinez-Veracoechea and F. A. Escobedo, "Simulation of the gyroid phase in off-lattice models of pure diblock copolymer melts," *Journal of Chemical Physics*, vol. 125, no. 10, 2006. 104907.

[119] I. Rychkov, "Block copolymers under shear flow," *Macromolecular Theory and Simulations*, vol. 14, no. 4, pp. 207–242, 2005.

[120] M. W. Matsen and F. S. Bates, "Origins of complex self-assembly in block copolymers," *Macromolecules*, vol. 29, no. 23, pp. 7641–7644, 1996.

[121] H. Hasegawa, T. Hashimoto, and S. T. Hyde, "Microdomain structures with hyperbolic interfaces in block and graft copolymer systems," *Polymer*, vol. 37, no. 17, pp. 3825–3833, 1996.

[122] F. J. Martinez-Veracoechea and F. A. Escobedo, "Lattice monte carlo simulations of the gyroid phase in monodisperse and bidisperse block copolymer systems," *Macromolecules*, vol. 38, no. 20, pp. 8522–8531, 2005.

[123] J. P. K. Doye, D. J. Wales, and S. I. Simdyankin, "Global optimization and the energy landscapes of dzugutov clusters," *Faraday Discussions*, vol. 118, pp. 159–170, 2001.

[124] J. J. Chiu, B. J. Kim, E. J. Kramer, and D. J. Pine, "Control of nanoparticle location in block copolymers," *Journal of the American Chemical Society*, vol. 127, pp. 5036–5037, APR 2005.

[125] S. Westenhoff and N. A. Kotov, "Quantum dot on a rope," *Journal of the American Chemical Society*, vol. 124, no. 11, pp. 2448–2449, 2002.

[126] R. W. Date and D. W. Bruce, "Shape amphiphiles: Mixing rods and disks in liquid crystals," *Journal of the American Chemical Society*, vol. 125, no. 30, pp. 9012–9013, 2003.

[127] M. Lee, B. Cho, H. Kim, J. Yoon, and W. Zin, "Self-organization of rod-coil molecules with layered crystalline states into thermotropic liquid crystalline assemblies," *Journal of the American Chemical Society*, vol. 120, pp. 9168–9179, SEP 1998.

[128] R. D. Groot, T. J. Madden, and D. J. Tildesley, "On the role of hydrodynamic interactions in block copolymer microphase separation," *Journal of Chemical Physics*, vol. 110, pp. 9739–9749, MAY 1999.

[129] E. W. Cochran, C. J. Garcia-Cervera, and G. H. Fredrickson, "Stability of the gyroid phase in diblock copolymers at strong segregation," *Macromolecules*, vol. 39, pp. 2449–2451, APR 2006.

[130] M. Lee and W. Cho, B.K. Zin, "Supramolecular structures from rod-coil block copolymers," *Chemical Reviews*, vol. 101, pp. 3869–3892, DEC 2001.

[131] J. P. K. Doye and D. J. Wales, "The effect of the range of the potential on the structure and stability of simple liquids: from clusters to bulk, from sodium to," *Journal of Physics B: Atomic, Molecular and Optical Physics*, vol. 29, no. 21, pp. 4859–4894, 1996.

[132] M. Cosentino Lagomarsino, M. Dogterom, and M. Dijkstra, "Isotropic-nematic transition of long, thin, hard spherocylinders confined in a quasi-two-dimensional planar geometry," *Journal of Chemical Physics*, vol. 119, pp. 3535–3540, AUG 2003.

[133] C. R. Iacovella, A. S. Keys, and S. C. Glotzer, "Entropy stabilized quasicrystals.".

[134] D. Levine and P. J. Steinhardt, "Quasicrystals - a new class of ordered structures," *Physical Review Letters*, vol. 53, no. 26, pp. 2477–2480, 1984.

[135] A. I. Goldman and R. F. Kelton, "Quasi-crystals and crystalline approximants," *Review of Modern Physics*, vol. 65, pp. 213–230, JAN 1993.

[136] D. Shechtman, I. Blech, D. Gratias, and J. W. Cahn, "Metallic phase with long-range orientational order and no translational symmetry," *Physical Review Letters*, vol. 53, no. 20, pp. 1951–1953, 1984.

[137] S. J. Poon, A. J. Drehman, and K. R. Lawless, "Glassy to icosahedral phase transformation in pd-u-si alloys," *Physical Review Letters*, vol. 55, pp. 2324–2327, NOV 1985.

[138] N. Wang, H. Chen, and K. H. Kuo, "Two-dimensional quasicrystal with eightfold rotational symmetry," *Physical Review Letters*, vol. 59, pp. 1010–1013, Aug 1987.

[139] X. B. Zeng, G. Ungar, Y. S. Liu, V. Percec, S. E. Dulcey, and J. K. Hobbs, "Supramolecular dendritic liquid quasicrystals," *Nature*, vol. 428, pp. 157–160, MAR 11 2004.

[140] M. E. Zoorob, M. D. B. Charlton, G. J. Parker, J. J. Baumberg, and M. C. Netti, "Complete photonic bandgaps in 12-fold symmetric quasicrystals," *Nature*, vol. 404, pp. 740–743, APR 13 2000.

[141] Y. Wang, S. Jian, S. Han, S. Feng, Z. Feng, B. Cheng, and D. Zhang, "Photonic band-gap engineering of quasiperiodic photonic crystals," *Journal of Applied Physics*, vol. 97, no. 10, p. 106112, 2005.

[142] C. Jin, B. Cheng, B. Man, Z. Li, D. Zhang, S. Ban, and B. Sun, "Band gap and wave guiding effect in a quasiperiodic photonic crystal," *Applied Physics Letters*, vol. 75, no. 13, pp. 1848–1850, 1999.

[143] A. S. Keys and S. C. Glotzer, "How do quasicrystals grow?," *Physical Review Letters*, vol. 99, no. 23, p. 235503, 2007.

[144] S. J. Plimpton, "Fast parallel algorithms for short-range molecular dynamics,," *Journal of Computational Physics*, vol. 117, 195.

[145] M. Dzugutov, "Formation of a dodecagonal quasi-crystalline phase in a simple monatomic liquid," *Physical Review Letters*, vol. 70, pp. 2924–2927, MAY 1993.

[146] J. Roth and A. R. Denton, "Solid-phase structures of the dzugutov pair potential," *Physical Review E*, vol. 61, pp. 6845–6857, Jun 2000.

[147] G. Ungar, Y. Liu, X. Zeng, V. Percec, and W.-D. Cho, "Giant Supramolecular Liquid Crystal Lattice," *Science*, vol. 299, no. 5610, pp. 1208–1211, 2003.

[148] D. S. Sebba, J. J. Mock, D. R. Smith, T. H. LaBean, and A. A. Lazarides, "Reconfigurable core-satellite nanoassemblies as molecularly-driven plasmonic switches," *Nano Letters*, vol. 8, no. 7, pp. 1803–1808, 2008.

[149] X. P. Zhang, B. Q. Sun, R. H. Friend, H. C. Guo, D. Nau, and H. Giessen, "Metallic photonic crystals based on solution-processible gold nanoparticles," *Nano Letters*, vol. 6, pp. 651–655, APR 2006.

[150] E. V. Shevchenko, M. Ringler, A. Schwemer, D. V. Talapin, T. A. Klar, A. L. Rogach, J. Feldmann, and A. P. Alivisatos, "Self-assembled binary superlattices of CdSe and Au nanocrystals and their fluorescence properties," *Journal of the American Chemical Society*, vol. 130, pp. 3274+, MAR 19 2008.

[151] K. D. Hermanson, S. O. Lumsdon, J. P. Williams, E. W. Kaler, and O. D. Velev, "Dielectrophoretic assembly of electrically functional microwires from nanoparticle suspensions," *Science*, vol. 294, pp. 1082–1086, NOV 2 2001.

[152] M. M. C. Cheng, G. Cuda, Y. L. Bunimovich, M. Gaspari, J. R. Heath, H. D. Hill, C. A. Mirkin, A. J. Nijdam, R. Terracciano, T. Thundat, and M. Ferrari, "Nanotechnologies for biomolecular detection and medical diagnostics," *Current Opinion in Chemical Biology*, vol. 10, pp. 11–19, FEB 2006.

[153] E. V. Shevchenko, D. V. Talapin, N. A. Kotov, S. O'Brien, and C. B. Murray, "Structural diversity in binary nanoparticle superlattices," *Nature*, vol. 439, pp. 55–59, JAN 2006.

[154] M. E. Leunissen, C. G. Christova, A. P. Hynninen, C. P. Royall, A. I. Campbell, A. Imhof, M. Dijkstra, R. van Roij, and A. van Blaaderen, "Ionic colloidal crystals of oppositely charged particles," *Nature*, vol. 7056, pp. 235–240, SEP 2005.

[155] T. Vossmeyer, G. Reck, L. Katsikas, E. Haupt, B. Schulz, and H. Weller, "A double-diamond superlattice built-up of cd17s4(sch2ch2oh)(26) clusters," *Science*, vol. 267, no. 5203, pp. 1476–1479, 1995.

[156] Z. Y. Tang, N. A. Kotov, and M. Giersig, "Spontaneous organization of single cdte nanoparticles into luminescent nanowires," *Science*, vol. 297, pp. 237–240, JUL 2002.

[157] K. S. Cho, D. V. Talapin, W. Gaschler, and C. B. Murray, "Designing pbse nanowires and nanorings through oriented attachment of nanoparticles," *Journal of the American Chemical Society*, vol. 127, pp. 7140–7147, MAY 2005.

[158] Z.-L. Zhang, Z. Y. Tang, N. A. Kotov, and S. C. Glotzer, "Simulations and analysis of self-assembly of cdte nanoparticles into wires and shee," *Nano Letters*, vol. 7, pp. 1670–1675, JUN 2007.

[159] G. Zhang, D. Y. Wang, and H. Mohwald, "Decoration of microspheres with gold nanodots-giving colloidal spheres valences," *Angewandte Chemie-International Edition*, vol. 44, no. 47, pp. 7767–7770, 2005.

[160] L. Hong, A. Cacciuto, E. Luijten, and S. Granick, “Clusters of amphiphilic colloidal spheres,” *Langmuir*, vol. 24, pp. 621–625, FEB 2008.

[161] J. P. K. Doye, A. Louis, I. Lin, L. Allen, E. Noya, A. Wilber, H. Kok, and R. Lyus, “Controlling crystallization and its absence: proteins, colloids and patchy models,” *Physical Chemistry Chemical Physics*, vol. 9, no. 18, pp. 2197–2205, 2007.

[162] Z.-L. Zhang and S. C. Glotzer, “Self-assembly of patchy particles,” *Nano Letters*, vol. 4, pp. 1407–1413, AUG 2004.

[163] X. Zhang, Z.-L. Zhang, and S. C. Glotzer, “Simulation study of dipole-induced self-assembly of nanocubes,” *Journal of Physical Chemistry*, vol. 111, pp. 4132–4137, MAR 2007.

[164] Z.-L. Zhang, A. S. Keys, T. C. Chen, and S. C. Glotzer, “Self-assembly of patchy particles into diamond structures through molecular mimicry,” *Langmuir*, vol. 21, pp. 11547–11551, DEC 2005.

[165] G. A. DeVries, F. R. Talley, R. P. Carney, and F. Stellacci, “Thermodynamic Study of the Reactivity of the Two Topological Point Defects Present in Mixed Self-Assembled Monolayers on Gold Nanoparticles,” *Advanced Materials*, vol. 20, pp. 4243–4247, NOV 18 2008.

[166] F. Stellacci, “Personal communication.”.

[167] L. Liu, J.-K. Kim, R. Gunawidjaja, V. V. Tsukruk, and M. Lee, “Toroid Morphology by ABC-Type Amphiphilic Rod-Coil Molecules at the Air-Water Interface,” *Langmuir*, vol. 24, pp. 12340–12346, NOV 4 2008.

[168] H.-J. Kim, E. Lee, M. G. Kim, M.-C. Kim, M. Lee, and E. Sim, “Folding of coordination polymers into double-stranded helical organization,” *Chemistry-A European Journal*, vol. 14, no. 13, pp. 3883–3888, 2008.

[169] A. Schultz, *Modeling and Computer Simulation of Block Copolymer/Nanoparticle Nanocomposites*. PhD thesis, North Carolina State University, 2003.

[170] “Center for computational materials science of the united states naval research laboratory, crystal lattice structures web page,” 2009.

[171] M. De Graef and M. E. McHenry, *Structure of Materials*. Cambridge University Press, 2007.

[172] S. Phan and G. H. Fredrickson, “Morphology of symmetric abc triblock copolymers in the strong segregation limit,” *Macromolecules*, vol. 31, pp. 59–63, JAN 1998.

[173] V. L. Colvin, “Personal communication.” 2008.

[174] J. A. Anderson, C. D. Lorenz, and A. Travesset, “General purpose molecular dynamics simulations fully implemented on graphics processing units,” *Journal of Computational Physics*, vol. 227, pp. 5342–5359, MAY 1 2008.

[175] M. A. Horsch, *Mesoscale Modeling and Computer Simulation of Tethered Nanorod "Shape Amphiphile" Assemblies*. PhD thesis, The University of Michigan, 2006.